Numerical Modelling of Microbial Enhanced Oil Recovery with Focus on Dynamic Effects: An Iterative Approach

Master's Thesis in Applied and Computational Mathematics

Kai Skiftestad

Department of Mathematics
University of Bergen

29th May, 2015

Acknowledgements

My sincere gratitude and appreciation to my supervisor Dr.habil. Florin Adrian Radu for his help, hints, patient guidance and everlasting positivity regarding this project.

Also, thanks to the Department of Mathematics and the NUPUS cooperation, funded by the Research Council of Norway, for the opportunity to travel to the United States to visit universities and learn from the best. The trip was superbly organized and managed by professor Jan M. Nordbotten, and students from the University of Stuttgart and the Eindhoven University of Technology made lovely traveling companions.

Thanks to my fellow students and lecturers at UoB.

Kai Skiftestad,

May, 2015

Abstract

Recovering more of the available oil has been a main driver behind the extensive work done in the field of enhanced oil recovery (EOR) over the last decades. Microbial enhanced oil recovery (MEOR) has been heavily researched, and is picking up pace compared with other EOR methods used today. MEOR is economically attractive and has a huge potential if applied in accordance to reservoir conditions.

This thesis considers a two-phase flow regime in homogeneous porous media, under the influence of microbial activity. The mathematical model includes the concept of dynamic capillary pressure, and is based on Darcy's law, the principle of mass conservation and the diffusion/dispersion-advection equation. The inclusion of the dynamic capillary pressure makes this model classified as a so-called non-standard model. In this work we aim to explore this, as well as the effect microbes have on flow, and ultimately oil production.

Implementation of the mathematical model has been done in MATLAB by using a new, fully implicit, iterative approach, to cope with the fact that the dynamic capillarity induces an additional temporal derivative in the two-phase model. The spatial discretization has been carried out with the use of a control volume method, the TPFA, on a cell-centered grid in one dimension. The scheme is related to the papers [1–3].

The effects of dynamic capillary pressure are shown to be small at the macroscale for realistic oil reservoirs, while clearly visible in an extreme case which have been set up.

Regarding microbial activity we have constructed relations between concentration and interfacial tension based on the work in [4–8]. This is done to model the effect of reduced fluid-fluid tension on flow and further the oil production. It is shown that a substantial concentration of microbes have a positive effect on the production, while small concentrations do not differ significantly from the case of no concentration.

Contents

List of Figures

Abbreviations

EOR	**E**nhanced **O**il **R**ecovery
TEOR	**T**hermal **E**nhanced **O**il **R**ecovery
MEOR	**M**icrobial **E**nhanced **O**il **R**ecovery
IMPES	**IM**plicit **P**ressure **E**xplicit **S**aturation
REV	**R**epresentative **E**lementary **V**olume
IFT	**I**nter**f**acial **T**ension
TPFA	**T**wo **P**oint **F**lux **A**pproximation
BC(s)	**B**oundary **C**ondition(**s**)
IC(s)	**I**nitial **C**ondition(**s**)
FVM	**F**inite **V**olume **M**ethod
OOIP	**O**riginal **O**il **I**n **P**lace
OIP	**O**il **I**n **P**lace

Symbols

ϕ	porosity	-
p	average pressure	MPa
p_α	phase α pressure	MPa
s_α	phase α saturation	-
s	water saturation	-
s^*	effective water saturation	-
t	time	s
x	position	m
ρ_α	phase α density	kg/m^3
k	permeability	mD [milliDarcy]
$k_{r,\alpha}$	relative permeability phase α	-
p_c	static capillary pressure	MPa
p_e	static capillary entry pressure	MPa
σ	surface tension between phases	N/m or J/m^2
g	gravitational acceleration	m/s^2
$\vec{u_\alpha}$	Darcy flux phase α	m^3/s
$\vec{u_\Sigma}$	total Darcy flux	m^3/s
μ_α	viscosity of phase α	$Pa \cdot s$
λ_α	phase α mobility	$1/(Pa \cdot s)$
λ_Σ	total mobility	$1/(Pa \cdot s)$
Δx	spatial step	m
Δt	time step	s
F_α	source term phase α	kg/day
D	dispersion-diffusion coefficient	m^2/day
bbl	barrel	-
α	microbial effect coefficient	-
τ	dynamic coefficient	$Pa \cdot s$

Chapter 1

General Introduction

The world's energy consumption has risen tremendously throughout the last 70 years, mainly driven by an increase in fossil fuel use, such as oil. Recovering as much of the available oil as possible is the reason why enhanced oil recovery has been a focus area in both academia and industry over the last decades, and is the motivation for the topic of this work. Microbial enhanced oil recovery is a tertiary oil recovery technique, seen as economically attractive and environmentally friendly, aiming to increase lifetime of mature reservoirs.

In this thesis we seek to model flow in porous media, more specifically the flow of oil and water within an oil reservoir. The flow in such an underground petroleum reservoir is a very complex phenomena, and can only be solved analytically when making extensive simplifications, thus resulting in erroneous descriptions of the physical model and therefore invalid solutions for many fluid flow problems. This has led to the extensive use of mathematical models, numerical methods and simulation software in the petroleum industry, providing better correlation between the physical model, the mathematical model and the numerical model.

We seek to explore the effect of adding microbes to an oil reservoir to enhance the recovery, the so-called MEOR - microbial enhanced oil recovery. This is done by modelling a one dimensional reservoir consisting of two phases, the oil- and water-phase, where flow is governed by the Darcy law and mass conservation for each phase. The flow is described by a standard two-phase model, where the phases are assumed incompressible and immiscible. The fate of the microbes is modelled by the advective-dispersive/diffusive

transport equation. In addition, the flow model considers dynamic capillary effects, which will be explored in detail through several numerical examples.

This work is interesting and innovative due to

- The standard IMPES method has been improved to account for dynamic capillarity, by an iterative, fully implicit, approach on the two-phase flow model.
- We have proposed new parameterizations for the link between microbial effects and interfacial tension.
- The model explores the coupled effect of MEOR and dynamic capillary pressure.

The outline of the thesis is set up as following:

Chapter 2 gives the reader an overview of the concepts and properties of porous media, and the most important flow-governing equations. Further, it includes an introduction to the MEOR method, in addition to a brief introduction to other enhanced oil recovery methods.

Chapter 3 derives the mathematical model of interest, with a starting point at Darcy's law, the concept of mass conservation and the advection-diffusion/dispersion equation. Additionally, theory on the concept of capillary pressure and dynamic capillarity is introduced. At the end, the full mathematical model of our interest is summarized and presented.

Chapter 4 is devoted to numerical methods, and gives an overview of the discretization of the model and the gridding of our domain. In addition to the TPFA, it also describes how we handle boundary conditions and which methods of approximation are used for integrals, derivatives and physical parameters, such as the matrix- and relative permeabilities.

Chapter 5 includes new parameterizations, based on [4–8], describing the dependence on microbial activity for interfacial tension, capillary pressure, relative permeabilities and residual oil saturation. Further we explore the effect of MEOR and dynamic capillary pressure, and include sensitivity analysis of key parameters. Convergence of the new scheme is investigated numerically.

Chapter 6 discusses our findings, offers a conclusion and outlines suggestions for further work.

Chapter 2

Flow in Porous Media and Microbial Enhanced Oil Recovery

This chapter is devoted to giving the reader a brief overview of the physical concepts that forms our mathematical understanding and modelling of the flow in porous media, along with a theoretical background for Microbial Enhanced Oil Recovery (MEOR). Examples of porous materials are to be found everywhere around us, such as biological tissue as skin, bones and wood, and the tarmac on roads and runways. However, in the following, we will use a typical oil reservoir-setup, with sedimentary rocks as the porous medium.

2.1 Flow in Porous Media

A porous medium is a material consisting of pores or void space, as well as a solid part, often referred to as the skeleton or the matrix of the medium. Porous media that are of our interest contains interconnected pores, which allows fluid to move continuously. In the study of oil reservoirs it is of great importance to be able to mathematically model the flow through the porous medium. This is necessary in order to give predictions about production, mobility, pressure, temperature and more, inside the reservoir. For us to be able to model the medium, it is required to understand that it is not possible to model the reservoir at a micro-scale. Thus we introduce a commonly used spatial averaging procedure, the Representative Elementary Volum (REV) approach [10].

The REV-method gives us the possibility to provide a certain bounded volume of space, which is used for averaging the physical properties of the medium. The value at a single mathematical point of the parameter, like e.g. porosity or permeability, is defined as the value of this parameter in a REV of porous medium surrounding this point. The size of the REV is, in short, defined by being sufficiently large to contain a representative number of pores, while at the same time being small enough to preserve local properties [10]. The optimal size also depends heavily on the type of medium, and depends on the level of heterogeneity [11].

2.1.1 Physical properties

A natural property used to describe the porous medium is its *porosity*, ϕ. The porosity is intuitively defined as the volume of void space over the total volume of the REV, and is therefore a dimensionless property between 0 and 1. For carbonate reservoirs the porosity usually lies in the range between 0.05 and 0.20, depending on the depth [12].

Another common property of the medium is the *absolute permeability*, $\mathbf{k}$. The permeability is a property describing the fluids ability to flow within the medium, the flow conductivity. Permeability has the dimension of area [L^2], and can be modelled as both a tensor accounting for heterogeneousness and anisotropic behavior, or at the other extreme as a constant. As the dimension of $\mathbf{k}$ is area, the SI-unit is m^2. This thesis make use of the more common and practical unit *Darcy* ($\approx 0.986\,922\,\mu m^2$), where we present absolute permeability in milliDarcys, mD, throughout.

The two main properties used to describe the physics of the fluid are the *viscosity*, μ, and the *density*, ρ. Viscosity can informally be understood as the "thickness" of the fluid, and is of great importance to how easily the fluid flows - the higher the viscosity - the more resistant it is to flow. The dimension of μ is [$ML^{-1}T^{-1}$]. At room temperature water has a viscosity of approximately 1 mPa $\cdot$ s, while honey possesses a $\mu \approx 10\,000$ mPa $\cdot$ s.

Density is defined as the fluids mass per volume, $\rho = \frac{\text{Mass of fluid}}{\text{Volume of fluid}}$, with dimension [$ML^{-3}$], hence the unit being kg/m^3. In general, all fluids are *compressible*, due to the density depending on e.g. pressure and temperature. However, it is customary to treat fluids as *incompressible*, due to relatively small changes, letting ρ be a constant.

2.1.2 The flow-governing equations

The two main equations describing the flow of different phases in porous media are Darcy's law and the mass conservation equation [13, 14]. The first is named after the French civil engineer Henry Darcy who performed multiple experiments which lead to a formulation of a relationship between hydraulic head and flux. This has later been extended and formalized into Darcy's law in its simplest formulation as

$$\vec{u} = -\boldsymbol{\kappa}\nabla h, \tag{2.1}$$

where h is the hydraulic head and $\boldsymbol{\kappa}$ is the hydraulic conductivity. Darcy's law can be formulated in different fashions, depending on which area of application it is used within, and which variables that are relevant. For this report we make use of the relationship between the hydraulic head and the pressure, p, as $h = \frac{p}{\rho g} + z$. In addition, we express the hydraulic conductivity, $\boldsymbol{\kappa}$, in terms of permeability, density, gravitational acceleration and viscosity, to formulate

$$\vec{u} = -\frac{\mathbf{k}}{\mu}\nabla(p - \rho\vec{g}). \tag{2.2}$$

Gravitational acceleration is a physical constant, while in the equation above, Equation (2.2), g is included through the gravitational acceleration vector $\vec{g} = -g \cdot \vec{e_z}$, where we have chosen positive direction against the gravitational forces. Pressure, p, is a physical property that quantize the amount of force applied perpendicular to an object or surface, per area. The most commonly used unit for pressure is pascal, Pa, which simply equals 1 $\mathrm{N/m^2}$. Thus, the dimension of pressure is $[\mathrm{ML^{-1}T^{-2}}]$.

In Equations (2.1) and (2.2) $\vec{u}$ is the volumetric flux of fluid, or the volume of fluid per total area per time, resulting in dimension $[\mathrm{LT^{-1}}]$ [14].

The Darcian approach is limited to Newtonian fluids in laminar flows, where the viscous forces rule and the fluids are moving slowly along parallel streamlines.

Mass conservation/balance

Mass conservation is an intuitive physical principle that states that the total mass remains unchanged. The mathematical equation describing this principle can be derived on a closed domain Ω, see Figure 2.1.

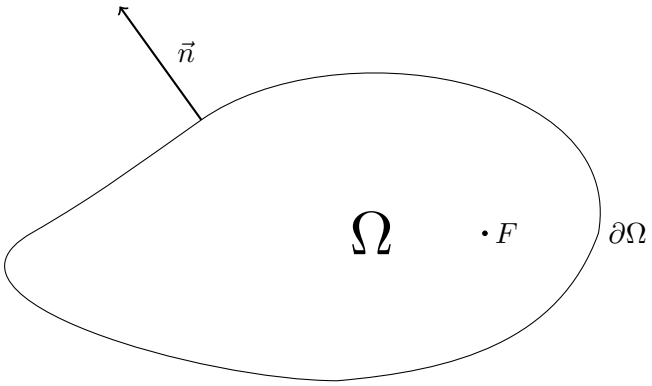

FIGURE 2.1: A domain Ω with boundary $\partial\Omega$, possible source/sink F and outward pointing unit normal $\vec{n}$.

Assume that at time $t_0 = 0$ there is a mass m_o inside the domain. Later, at a time $t > t_0$, there will be a total mass $m = m_0 + m_{in/out} + m_F$, inside the domain. Here, the mass passing through the boundary and the mass entering or leaving through any possible sinks/sources, is accounted for. If there are no sources/sinks, such an equation will be referred to as a conservation law, while if sources/sinks are present, it is a balance equation [14]. One can formalize this as

$$\frac{\partial m}{\partial t} = -\vec{f} \cdot \vec{n} + F, \tag{2.3}$$

where $\vec{f} \cdot \vec{n}$ is the flux of mass through the boundary, while F is the contribution from the sinks/sources. Integrating this over the whole domain included the boundary, and applying the divergence theorem yields

$$\int_\Omega \frac{\partial m}{\partial t} \mathrm{d}V = -\int_{\partial\Omega} \vec{f} \cdot \vec{n} \mathrm{d}S + \int_\Omega F \mathrm{d}V \int_\Omega \frac{\partial m}{\partial t} \mathrm{d}V = -\int_\Omega \nabla \cdot \vec{f} \mathrm{d}V + \int_\Omega F \mathrm{d}V, \tag{2.4}$$

which holds for arbitrary domains Ω. This, combined with the fact that the integrand is continuous, results in the differential formulation of mass balance as

$$\frac{\partial m}{\partial t} + \nabla \cdot \vec{f} = F. \tag{2.5}$$

This will be exemplified through the derivation of the two-phase flow model in the next chapter.

2.1.3 Transport equation

For later use in the thesis it is also of interest to introduce a transport equation based on the mass conservation equation. Say one has a component C, let $c = c(x,t)$ be the concentration of component C. Then the balance equation

$$\frac{\partial c}{\partial t} + \nabla \cdot (-\vec{u}c + \vec{j}) = Q(\mathbf{x}, t) \tag{2.6}$$

should be satisfied for all domains Ω.

The term $-\vec{u}c + \vec{j}$ represents the total flux through the boundary $\partial\Omega$ and is combined of advective flux, $(-\vec{u}c)$, and diffusive-dispersive flux, $(\vec{j})$. Advection is the process whereas the component is transported with the flow, while diffusion and dispersion is the spreading of molecules from areas of high concentration to areas of lower concentration. The term defining the diffusion-dispersion process originates from Fick's law of diffusion. The Q on the right hand side is now also including internal reactions, either chemical or biological, as well as external sources or sinks [14].

The equation will be further investigated in the next chapter, where we will rewrite the transport equation in order to model species only living in the water phase.

2.2 EOR - Enhanced Oil Recovery

Oil recovery in general consists of three phases. In the first phase, the *primary* phase, one utilizes the natural pressure within the reservoir to push crude oil to the surface. The *secondary* recovery phase makes use of water, and/or gas, to re-pressurize the reservoir, with intent to drive more of the oil towards the production wells. After this phase there is still a substantial amount of residual oil, a tertiary potential of more than 50 %, left in the reservoir. This is where EOR methods are brought into play.

Enhanced oil recovery is a general term for all different types of effort being made to realize the tertiary potential. Maintaining reservoir pressure is still of key importance, while at the same time trying to change some of the properties governing the flow of oil. This can be done in several ways, and we will only give a very short overview of some of the techniques that are explored and used today.

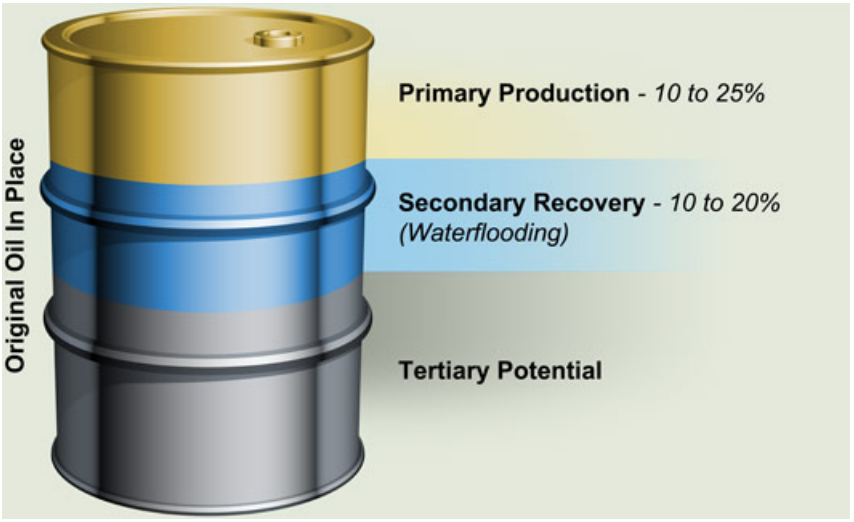

FIGURE 2.2: After the initial and secondary phase there is still a huge potential for oil recovery (courtesy of Mid-Con Energy Partners).

Chemical flooding is a collective term for the techniques where one adds different types of chemicals to the injection water. Depending on the type of process, this can lead to a changed interfacial tension (IFT) between water and oil (typically surfactants and alkalis), and/or make the water viscosity match the oil viscosity (polymers) [15]. Chemical flooding has been a known EOR technique since the '60s [16], and can potentially be a very effective technique. It is crucial to account for the chemical properties of the rock and the thermal conditions in the reservoir, when developing the solvent [15]. Chemical flooding is today mostly employed in China, and contributes to approximately one third of a million barrels of oil per day [17].

Thermal methods, often abbreviated as TEOR, introduces heat energy to the reservoir, and includes injection of steam, hot water and combustion [17]. It is by far the most widely used EOR method, contributing approximately 2 million oil barrels per day [17]. Recent big scale applied thermal methods also includes solar EOR, where solar power is used to produce steam.

Gas injection used as an EOR technique involves the injection of natural gas, carbon dioxide or nitrogen, and is in general an effective way to enhance the recovery. The main idea is to use a miscible gas that reduces the IFT between water and oil, hence improving the displacement of oil. The availability and cost of gas locally are the main limitations of to which extent the technique is being used today.

2.3 MEOR - Microbial Enhanced Oil Recovery

In this thesis we will focus on microbial enhanced oil recovery, which is a method where one introduces microbes into the reservoir in order to alter fluid and/or matrix properties. Microbes, or microorganisms, are single-celled creatures such as bacteria, fungi, viruses and more, so small (≈ 0.5 - 5 µm) that they are only visible with the help of a microscope.

2.3.1 Implementation

Generally, three strategies exist for implementing MEOR [18–20]:

Injection of nutrients to stimulate indigenous microbes is only desirable if there already exist microbes in the reservoir that can alter properties in a sought-after fashion. Identification of both the microbes, the metabolites or activity they result in or perform, and determination of the correct nutrient is necessary before one starts stimulating the microbes [18, 21].

Injection of exogenous microbes and nutrients consists of injecting *both* the microbes themselves *and* the nutrient they feed on. The microbes must be capable of living and breeding within given reservoir conditions. If so, this technique might be favorable in two ways. Firstly, one has the opportunity to choose the type of microbe(s), based on what kind of activity one wants to obtain. Secondly, this makes sure that the activity happens quickly [18]. A critical factor of this approach is the transport ability of such microbes in the reservoir [18].

Injection of ex situ produced products. If indigenous microorganisms are not suitable for the desired outcome and conditions in the reservoir are too harsh for survival of exogenous microbes, the last possibility is to add ex situ-produced products [18, 20]. Metabolites such as biopolymers and surfactants are coming from bacteria grown ex situ on suitable nutrients, before they are introduced into the reservoir.

The first two approaches have the added difficulties of having to compete for nutrition with other indigenous microorganisms, maintaining nutrition levels throughout the reservoir and dealing with bacteria transport [21]. Thus, it is believed that the third strategy is the simplest and most likely to succeed in field-scale operations [22], but it also comes with the capital cost of bioreactor operations and product purification [20].

2.3.2 Mechanisms

Metabolic products of microbes include biosurfactants, acids, solvents, gases, biopolymers and enzymes, which all have different effect on the interplay between phases and the porous medium, see Table 2.1. The ultimate goal is to enhance the recovery of crude oil, and this can be achieved in several ways, and by several mechanisms [18–20, 23]:

Reduction of oil-water IFT, where the bond, or tension, that keeps oil and water together is reduced or broken down, is the most promising mechanism of MEOR. This leads to the oil having a higher probability of being mobilized.

Selective clogging/plugging is a mechanism where one add microbes with the ability to breed, thus resulting in biomass that plug pores, reducing the number of paths for the fluid to flow through. If one succeeds in clogging for instance the preferred "highway" of flow, the fluids need to find new paths through the medium, with the consequence that immobilized oil may be mobilized. Other potential mechanisms are

- **Degradation of the rocks** by production of acid,
- **Reduction of oil viscosity** which is closely linked with the reduction of IFT,
- **Formation of gas** that results in local pressurization.

TABLE 2.1: Metabolites of MEOR and their effects [23, 24]

Metabolite	Effects
Acid	- Improves permeability and porosity by degradation of the rock - Reduction of oil viscosity by production of CO_2 when reacting with carbonates
Solvents	- Dissolving the oil
Biomass	- Selective/non-selective plugging - Altering wettability - Reduction of oil viscosity
Gases	- Pressurization of the reservoir - Viscosity reduction
Surfactants	- Reducing IFT - Emulsification
Polymers	- Mobility control - Selective/non-selective plugging

2.3.3 Pros and cons of MEOR

MEOR was described by Beckman already in 1926 [24], but is still not widely applied as an EOR method today. This is, and has been, due to problems or challenges regarding the method. One of the main challenges, and reason for the failure of many MEOR projects, is the harsh reservoir conditions. The activity of reservoir-employed microbes depends on both chemical and physical conditions, such as e.g. temperature, salinity, pressure, pH and redox potential. Such conditions vary a lot between different reservoirs [25], and the planning of the MEOR process does not emphasize these conditions sufficiently, the project is likely to fail. However, all factors should be possible to overcome, according to Adetunji [25]. Another aspect is, that to expect significant effects of MEOR, there is a need for high concentrations of metabolites in small areas of the reservoir. Lazar [26] also lists three other problems regarding MEOR:

- Lost injectivity due to wellbore plugging,
- Insufficient transport/dispersion of necessary components to the target zone,
- The existence of competition or undesirable secondary activity.

On the plus side, there are also several important and interesting points that make MEOR an attractive method to research [26]:

- Microbes and nutrients are obtainable and inexpensive,
- MEOR processes are cheap and therefore attractive for marginally producing fields as an alternative before abandonment,
- Microbial cell factories need little energy to produce agents,
- Less modification of field structure compared with other EOR methods,
- The cost of microbes are not dependent on the oil price since they are not petrochemicals,
- The effects of MEOR improves with population and therefore time, as compared to other EOR methods,
- MEOR is environmentally compatible,
- All over economically attractive.

Chapter 3

A Simplified Mathematical Model for MEOR with Dynamic Capillary Pressure

To be able to mathematically investigate the effects of added microorganisms to an oil reservoir, we need to set up a solvable, yet describable and reliable, model. In this thesis we will assemble a one-dimensional model of a two-phase flow, and couple it with an equation describing the dynamics of microbial transport. The mathematical model we derive is fully based on continuum theory, in this case the REV method described in Chapter 2.

3.1 Two-Phase Flow

Firstly, we need to be able to describe the motion of flow within a porous medium that consists of two phases, e.g. oil/water or gas/water. To do this, we set up the governing equations for each phase, namely Darcy's law, see Equation (2.2), and the mass conservation, Equation (2.5). Also, we have to define a new variable, the *saturation*, s_α, where $\alpha = n, w$ distinguishes between the non-wetting and the wetting phase. Saturation quantize how much of the void space is filled with each of the phases, and is defined intuitively as the volume of a phase over the total volume of voids in the REV, as $s_\alpha = \frac{\text{volume of phase } \alpha}{\text{volume of voids in REV}}$. Saturation is therefore a dimensionless quantity between 0

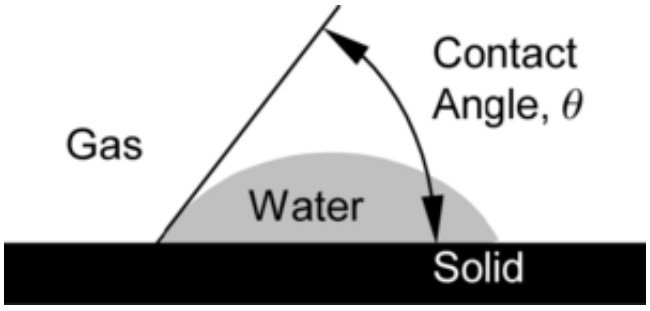

FIGURE 3.1: A droplet of water in gas on a solid. Water is here the wetting phase, gas is non-wetting. Illustration borrowed from [27].

and 1. Note that the sum of saturations always equals 1,

$$\sum_{\alpha=w,n} s_\alpha = 1. \tag{3.1}$$

The *wetting phase* is at all times defined as the phase most preferentially attracted to the solid, with contact angle $\theta < 90°$, see Figure 3.1.

In this thesis we are exploring *immiscible* fluids, fluids that do not mix with each other, which is a commonly assumed property of a two-phase flow consisting of oil and water.

Relative permeability

When two phases compete for the space in the porous medium, they affect each others available void space, i.e., they will block some of the pathways and space for each other. To model this we will introduce a constitutive relation relating permeability and water saturation, together with the effects of microbial activity, see Sections 4.4.1 and 5.2.1. This leads to the total effective permeability for each fluid being expressed as a product of the relative permeability for phase α times the absolute permeability of the medium,

$$\mathbf{k}_{\text{eff},w} = k_{r,w}(s_w, c)\mathbf{k} \qquad \text{and} \qquad \mathbf{k}_{\text{eff},n} = k_{r,n}(s_w, c)\mathbf{k}. \tag{3.2}$$

Effective saturation

The parameterizations in this work will include the water saturation as an *effective* saturation. This is done by mapping real values of water saturation to values ranging

from 0 to 1. Mathematically, this can be expressed as

$$s^* = \frac{s_w - s_{res}}{s_{max} - s_{res}}, \tag{3.3}$$

where s_{res} is the residual water saturation, while s_{max} is the maximum water saturation in the pore space. This is a special case of the so-called *normalized water content*

$$\Theta = \frac{\theta - \theta_{res}}{\theta_{max} - \theta_{res}}, \tag{3.4}$$

with $\theta = \phi s_w$ being the current water content. Also, θ_{res} is the residual water content, and θ_{max} is the maximum water content in the pore space. This normalization was used by Mualem in 1976 [28], and also by van Genuchten [29].

The residual water saturation denotes the water trapped and immobilized inside the pore space, while the maximum water saturation corresponds to $1 - s_{n,res}$, the inverse of the residual oil/gas saturation.

In the remainder of this thesis we denote water saturation by s for simplicity.

3.1.1 The concept of capillary pressure and interfacial tension

While single phase flow is governed only by gravitational and pressure gradients, two-phase immiscible flow involves a third gradient is in the model. This stems from the fact that across the curved fluid-fluid interfaces there is a difference in pressure, where the pressure on the concave side exceeds the one on the convex side. These sharp interfaces and pressure differences on a microscopic level gives rice to capillary forces. Such forces partly governs the flow on a macroscopic level [30]. This concept is used to link the phase pressures together by the capillary pressure relation, as

$$p_c = p_n - p_w. \tag{3.5}$$

The capillary pressure itself is most commonly parameterized as an algebraic function of water saturation [14], as we will see later, in Section 4.4.1, and may also be influenced by microbes on the interface, see Section 5.2.1. The phenomenon can also be related directly to the surface tension, or interfacial tension (IFT), between the fluids, by the

Young-Laplace equation

$$p_c = \frac{2\sigma cos(\theta)}{r_{\text{eff}}}, \tag{3.6}$$

on the microscale. Above, σ is the surface- or interfacial tension between phases, θ is the contact angle between interface and solid and r_{eff} is the effective curvature radius of the pore. One easily notices that if the interface is close to flat (i.e., curvature radius is big), there is a very little pressure difference/capillary pressure, and vice versa. Between phases such as oil and water, which will be thoroughly explored in the following, the IFT is typically of magnitude $20 - 30$ mN/m.

As a consequence of the relationship between IFT and capillary pressure, we will include effects due to a potential IFT-reduction in our work at a later stage, see Section 5.2.1.

3.1.2 Dynamic capillarity

This part contains basic theory and practical consequences of dynamic capillary effects that may occur in flow with two or more phases. Hassanizadeh et al. [31] states that simulations and experimental studies indicates that such effects may be important for some field situations with unsaturated flow. Thus, numerical simulators should generally include tools for handling them. This will be implemented in our model to ensure that we have the possibility to include these effects in our simulations of the two-phase flow.

The typical relationship from Section 4.4.1 is derived from experiments where one measures the capillary pressure at equilibrium conditions. For small changes in p_c the saturation is measured only when equilibrium is reached, which can take several days. Hence, this may be seen as the static capillary pressure. In fact, there is ample, both theoretical and experimental, evidence that this static relationship is not unique, capillary pressure is shown to depend both on hysteresis, due to trapping of phases, and on the rate of change of saturation [31, 32]. This is natural when we are discussing non-equilibrium situations (i.e., there is flow). The fluid-fluid interfaces tend to change position to equilibrate internal and external forces which governs flow dynamics when the stable situation is breached, i.e., $\partial_t s \neq 0$ [33]. Mathematically, the relationship

$$p_c = p_n - p_w \tag{3.7}$$

only holds at equilibrium conditions, while at all other conditions dynamic effects *may* be present. We include this as a linear approximation of the dependence on the rate of saturation change as

$$p_n - p_w = p_c(s, c) - \tau \frac{\partial s}{\partial t}, \tag{3.8}$$

which is shown to capture the effects seen in experiments [31]. Here, τ is defined as the dynamic capillary coefficient, which is taken either to be a constant, or as a function depending on saturation, and is of dimension $[\mathrm{ML}^{-1}\mathrm{T}^{-1}]$, the unit being $\mathrm{Pa} \cdot \mathrm{s}$.

In the following, $p_n - p_w$ is described as the difference in phase pressures, p_c is the empirical measured capillary pressure under equilibrium conditions, and $p_c - \tau\, \partial_t s$ is the dynamic capillary pressure.

3.1.3 Deriving the two-phase flow model

With mass as a product of porosity, saturation and density, and the flux as a product of density and Darcy flux, we can set up a system for the two-phase flow based on the governing equations described in Chapter 2:

$$\begin{aligned} \vec{u_w} &= -\frac{k_{r,w}(s_w)\mathbf{k}}{\mu_n}(\nabla p_w - \rho_w \vec{g}), \\ \vec{u_n} &= -\frac{k_{r,n}(s_w)\mathbf{k}}{\mu_n}(\nabla p_n - \rho_n \vec{g}), \\ \phi \frac{\partial s_w}{\partial t} + \nabla \cdot \vec{u_w} &= \frac{F_w}{\rho_w}, \\ \phi \frac{\partial s_n}{\partial t} + \nabla \cdot \vec{u_n} &= \frac{F_n}{\rho_n}. \end{aligned} \tag{3.9}$$

Here, $kr_n(s_w)$ and $kr_w(s_w)$ are the relative permeability functions as introduced in Equation (3.2), and F_w and F_n are sink/source terms for the wetting and non-wetting phase. Note that some simplifications have been applied in the above. Both the solid part and the fluids are said to be *incompressible*, resulting in ϕ, ρ_n and ρ_w being constants. Also, the fluids are assumed to be immiscible and non-diffusive.

The latter part of the system, the two conservation equations, can be summed up, resulting in

$$\phi \frac{\partial (s_w + s_n)}{\partial t} + \nabla \cdot (\vec{u_w} + \vec{u_n}) = \frac{F_w}{\rho_w} + \frac{F_n}{\rho_n}. \tag{3.10}$$

By using the sum of saturations from Equation (3.1), notice that the temporal derivative vanishes and

$$\nabla \cdot (\vec{u_w} + \vec{u_n}) = \sum_{\alpha=w,n} \frac{F_\alpha}{\rho_\alpha}. \tag{3.11}$$

One possibility to simplify the above further is to introduce and define two new variables. First we introduce the average pressure, which we in the following denote p, as an arithmetic average of the two phase pressures,

$$p = \frac{p_w + p_n}{2}. \tag{3.12}$$

The average pressure will end up being one of our primary variables in the model. The phase pressures can now be written

$$p_w = p - \frac{1}{2}p_c + \frac{\tau}{2}\frac{\partial s}{\partial t} \qquad \text{and} \qquad p_n = p + \frac{1}{2}p_c - \frac{\tau}{2}\frac{\partial s}{\partial t}, \tag{3.13}$$

using the capillary pressure relation Equation (3.8).

Secondly we introduce phase mobility. Phase mobility is defined as the ratio of relative permeability of a phase to its viscosity, as $\lambda_\alpha = \frac{k_{r,\alpha}}{\mu_\alpha}$ for $\alpha = w, n$, and has dimension $[\mathrm{LTM}^{-1}]$. For the two phases we have

$$\lambda_w = \frac{k_{r,w}}{\mu_w} \qquad \text{and} \qquad \lambda_n = \frac{k_{r,n}}{\mu_n}. \tag{3.14}$$

Based on this we also define the sum of mobilities (i.e., the total mobility), and the difference in mobilities as

$$\lambda_\Sigma = \lambda_n + \lambda_w \qquad \text{and} \qquad \lambda_\Delta = \lambda_n - \lambda_w. \tag{3.15}$$

Now, by combining Equations (3.12), (3.13) and (3.15) we can write the Darcy fluxes as

$$\begin{aligned} \vec{u_w} &= -\lambda_w \mathbf{k}(\nabla(p - \frac{1}{2}p_c + \frac{\tau}{2}\frac{\partial s}{\partial t})), \\ \vec{u_n} &= -\lambda_n \mathbf{k}(\nabla(p + \frac{1}{2}p_c - \frac{\tau}{2}\frac{\partial s}{\partial t})), \end{aligned} \tag{3.16}$$

and combine them as the total flux

$$\vec{u_\Sigma} = \vec{u_w} + \vec{u_n} = -\mathbf{k}(\lambda_\Sigma \nabla p + \frac{1}{2}\lambda_\Delta(\nabla(p_c - \tau\frac{\partial s}{\partial t})). \tag{3.17}$$

Notice that we have omitted the gravitational gradient, as this thesis only considers a one-dimensional model in a horizontal domain.
Combining Equation (3.17) and Equation (3.11) results in a pseudo-elliptic PDE that we from now on define as our **pressure equation**

$$\nabla \cdot (-\mathbf{k}(\lambda_\Sigma \nabla p + \frac{1}{2}\lambda_\Delta \nabla(p_c - \tau\frac{\partial s}{\partial t})) = \sum_{\alpha=w,n} \frac{F_\alpha}{\rho_\alpha}. \tag{3.18}$$

As stated previously it is highly common to parameterize the constitutive relations explicitly based on the water saturation, which will also be used throughout this thesis. Later, we will extend the parameterizations to include microbial effects, through the concentration, c. Both the static capillary pressure and the relative permeabilities are functions of s as

$$k_{r,w} = k_{r,w}(s), \qquad k_{r,n} = k_{r,n}(s), \qquad p_c = p_c(s). \tag{3.19}$$

As a consequence of the above, it is natural to couple the pressure equation with the mass conservation equation for the water phase,

$$\phi\frac{\partial s_w}{\partial t} + \nabla \cdot \vec{u_w} = \frac{F_w}{\rho_w}. \tag{3.20}$$

By substituting the water flux from Equation (3.16) we obtain the nonlinear pseudo-parabolic equation from now on defined as the **saturation equation**

$$\phi\frac{\partial s}{\partial t} - \nabla \cdot (\mathbf{k}\lambda_w(\nabla(p - \frac{1}{2}p_c + \frac{\tau}{2}\frac{\partial s}{\partial t})) = \frac{F_w}{\rho_w}. \tag{3.21}$$

A comprehensive study of the existence and uniqueness, as well as error estimates for the Euler method applied on such equations, is performed by Fan and Pop in [34].

3.1.4 The complete two-phase flow model

This leaves us with one mass conservation equation, the saturation equation, and one summed flux equation, the pressure equation. To close the model we have to include constitutive relations, and to ensure the uniqueness and well-posedness of it we must apply initial- and boundary conditions. Our complete two-phase flow model is then comprised of

$$\nabla \cdot (-\mathbf{k}(\lambda_\Sigma \nabla p - \frac{1}{2}\lambda_\Delta \nabla (p_c - \tau \frac{\partial s}{\partial t}))) = \frac{F_w}{\rho_w}, \quad \text{in} \quad \Omega,$$

$$\phi \frac{\partial s}{\partial t} - \nabla \cdot (\mathbf{k}\lambda_w (\nabla (p - \frac{1}{2}p_c + \frac{\tau}{2}\frac{\partial s}{\partial t}))) = \frac{F_w}{\rho_w}, \quad \text{in} \quad \Omega,$$

$$\text{Initial conditions:} \quad s = s(\mathbf{x}, t_0) \quad \text{and} \quad p = p(\mathbf{x}, t_0) \quad \text{in} \quad \Omega,$$

$$\text{Appropriate boundary conditions for } s \text{ and } p \quad \text{on} \quad \partial\Omega,$$

$$\text{Parameterizations:} \quad k_{r,w} = k_{r,w}(s), \qquad k_{r,n} = k_{r,n}(s), \qquad p_c = p_c(s), \qquad \tau = \tau(s).$$

3.2 Modelling the Transport

One of the main challenges of the MEOR method is to transport the microbes far enough into the reservoir for them to have a significant effect on the oil recovery. To model the transport of microbes in the reservoir we introduce a transport equation which describes the spatial and temporal distribution of microbes, the advection-dispersion/diffusion equation from Chapter 2. The transport equation for the water phase is

$$\frac{\partial \theta c}{\partial t} = \nabla \cdot (D \nabla \theta c - \vec{q} c) + Q(\mathbf{x}, t), \tag{3.22}$$

where $\theta = \phi s$ is the water content, c is the concentration of microbes, D is the diffusion-dispersion coefficient, $\vec{q}$ is the velocity of the transporting fluid and Q is a source/sink/reaction term for the microbes.

Dispersion and advection

The term $\nabla \cdot (D \nabla C)$ is the *diffusion-dispersion* term, and accounts for the diffusive and dispersive effects. It is composed of both molecular diffusion and mechanical dispersion, but these types cannot be distinguished on the Darcy scale which we operate on.

$\nabla \cdot (\vec{u}C)$ is the *advection* term, accounting for the transport of microbes with the flow of velocity $\vec{q}$. If one of the terms strongly dominates the other (e.g., if advection strongly dominates diffusion-dispersion), it is possible to omit the dominated term and express the transport equation either as a purely advective equation (i.e., as a first order hyperbolic PDE), or as a purely diffusive-dispersive equation, a second order parabolic PDE. In this thesis we will consider both effects on the microbial transport.

Growth, decay and absorption of microbes

During transport there will be a fraction of microbes that is absorbed by the surface. This can by taken into account by an additional term on the left hand side, describing the evolution of attached microbes. This thesis will not take into accounts such phenomenon and therefore the theory is omitted.

Growth and decay is another natural matter to consider when modelling living organisms. These effects are usually included through the source/sink term Q. A simple inclusion can for instance be the Langmuir isotherm

$$r = \frac{\mu_{max} N}{K + N}, \tag{3.23}$$

where μ_{max} is the maximum growth rate, K is the half saturation coefficient and N is the nutrient concentration. See for instance [35, 36] for an extended practical and theoretical overview. We also refer to the PhD thesis of Radu [37] for other possible isotherms.

Our transport model

In this thesis we limit our exploration to microbes that live in water. This allows us to derive a transport equation where microbes only appears in the water phase, as

$$\phi \frac{\partial (sc)}{\partial t} + \nabla \cdot (-\nabla(\phi D s c) + \vec{u}_w c) = Q(\mathbf{x}, t), \tag{3.24}$$

where c is the concentration of microbes, s is the water saturation and $\vec{u}_w$ is the water flux.

3.3 Our Complete System of Equations

In the remainder of this thesis we will numerically explore the two-phase model coupled with the transport model. We will also investigate the effects microbes have on the constitutive relations, so that the relative permeabilities and the capillary pressure are also depending on the concentration, c. This will be done in one spatial dimension (1D), so that our starting point is

$$\frac{\partial}{\partial x}(-k(\lambda_\Sigma \frac{\partial p}{\partial x} + \frac{1}{2}\lambda_\Delta \frac{\partial}{\partial x}(p_c - \tau \frac{\partial s}{\partial t}))) = \sum_{\alpha=w,n} \frac{F_\alpha}{\rho_\alpha}, \quad \text{in} \quad \Omega,$$

$$\phi \frac{\partial s}{\partial t} - \frac{\partial}{\partial x}(\mathbf{k}\lambda_w(\frac{\partial}{\partial x}(p - \frac{1}{2}p_c + \frac{\tau}{2}\frac{\partial s}{\partial t}))) = \frac{F_w}{\rho_w}, \quad \text{in} \quad \Omega,$$

$$\phi \frac{\partial sc}{\partial t} + \frac{\partial}{\partial x}(-\frac{\partial}{\partial x}(\phi D sc) + u_w c) = Q(x,t), \quad \text{in} \quad \Omega,$$

Initial conditions: $s = s(x,t_0), \quad p = p(x,t_0), \quad c = c(x,t_0),$ in Ω,

Appropriate boundary conditions for s, p and c on $\partial\Omega$,

Parameterizations: $k_{r,w} = k_{r,w}(s,c), \quad k_{r,n} = k_{r,n}(s,c), \quad p_c = p_c(s,c), \quad \tau = \tau(s).$

Chapter 4

Numerical Modelling

Numerical modeling is in this thesis our main tool for solving the mathematical model. It is widely used in most areas of technology and engineering, and is therefore defined and understood in several ways. In any case, it is always the process of solving a simplified physical or technical problem with the use of different numerical techniques. In our case we use it to approximate the solutions of our coupled system of nonlinear differential equations. Our approach to doing this is based on the so-called IMPES approach, where one make use of both explicit and implicit techniques.

Its basic idea is to combine the flow equations to obtain a single pressure equation, as described in Chapter 3, which is solved implicitly. After pressure has been advanced in time one updates the saturation explicitly based on the pressure at the new time level. The standard IMPES-method was first proposed by Sheldon et al. in 1959 [38], and has been the subject of much interest in both the academic spheres and the industry.

In order to include dynamic capillarity in our model, we develop a new, iterative, fully implicit scheme, based on the ideas in [1–3].

Our spatial discretization is made with the use of a certain control volume method, the Two Point Flux Approximation (TPFA), with the support of finite differences, in one dimension. In the following, we will give the theoretical background for the discretization techniques, and show the discretization of our coupled system in short.

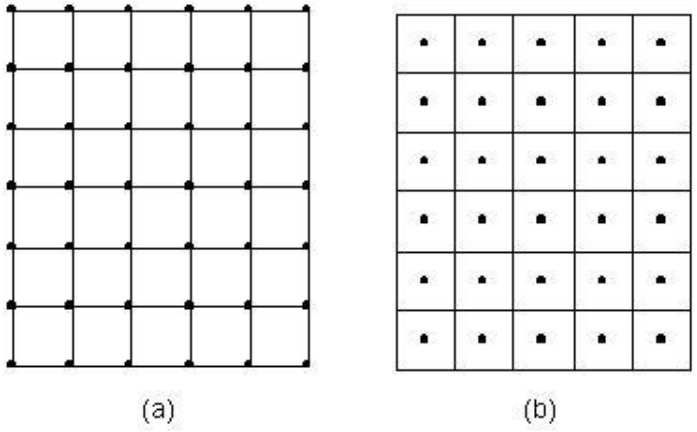

FIGURE 4.1: A 2D-grid with (a) mesh-centered and (b) cell-centered gridpoints.

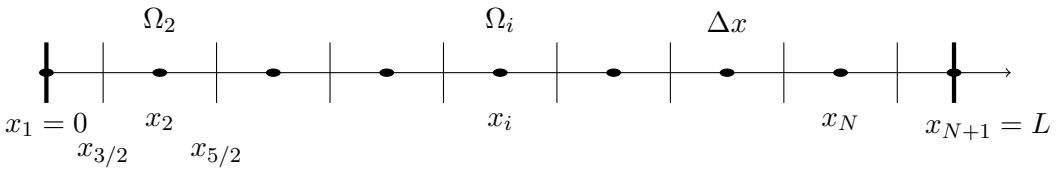

FIGURE 4.2: A uniform cell-centered grid in 1D with half-cells at the boundaries.

4.1 Discretization and the TPFA

We are almost always interested in the solution to differential equations inside a finite domain in space. Therefore, whenever we need to solve a mathematical problem numerically, defining and discretizing the domain of interest is a natural first step.

4.1.1 Gridding

Our geometric discretization turns a continuous domain into a discrete representation of it. This is done by placing discrete mathematical points at certain locations in the domain, and define a cell around it to be a 1D-shape (interval), 2D-shape (e.g. a triangle) or 3D-shape (e.g. a tetrahedron). One can either let the points be the node of the cells, a so-called mesh-centered, or vertex-centered, grid, or let the cell surround the discrete mathematical point, a cell-centered grid, see comparison in Figure 4.1.

Thomas [39] describes the differences and similarities between the two and states that which approach is used often depends on the area of application. In the following we will

mainly discuss the cell-centered grid. Our TPFA-approach utilize a point-distributed, cell-centered grid with equidistant points in 1D, with half-cells near the boundary of the domain, see Figure 4.2. The half-cells is one out of the two most common ways to handle the boundary of the domain when using a cell-centered grid [13, 39]. The other possibility is to add a ghost cell, with a ghost point, outside the domain, which causes difficulties incorporating Dirichlet boundary conditions.

Given our setup of the point-distributed, cell-centered, grid this is not a problem, as we are able to proceed straight forward with such conditions.

Our time-discretization is based on Euler's method. We divide our time-interval [0,T], which spans from the initial time $t_0 = 0$ to a final time T, into n equally sized time steps. We label the size of the time step Δt, which is the total time divided by number of steps, $\Delta t = \frac{T}{n}$.

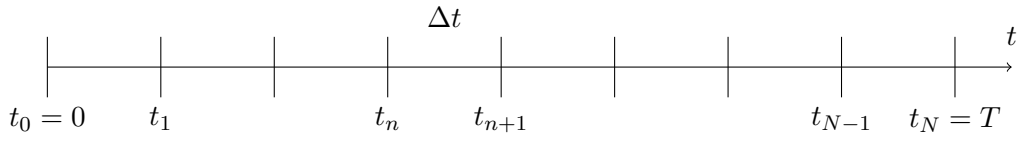

FIGURE 4.3: A uniform discretization in time from $t = 0$ to T.

Combining the space- and time discretization give us the discrete time-space grid shown in Figure 4.4 for our domain, $T \times \Omega$.

A function $f(t, x)$ defined on this domain is represented discretely in matrix form as

$$\mathbf{f} = \begin{pmatrix} f(t_0, x_1) & f(t_0, x_2) & \dots & \dots & \dots & f(t_0, x_{N+1}) \\ f(t_1, x_1) & f(t_1, x_2) & \dots & \dots & \dots & f(t_1, x_{N+1}) \\ \vdots & \vdots & \ddots & \ddots & \ddots & \vdots \\ \vdots & \vdots & \ddots & \ddots & \ddots & \vdots \\ f(t_N, x_1) & f(t_N, x_2) & \dots & \dots & \dots & f(t_N, x_{N+1}) \end{pmatrix}.$$

4.1.2 Methods of approximation

The main approximations used throughout the thesis, for calculating discrete derivatives, mobilities and derivatives, are presented in this section.

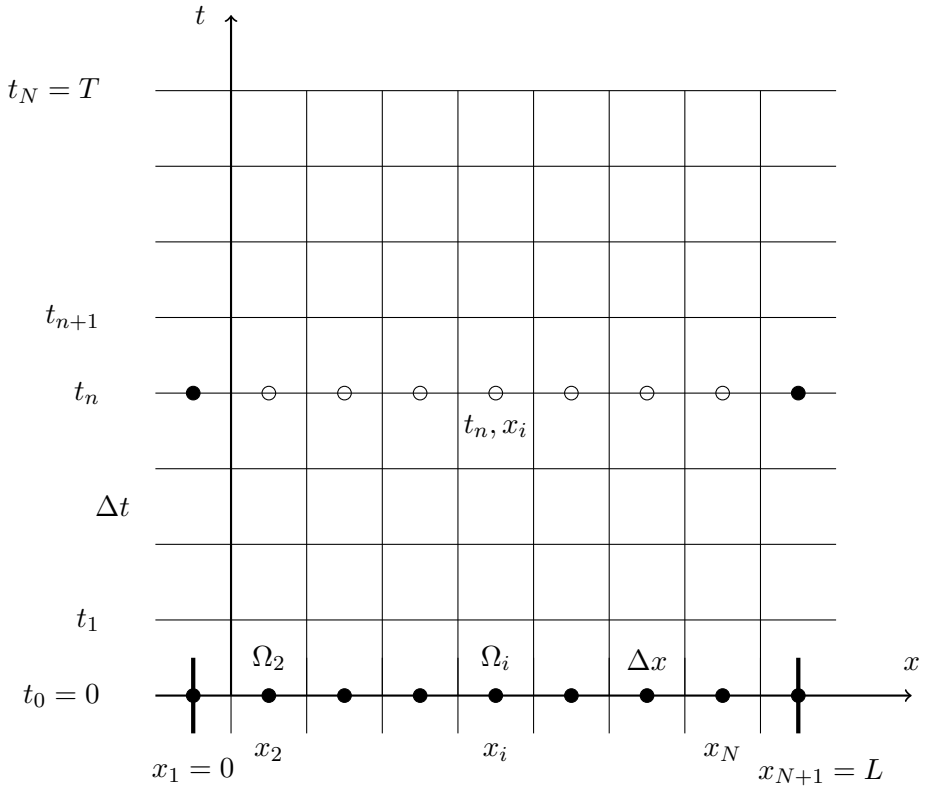

FIGURE 4.4: Our time-space grid on $[0, T]x[0, L]$ where ● corresponds to known values due to ICs or BCs, while ○ corresponds to unknown values.

The midpoint rule

Numerical quadrature is used for the computation of integrals in numerical modelling. A common way of approximating a definite integral is to apply the midpoint rule. For a general integral, one divides the interval $[a, b]$ into n equal subintervals with equal length, $h = (b - a)/n$, and compute a weighted sum of functional values at the midpoints of these subintervals, as

$$\int_a^b f(x)\,\mathrm{d}x \approx h \sum_{i=1}^{n} f(m_i), \qquad \forall \quad i = a + h(i - 1/2), \quad 1 \leq i \leq n. \tag{4.1}$$

The midpoint rule is used throughout this thesis, due to the fact that we operate on a cell-centered grid. That is, we approximate the integral of a function over the control interval Ω_i, using the midpoint of the interval multiplied by its length

$$\int_{x-1/2}^{x+1/2} f(x)\,\mathrm{d}x \approx f(x_i)\Delta x, \tag{4.2}$$

given equidistant gridpoints. The method is relatively simple, yet provides strong results, and the error is bounded by the second derivative and the length of the subinterval

$$|\text{error}| \leq \frac{L}{24}\Delta x^3, \tag{4.3}$$

when $|f''(x)| \leq L \quad \forall \quad x$.

Taylor series

The derivative of a function $f(x)$ is defined

$$f'(x) = \lim_{h \to 0} \frac{f(x+h) - f(x)}{h}, \tag{4.4}$$

at the points x, where the limit exist [40]. This makes it natural for us to use Taylor series for approximating the derivatives in our model. A Taylor series is a representation of a function f as an infinite sum of terms around a point h, using the derivative of the function, f'. In our case we make use of the two series

$$\begin{aligned} f(x+h) &= f(x) + hf'(x) + \frac{h^2}{2!}f''(x) + \frac{h^3}{3!}f'''(x) + \frac{h^4}{4!}f^{(4)}(x)\ldots, \\ f(x-h) &= f(x) - hf'(x) + \frac{h^2}{2!}f''(x) - \frac{h^3}{3!}f'''(x) + \frac{h^4}{4!}f^{(4)}(x)\ldots, \end{aligned} \tag{4.5}$$

which are combined to approximate the first derivative using the forward difference or the centered difference as

$$\begin{aligned} f'(x) &\approx \frac{f(x+h) - f(x)}{h} = f'(x) + \frac{h}{2}f''(x) + \frac{h^2}{6}f^{(3)}(x) + O(h^3), \\ f'(x) &\approx \frac{f(x+\frac{h}{2}) - f(x-\frac{h}{2})}{h} = f'(x) + \frac{h^2}{24}f^{(3)}(x) + O(h^4). \end{aligned} \tag{4.6}$$

Note that using forward differences yields a truncation error of $O(h)$, while using centered differences is of $O(h^2)$. In general throughout this thesis, the latter is used for the spatial derivatives, while the first is used for the temporal derivatives, due to the gridding described in Section 4.1.1.

Upstream weighted permeabilities

The permeability of the medium, k, at the boundaries $i + \frac{1}{2}$ is approximated by harmonically averaging over two adjacent intervals as

$$k_{i+1/2} = \frac{1}{\frac{1}{2}\left(\frac{\Delta x_i}{k_i} + \frac{\Delta x_{i+1}}{k_{i+1}}\right)}, \qquad \forall \quad i. \tag{4.7}$$

Using the fact that we are operating on equidistant grid throughout this thesis, this can be simplified in the following way;

$$k_{i+1/2} = \frac{1}{\frac{\Delta x}{2}\left(\frac{1}{k_i} + \frac{1}{k_{i+1}}\right)}, \qquad \forall \quad i. \tag{4.8}$$

Hence, the permeability prescribed at each grid point in the input data is never used in the simulations, as they are converted to half-point inter-cell values during the initialization, overwriting original permeability values [41].

To compute relative permeability it is natural, from the standpoint of numerical analysis, to compute this as an arithmetic average over two adjacent cells

$$k_{r,i+1/2} = \frac{1}{2}\left(k_r(s_i) + k_r(s_{i+1})\right). \tag{4.9}$$

This is a midpoint weighted average over two intervals, and is of second order. However, it leads to instability and erroneous results for many flow problems [13]. Because of this, the commonly used scheme [13, 38] is the upstream weighting, which is defined as

$$k_{r,i+1/2} = \begin{cases} k_r(s_i), & \text{if flow is from } i \text{ to } i+1, \\ k_r(s_{i+1}), & \text{if flow is from } i+1 \text{ to } i, \end{cases} \tag{4.10}$$

for both the relative permeability functions. The above is implemented by determining the direction of flow, and based on this, choosing the upstream cell for the calculations of relative permeabilities, which is a physical property that moves with the flow [41].

This weighting will, as a natural cause of the above-mentioned, be used throughout this work.

4.1.3 Two point flux approximation (TPFA)

TPFA is a certain control volume method, which, as finite volume methods (FVMs) in general, is more physically motivated than finite difference methods. The basic idea of all FVMs is to integrate the equations over finite volumes which stems from the partition of a domain Ω into a number of volumes as $\Omega = \{\Omega_1, ..., \Omega_i, ..., \Omega_N\}$. The equations should be, at least partly, on divergence form. For our use of the TPFA in 1D, this divergence is the *flux* over the boundaries of the control interval Ω_i. This may be demonstrated by using the stationary pressure equation Equation (3.18), expressed for total Darcy flux, as

$$\nabla \cdot \vec{u_\Sigma} = \sum_{\alpha=w,n} \frac{F_\alpha}{\rho_\alpha}. \tag{4.11}$$

Integrating this over Ω_i

$$\int_{\Omega_i} \nabla \cdot \vec{u_\Sigma} \, \mathrm{d}x = \int_{\Omega_i} \sum_{\alpha=w,n} \frac{F_\alpha}{\rho_\alpha} \, \mathrm{d}x, \tag{4.12}$$

and applying the divergence theorem from calculus, yields

$$\int_{\partial\Omega_i} \vec{u_\Sigma} \cdot \vec{n} \, \mathrm{d}x = \int_{\Omega_i} \sum_{\alpha=w,n} \frac{F_\alpha}{\rho_\alpha} \, \mathrm{d}x. \tag{4.13}$$

By letting *i-1/2* denote the left boundary with outward pointing normal $\vec{n}_{i-1/2}$, and *i+1/2* denote the right boundary with outward pointing normal $\vec{n}_{i+1/2}$, this can be formulated

$$\int_{\partial\Omega_{i-1/2}} \vec{u_\Sigma} \cdot \vec{n}_{i-1/2} \, \mathrm{d}x + \int_{\partial\Omega_{i+1/2}} \vec{u_\Sigma} \cdot \vec{n}_{i+1/2} \, \mathrm{d}x = \int_{\Omega_i} \sum_{\alpha=w,n} \frac{F_\alpha}{\rho_\alpha} \, \mathrm{d}x. \tag{4.14}$$

Due to the fact that $\vec{n}_{i-1/2} = [-1, 0]$, and $\vec{n}_{i+1/2} = [1, 0]$, given positive direction to the right as normal, this yields

$$-\int_{\partial\Omega_{i-1/2}} \vec{u_\Sigma} \, \mathrm{d}x + \int_{\partial\Omega_{i+1/2}} \vec{u_\Sigma} \, \mathrm{d}x = \int_{\Omega_i} \sum_{\alpha=w,n} \frac{F_\alpha}{\rho_\alpha} \, \mathrm{d}x, \tag{4.15}$$

approximated as

$$-\frac{\vec{u}_{\Sigma,i} - \vec{u}_{\Sigma,i-1}}{\Delta x} + \frac{\vec{u}_{\Sigma,i+1} - \vec{u}_{\Sigma,i}}{\Delta x} = \sum_{\alpha=w,n} \frac{F_{\alpha,i}}{\rho_\alpha} \Delta x. \tag{4.16}$$

We have here assumed that the flux u_Σ is continuous over each of the boundaries, and therefore across the control volume Ω_i.

When the flux-governing derivatives for pressures are approximated using centered differences, and the source integral on the right hand side is approximated using the midpoint rule, this results in a complete discretization of the pressure equation as shown in Section 4.2.1.

4.1.4 Boundary- and initial conditions

To close a system of differential equations in general one needs to incorporate a set of boundary- and initial conditions. This is necessary to ensure that the system has a unique solution. For a one dimensional domain, the boundaries are located at the endpoints of the interval, and the conditions accounts for the interaction with the surroundings outside the domain. Boundary conditions are the most likely source of error in mathematical modelling, and must therefore be taken care of accordingly [42].

Several types of boundary conditions (BCs), and combinations of them, exist and are used in numerical modelling. In this thesis however, we will limit both theory and application to the natural and essential types of boundary conditions, the Neumann and Dirichlet BCs, which accounts for the majority of application in our field of study.

Dirichlet boundary conditions

Dirichlet BCs are often referred to as first-type or essential boundary conditions, and are prescribed values of the unknown at the boundaries of the domain. Exemplifying this by again using the stationary pressure equation, Equation (3.18), the values of the unknown pressure can be Dirichlet BCs as

$$p(t, x = 0) = p_0(t), \tag{4.17}$$

$$p(t, x = L) = p_L(t), \tag{4.18}$$

where L is the length of the interval. Due to the way we have constructed the grid, these conditions are easily incorporated, making up the first and last equation in the system

later derived in Equation (4.41) as

$$\begin{pmatrix} 1 & 0 & \dots & \dots & 0 \\ \vdots & \ddots & \ddots & \ddots & \vdots \\ \vdots & \ddots & \ddots & \ddots & \vdots \\ 0 & \dots & \dots & 0 & 1 \end{pmatrix} [p_1, \dots, p_{N+1}]^{n+1} = \begin{pmatrix} p_0 \\ \vdots \\ \vdots \\ p_L \end{pmatrix}. \tag{4.19}$$

The Dirichlet BCs must be incorporated in the matrix system for implicit techniques as they affect other equations than the first and last, noticeable from Equations (4.19) and (4.41). In this thesis we will do so for both the pressure equation as above, and for the saturation- and transport equation in the same manner.

For explicit techniques on the other hand, the equations governing the Dirichlet BCs are not affecting the neighboring cells at the same time level, and the boundary value prescribed in the conditions can be applied directly to the unknown without considering other effects.

Neumann boundary conditions

The second type of boundary conditions are the Neumann BCs, often referred to as the natural boundary conditions in the weak sense. For the pressure equation they can be used to express the flow rate across the boundary, and/or specify the production rate, the known influx from aquifer, or flow from parts of the reservoir outside the domain [13]. As above, we exemplify by using Equation (3.18), so that the Neumann BCs are

$$\frac{\partial p}{\partial x}(t, x = 0) = q_0(t), \tag{4.20}$$

$$\frac{\partial p}{\partial x}(t, x = L) = q_L(t). \tag{4.21}$$

Note that the fluxes can vary with time, but are assumed to be constant over one time step Δt. An $O(\Delta x)$ method at the boundary is to approximate the derivative using the point next to the boundary point [13], see Figure 4.5, as

$$\frac{p_2^n - p_1^n}{\Delta x} = q_0^n. \tag{4.22}$$

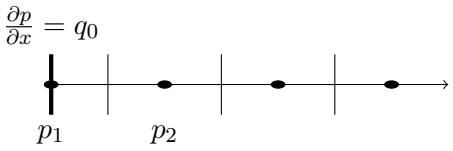

FIGURE 4.5: Setup of our grid with a Neumann BC at the left boundary.

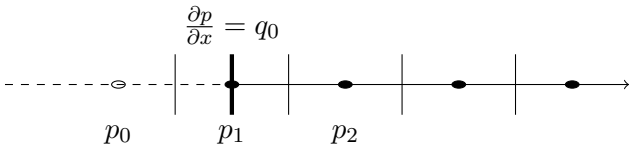

FIGURE 4.6: Setup of a grid with a Neumann BC at the left boundary, using a ghost point.

To incorporate an $O(\Delta x^2)$ method, it it customary to use a so-called ghost point, or a reflection technique [13, 39]. This consists of creating a new point outside the original domain of interest, as shown in Figure 4.6. Discretizing the BC using centered differences then results in

$$\frac{p_2^n - p_0^n}{2\Delta x} = q_0^n, \tag{4.23}$$

which theoretically is used to eliminate p_0^n from the difference equation for the boundary point [13].

In addition to specifying the derivative of the pressure at the boundary, the Neumann BCs can also be used to specify the total flux at the boundary for the pressure equation, as

$$\vec{u}_{\Sigma,0} = q_0^n, \tag{4.24}$$

$$\vec{u}_{\Sigma,L} = q_L^n. \tag{4.25}$$

Note that it is common to talk about and use no-flow boundary conditions, which is a special case of the flux boundary conditions where

$$\vec{u}_\Sigma = 0 \tag{4.26}$$

over the boundary.

Due to the design of the equations of interest for our model, we will use the method in Equation (4.22) for taking care of the Neumann type conditions throughout this thesis, whether they are prescribing values of the derivative of unknowns, or determining the flux over the boundaries. A condition as in Equation (4.22) is easily taken care of and yields the following completion of the implicit system Equation (4.41):

$$\begin{pmatrix} -1 & 1 & 0 & \dots & 0 \\ \vdots & \ddots & \ddots & \ddots & \vdots \\ \vdots & \ddots & \ddots & \ddots & \vdots \\ 0 & \dots & 0 & -1 & 1 \end{pmatrix} [p_1, \dots, p_{N+1}]^{n+1} = \begin{pmatrix} q_0 \Delta x \\ \vdots \\ \vdots \\ q_L \Delta x \end{pmatrix}. \tag{4.27}$$

A no-flow flux condition as Equation (4.26) on both boundaries results in the first and last equation being

$$\begin{pmatrix} 1 & -1 & \dots & 0 \\ \vdots & \ddots & \ddots & \vdots \\ \vdots & \ddots & \ddots & \vdots \\ 0 & \dots & 1 & -1 \end{pmatrix} [p_1, ..., p_{N+1}]^{n+1} = \begin{pmatrix} \frac{\lambda_\Delta}{2\lambda_\Sigma}(p_{c,2} - p_{c,1} - \tau(s_2^{n+1} - s_1^{n+1} - s_2^n + s_1^n)) \\ \vdots \\ \vdots \\ \frac{\lambda_\Delta}{2\lambda_\Sigma}(p_{c,N+1} - p_{c,N} - \tau(s_{N+1}^{n+1} - s_N^{n+1} - s_{N+1}^n + s_N^n)) \end{pmatrix}. \tag{4.28}$$

The Neumann boundary conditions are incorporated in the same fashion, using the same concepts, for the saturation- and transport equation.

Initial conditions

Describing the initial state at the entire domain, thus giving a connection to what has been, is done through initial conditions (ICs). The conditions must be prescribed for all the unknowns at all spatial locations in the domain. For this thesis we will in general require the ICs for average pressure, water saturation and concentration as

$$p(x, t = 0) = [p_1^0, p_2^0, ...p_{N+1}^0]^T =: \mathbf{p}_x^0, \tag{4.29}$$

$$s(x, t = 0) = [s_1^0, s_2^0, ...s_{N+1}^0]^T =: \mathbf{s}_x^0, \tag{4.30}$$

$$c(x, t = 0) = [c_1^0, c_2^0, ...c_{N+1}^0]^T =: \mathbf{c}_x^0. \tag{4.31}$$

4.1.5 Time discretization

For the discretization in time this thesis uses the most well-known fixed step solver, the Euler method. The Euler method consists of computing one calculation per iteration, contrary to methods as the classical Runge-Kutta method which approximates based on four calculations per iteration step. Euler's method can be used as an *implicit* method, seeking the solution at the next time step by implicit dependence on the new solution at that time step

$$y^{n+1} = y^n + f(t^{n+1}, y^{n+1})h. \tag{4.32}$$

Here, h is the increment in time, f is a function depending on t and y, and y is the unknown depending on time. This method is referred to as the *backward* method [13, 39].

The *forward* method on the other hand, is an explicit technique using known values from the last time step to approximate the new solution as

$$y^{n+1} = y^n + f(t^n, y^n)h, \tag{4.33}$$

where h, f and y are as above. Both methods and combinations of them will be used during this work, but in general the approach will be implicit throughout, with most parts being solved fully implicit, and some parts included explicitly.

The explicit approach yields a strict limitation on the time step to ensure convergence of the method. If this limit is exceeded the method may become unstable and diverge strongly from the correct solution. This is not the case for fully implicit methods, but the accuracy of the solution is of course depending on the size of the time step.

4.2 Discretization of the Mathematical Model

In this section we will discuss the discretization of the mathematical model from Chapter 3. We examine the equations one by one, starting with the pressure equation. The results from this section are implemented and serve as the cornerstone for the exploration in the remainder of this thesis. To cope with the fact that dynamic capillarity induces an additional temporal derivative in our model, we develop a new, fully implicit, iterative method. In the case of no dynamic effects, $\tau = 0$, one iteration of the

new method corresponds to the standard IMPES scheme. The idea and setup of this new method is outlined in the following section, and commented on in Section 4.3. The scheme is related to the work presented in the papers [1–3].

4.2.1 The pressure equation

$$\frac{\partial}{\partial x}(-k(\lambda_\Sigma \frac{\partial p}{\partial x} + \frac{1}{2}\lambda_\Delta \frac{\partial}{\partial x}(p_c - \tau \frac{\partial s}{\partial t}))) = \sum_{\alpha=w,n} \frac{F_\alpha}{\rho_\alpha}. \tag{4.34}$$

In the work of discretizing the pressure equation a natural starting point is the general divergence theorem, which works as the fundamental theorem of Calculus in 1D [40], to eliminate the derivative in front of the flux term. Thus, we integrate over a control interval Ω_i, which is the interval $[x_{i-1/2}, x_{i+1/2}]$. This is a practical way of discretizing the equation, by approximating the flux at two points, namely the left hand side and the right hand side of the interval. This results in

$$\int_{x_{i-1/2}}^{x_{i+1/2}} \frac{\partial}{\partial x}(-k(\lambda_\Sigma \frac{\partial p}{\partial x} + \frac{1}{2}\lambda_\Delta \frac{\partial}{\partial x}(p_c - \tau \frac{\partial s}{\partial t})))\mathrm{d}x = \int_{x_{i-1/2}}^{x_{i+1/2}} \sum_{\alpha=w,n} \frac{F_\alpha}{\rho_\alpha}\,\mathrm{d}x. \tag{4.35}$$

By using the divergence term we can rewrite the left hand side as the difference of fluxes over the boundaries, while we discretize the right hand side using the midpoint rule

$$(-k(\lambda_\Sigma \frac{\partial p}{\partial x} + \frac{1}{2}\lambda_\Delta \frac{\partial}{\partial x}(p_c - \tau \frac{\partial s}{\partial t})))_{i+1/2} + (k(\lambda_\Sigma \frac{\partial p}{\partial x} + \frac{1}{2}\lambda_\Delta \frac{\partial}{\partial x}(p_c - \tau \frac{\partial s}{\partial t})))_{i-1/2} = \sum_{\alpha=w,n} \frac{F_{\alpha,i}}{\rho_\alpha}\Delta x_i.$$

A basic assumption of the standard IMPES method is that the static capillary pressure term does not change over a time step, so that one can compute the value of p_c at the previous time step using already known values of the saturation.

In our case, because of the added dynamic capillary pressure, we are iterating several times on the same time step so that the static capillary pressure is always computed at the actual time step. This is included in the notation below, by adding two superscripts where n is the time, and j is an inner loop on each time step. At every new time step, $n+1$, the final solutions from the last time step correspond to the initial value in the

inner loop, $j = 1$,

$$p_i^{n+1,1} = p_i^n, \quad p_{c,i}^{n+1,1} = p_{c,i}^n, \quad \lambda_i^{n+1,1} = \lambda_i^n, \quad \forall \quad i. \tag{4.36}$$

Following this, the iteration provides results for $p^{n+1,j+1}$ until convergence, see Section 4.3.

Approximation of the temporal derivative of s and collation of unknowns terms on the left hand side and known values on the right hand side yields

$$\begin{aligned}
&- k_{i+1/2}\lambda_{\Sigma i+1/2}^{n+1,j}\frac{\partial p_{i+1/2}^{n+1,j+1}}{\partial x} + k_{i-1/2}\lambda_{\Sigma i-1/2}^{n+1,j}\frac{\partial p_{i-1/2}^{n+1,j+1}}{\partial x} = \sum_{\alpha=w,n}\frac{F_{\alpha,i}^{n+1}}{\rho_\alpha}\Delta x_i \\
&+ k_{i+1/2}\frac{1}{2}\lambda_{\Delta i+1/2}^{n+1,j}\left(\frac{\partial p_{c,i+1/2}^{n+1,j}}{\partial x} - \tau\frac{\partial(s_{i+1/2}^{n+1,j} - s_{i+1/2}^n)}{\partial x \Delta t}\right) \\
&- k_{i-1/2}\frac{1}{2}\lambda_{\Delta i-1/2}^{n+1,j}\left(\frac{\partial p_{c,i-1/2}^{n+1,j}}{\partial x} - \tau\frac{\partial(s_{i-1/2}^{n+1,j} - s_{i-1/2}^n)}{\partial x \Delta t}\right).
\end{aligned} \tag{4.37}$$

As noted earlier, the permeability is estimated by the harmonic mean of two adjacent cells as $\bar{k}_i = \frac{2}{\Delta x(\frac{1}{k_i} + \frac{1}{k_{i-1}})}$. This, together with the arithmetic mean of the mobilities and the centered differences for the spatial derivatives from Section 4.1.2, results in

$$\begin{aligned}
&- \bar{k}_{i+1}\frac{\lambda_{\Sigma,i+1}^{n+1,j} + \lambda_{\Sigma,i}^{n+1,j}}{2}\frac{p_{i+1}^{n+1,j+1} - p_i^{n+1,j+1}}{\Delta x} + \bar{k}_i\frac{\lambda_{\Sigma,i}^{n+1,j} + \lambda_{\Sigma,i-1}^{n+1,j}}{2}\frac{p_i^{n+1,j+1} - p_{i-1}^{n+1,j+1}}{\Delta x} = \sum_{\alpha=w,n}\frac{F_{\alpha,i}^{n+1}}{\rho_\alpha}\Delta x_i \\
&+ \frac{1}{2}\bar{k}_{i+1}\frac{\lambda_{\Delta,i+1}^{n+1,j} + \lambda_{\Delta,i}^{n+1,j}}{2}\left(\frac{p_{c,i+1}^{n+1,j} - p_{c,i}^{n+1,j}}{\Delta x} - \tau\frac{s_{i+1}^{n+1,j} - s_i^{n+1,j} - s_{i+1}^n + s_i^n}{\Delta x \Delta t}\right) \\
&- \frac{1}{2}\bar{k}_i\frac{\lambda_{\Delta,i}^{n+1,j} + \lambda_{\Delta,i-1}^{n+1,j}}{2}\left(\frac{p_{c,i}^{n+1,j} - p_{c,i-1}^{n+1,j}}{\Delta x} - \tau\frac{s_i^{n+1,j} - s_{i-1}^{n+1,j} - s_i^n + s_{i-1}^n}{\Delta x \Delta t}\right).
\end{aligned} \tag{4.38}$$

Systematizing in terms of the unknown variable

$$\begin{aligned}
&p_{i+1}^{n+1,j+1}\left(-\bar{k}_{i+1}\frac{\lambda_{\Sigma,i+1}^{n+1,j} + \lambda_{\Sigma,i}^{n+1,j}}{2}\right) + p_{i-1}^{n+1,j+1}\left(-\bar{k}_i\frac{\lambda_{\Sigma,i}^{n+1,j} + \lambda_{\Sigma,i-1}^{n+1,j}}{2}\right) \\
&p_i^{n+1,j+1}\left(-\bar{k}_{i+1}\frac{\lambda_{\Sigma,i+1}^{n+1,j} + \lambda_{\Sigma,i}^{n+1,j}}{2} + \bar{k}_i\frac{\lambda_{\Sigma,i}^{n+1,j} + \lambda_{\Sigma,i-1}^{n+1,j}}{2}\right) \\
&= \sum_{\alpha=w,n}\frac{F_{\alpha,i}^{n+1}}{\rho_\alpha}\Delta x_i^2 + \frac{1}{4}\bar{k}_{i+1}(\lambda_{\Delta,i+1}^{n+1,j} + \lambda_{\Delta,i}^{n+1,j})\left(p_{c,i+1}^{n+1,j} - p_{c,i}^{n+1,j} - \tau\frac{s_{i+1}^{n+1,j} - s_i^{n+1,j} - s_{i+1}^n + s_i^n}{\Delta t}\right) - \\
&\frac{1}{4}\bar{k}_i(\lambda_{\Delta,i}^{n+1,j} + \lambda_{\Delta,i-1}^{n+1,j})\left(p_{c,i}^{n+1,j} - p_{c,i-1}^{n+1,j} - \tau\frac{s_i^{n+1,j} - s_{i-1}^{n+1,j} - s_i^n + s_{i-1}^n}{\Delta t}\right),
\end{aligned} \tag{4.39}$$

and by letting

$$
\begin{aligned}
a_i &= \bar{k}_{i+1}\frac{(\lambda_{\Sigma,i+1}^{n+1,j}+\lambda_{\Sigma,i}^{n+1,j})}{2} \quad \text{for} \quad 1 \le i \le n, \\
b_i &= \sum_{\alpha=w,n}\frac{F_{\alpha,i}^{n+1}}{\rho_\alpha}\Delta x_i^2 + \frac{1}{4}\bar{k}_{i+1}(\lambda_{\Delta,i+1}^{n+1,j}+\lambda_{\Delta,i}^{n+1,j})(p_{c,i+1}^{n+1,j}-p_{c,i}^{n+1,j}-\tau\frac{s_{i+1}^{n+1,j}-s_i^{n+1,j}-s_{i+1}^n+s_i^n}{\Delta t})- \\
&\quad \frac{1}{4}\bar{k}_i(\lambda_{\Delta,i}^{n+1,j}+\lambda_{\Delta,i-1}^{n+1,j})(p_{c,i}^{n+1,j}-p_{c,i-1}^{n+1,j}-\tau\frac{s_i^{n+1,j}-s_{i-1}^{n+1,j}-s_i^n+s_{i-1}^n}{\Delta t}) \quad \text{for} \quad 1 < i \le n,
\end{aligned}
\tag{4.40}
$$

we can formulate this as a linear system $\mathbf{A} = \mathbf{p}^{n+1,j+1}\mathbf{b}$. The system matrix

$$
\mathbf{A} = \begin{bmatrix}
\text{Depending on BCs} & & & & & & \\
-a_1 & a_1+a_2 & -a_2 & 0 & & & 0 \\
0 & -a_2 & a_2+a_3 & -a_3 & 0 & & \\
 & \ddots & \ddots & \ddots & \ddots & \ddots & \\
 & \ddots & -a_{i-1} & a_{i-1}+a_i & -a_{i+1} & \ddots & \\
 & \ddots & \ddots & \ddots & \ddots & \ddots & \\
 & & & 0 & -a_{n-1} & a_{n-1}+a_n & -a_n \\
0 & & & & & \text{Depending on BCs} &
\end{bmatrix},
\tag{4.41}
$$

where the type of BCs determines the first and last equation. This is solved for the average pressure, $\mathbf{p}^{n+1,j+1}$.

4.2.2 The saturation equation

$$
\phi\frac{\partial s}{\partial t} - \frac{\partial}{\partial x}(k\lambda_w(\frac{\partial}{\partial x}(p-\frac{1}{2}p_c+\frac{\tau}{2}\frac{\partial s}{\partial t}))) = \frac{F_w(t,x)}{\rho_w} \tag{4.42}
$$

Solving the saturation equation is done once we have updated the solution for average pressure. Therefore we seek to discretize the saturation equation above using newly updated values of average pressure. First we approximate the temporal derivatives, leading to

$$
\phi\frac{s^{n+1}-s^n}{\Delta t} - \frac{\partial}{\partial x}(k\lambda_w(\frac{\partial}{\partial x}(p^{n+1}-\frac{1}{2}p_c^n+\frac{\tau}{2}\frac{s^{n+1}-s^n}{\Delta t}))) = \frac{F_w^{n+1}}{\rho_w}. \tag{4.43}
$$

Spatial discretization is again performed using TPFA, integrating over a control interval Ω_i, and applying the divergence theorem, yielding

$$\begin{aligned}&\Delta x\phi\frac{s_i^{n+1}-s_i^n}{\Delta t}-(k\lambda_w(\frac{\partial}{\partial x}(p^{n+1}-\frac{1}{2}p_c^{n+1}+\frac{\tau}{2}\frac{s^{n+1}-s^n}{\Delta t})))_{i+1/2}+\\&(k\lambda_w(\frac{\partial}{\partial x}(p^{n+1}-\frac{1}{2}p_c^{n+1}+\frac{\tau}{2}\frac{s^{n+1}-s^n}{\Delta t})))_{i-1/2}=\frac{F_w^{n+1}}{\rho_w}\Delta x,\end{aligned}\tag{4.44}$$

by usage of the midpoint rule and the difference in flux over the boundaries of the interval. At this point, we multiply through by $\Delta x\Delta t$, and reorder the equation with the unknowns at the left hand side so that

$$\begin{aligned}&s_i^{n+1}(\Delta x^2\phi+\frac{\tau}{2}(\bar{k}_{i+1}\lambda_{w,i+1/2}+\bar{k}_{i-1}\lambda_{w,i-1/2})+\\&s_{i+1}^{n+1}(-\frac{\tau}{2}\bar{k}_{i+1}\lambda_{i+1/2})+s_{i-1}^{n+1}(-\frac{\tau}{2}\bar{k}_i\lambda_{i-1/2})=\\&\Delta x^2(\frac{F_{w,i}^{n+1}}{\rho_w}\Delta t+\phi s_i^n)+\\&\Delta t\bar{k}_{i+1}\lambda_{w,i+1/2}(p_{i+1}^{n+1}-p_i^{n+1}-\frac{1}{2}(p_{c,i+1}^{n+1}-p_{c,i}^{n+1}-\tau(s_i^n-s_{i+1}^n)))-\\&\Delta t\bar{k}_i\lambda_{w,i-1/2}(p_i^{n+1}-p_{i-1}^{n+1}-\frac{1}{2}(p_{c,i}^{n+1}-p_{c,i-1}^{n+1}-\tau(s_{i-1}^n-s_i^n))),\end{aligned}\tag{4.45}$$

where we have approximated the derivatives and the mobilities in the same manner as before. Once again we introduce the second superscript j, where $j+1$ is denoting unknown values, and j are known values. As earlier we use the solution from the last time step as an initial guess for the first j-value

$$s_i^{n+1,1}=s_i^n\quad\forall\quad i,\tag{4.46}$$

so that the full discretization is

$$
\begin{aligned}
&s_i^{n+1,j+1}(\Delta x^2\phi + \frac{\tau}{2}(\bar{k}_{i+1}\lambda_{w,i+1/2}^{n+1,j} + \bar{k}_{i-1}\lambda_{w,i-1/2}^{n+1,j})+\\
&s_{i+1}^{n+1,j+1}(-\frac{\tau}{2}\bar{k}_{i+1}\lambda_{i+1/2}^{n+1,j}) + s_{i-1}^{n+1,j+1}(-\frac{\tau}{2}\bar{k}_i\lambda_{i-1/2}^{n+1,j}) =\\
&\Delta x^2(\frac{F_{w,i}^{n+1}}{\rho_w}\Delta t + \phi s_i^n)+\\
&\Delta t\bar{k}_{i+1}\lambda_{w,i+1/2}^{n+1,j}(p_{i+1}^{n+1,j+1} - p_i^{n+1,j+1} - \frac{1}{2}(p_{c,i+1}^{n+1,j} - p_{c,i}^{n+1,j} - \tau(s_i^n - s_{i+1}^n)))-\\
&\Delta t\bar{k}_i\lambda_{w,i-1/2}^{n+1,j}(p_i^{n+1,j+1} - p_{i-1}^{n+1,j+1} - \frac{1}{2}(p_{c,i}^{n+1,j} - p_{c,i-1}^{n+1,j} - \tau(s_{i-1}^n - s_i^n))).
\end{aligned}
\tag{4.47}
$$

Letting

$$
\begin{aligned}
&d_i = \frac{\tau}{4}(\bar{k}_i(\lambda_{w,i}^{n+1,j} + \lambda_{w,i-1}^{n+1,j})),\\
&e_i = \Delta x^2(\frac{F_{w,i}^{n+1}}{\rho_w}\Delta t + \phi s_i^n)+\\
&\Delta t\bar{k}_{i+1}\lambda_{w,i+1/2}^{n+1,j}(p_{i+1}^{n+1,j+1} - p_i^{n+1,j+1} - \frac{1}{2}(p_{c,i+1}^{n+1,j} - p_{c,i}^{n+1,j} - \tau(s_i^n - s_{i+1}^n)))-\\
&\Delta t\bar{k}_i\lambda_{w,i-1/2}^{n+1,j}(p_i^{n+1,j+1} - p_{i-1}^{n+1,j+1} - \frac{1}{2}(p_{c,i}^{n+1,j} - p_{c,i-1}^{n+1,j} - \tau(s_{i-1}^n - s_i^n))),
\end{aligned}
\tag{4.48}
$$

this can be expressed and solved as a system $\mathbf{B} = \mathbf{s}^{n+1,j+1}\mathbf{e}$, where

$$
\mathbf{B} = \begin{bmatrix}
\text{Depending on BCs} & \dots & \dots & \dots & 0\\
-d_1 & d_1 + d_2 + \Delta x^2\phi & -d_2 & 0 & \\
0 & -d_2 & d_2 + d_3 + \Delta x^2\phi & -d_3 & 0\\
\vdots & \ddots & \ddots & \ddots & \vdots\\
\vdots & 0 & -d_{n-1} & d_{n-1} + d_n + \Delta x^2\phi & -d_n\\
0 & \dots & \dots & \text{Depending on BCs} &
\end{bmatrix},
$$

and the type of BCs determines the first and last equation. The system above is solved for the saturation at the new time step $n+1$, and iteration step $j+1$, yielding $\mathbf{s}^{n+1,j+1}$.

After solving for the two-phase flow at iteration step $j+1$, the static capillary pressure is updated to $p_c^{n+1,j+1}$, and both functions for mobilities are updated to $\lambda_\Delta^{n+1,j+1}$, $\lambda_\Sigma^{n+1,j+1}$, based on the newly updated saturation. Thereafter the procedure is repeated until convergence, see Section 4.3.

4.2.3 The transport equation

$$\phi\frac{\partial(sc)}{\partial t}+\frac{\partial}{\partial x}(-\frac{\partial}{\partial x}(\phi Dsc)+u_w c)=Q(t,x) \tag{4.49}$$

After having accepted the solutions for both the pressure and the saturation at the new time, using the new scheme, we compute the concentration c, using purely implicit techniques. Starting as with the saturation equation, approximating the temporal derivative, results in

$$\phi\frac{s^{n+1}c^{n+1}-s^n c^n}{\Delta t}+\frac{\partial}{\partial x}(-\frac{\partial}{\partial x}(\phi Ds^{n+1}c^{n+1})+u_w c^{n+1})=Q(t,x), \tag{4.50}$$

which when applying the TPFA method over an interval Ω_i yields

$$\begin{aligned}&\Delta x\phi\frac{s_i^{n+1}c_i^{n+1}-s_i^n c_i^n}{\Delta t}+\left(-\frac{\partial}{\partial x}\left(\phi Dc^{n+1}c^{n+1}\right)+u_w c^{n+1}\right)_{i+1/2}\\&-\left(-\frac{\partial}{\partial x}\left(\phi Dc^{n+1}c^{n+1}\right)+u_w c^{n+1}\right)_{i-1/2}=Q_i^{n+1}\Delta x.\end{aligned} \tag{4.51}$$

Using previously described techniques for approximating the derivatives and arithmetically averaging the water flux gives

$$\begin{aligned}&c_i^{n+1}(\frac{\Delta x\phi}{\Delta t}s_i^{n+1}+\frac{1}{2}(u_{w,i+1/2}+u_{w,i-1/2})+2\frac{\phi D}{\Delta x}s_i^{n+1})+\\&c_{i-1}^{n+1}(-\frac{1}{2}u_{w,i-1/2}-\frac{\phi D}{\Delta x}s_{i-1}^{n+1})+c_{i+1}^{n+1}(-\frac{1}{2}u_{w,i+1/2}-\frac{\phi D}{\Delta x}s_{i+1}^{n+1})=\\&Q_i^{n+1}\Delta x+\frac{\Delta x\phi}{\Delta t}s_i^n c_i^n,\end{aligned} \tag{4.52}$$

after some manipulation, where all the unknowns are on the left hand side. Introducing

$$Y=\frac{\Delta x\phi}{\Delta t}, \tag{4.53}$$

$$Z=\frac{\phi D}{\Delta x}, \tag{4.54}$$

$$f_i=\frac{1}{2}(u_{w,i+1}+u_{w,i}), \tag{4.55}$$

and

$$g_i=Y(s_i^n c_i^n)+Q_i^{n+1}\Delta x, \tag{4.56}$$

to simplify notation, we can write the system of equations $\mathbf{D} = \mathbf{c}^{n+1}\mathbf{g}$.
Hence, the system matrix

$$\mathbf{D} = \begin{bmatrix} \text{Depending on BCs} & \dots & \dots & 0 \\ -f_1 - Zs_1^{n+1} & f_2 - f_1 + (2Z+Y)s_2^{n+1} & f_2 - Ys_3^{n+1} & \\ \vdots & \ddots & \ddots & \ddots \\ \vdots & f_{N-1} - Zs_{N-1}^{n+1} & f_N - f_{N-1} + (2Z+Y)s_N^{n+1} & f_N - Ys_{N+1}^{n+1} \\ 0 & \dots & & \text{Depending on BCs} \end{bmatrix}$$

and the 1st and last equation depends on boundary conditions, as outlined in Section 4.1.4. This system is solved for the concentration at the new time step, $\mathbf{c}^{n+1}$.

Stability of the standard IMPES method versus our new scheme

Due to the fact that the IMPES method utilizes explicit techniques, it is necessary to control the time step in order to guarantee the stability of the method. A numerical algorithm is considered to be stable if any errors introduced at some stage does not grow during the subsequent iterations. The stability criterion for the standard IMPES method with my choice of primary variables is as following [39];

$$\Delta t < \frac{1}{2}\Delta x^2 \, \min\left(\frac{\phi}{\bar{k}_i}\right) \frac{1}{\max\left|\frac{\partial p_c(s)}{\partial x}\right|} \, \min\left(\frac{\mu_n}{k_{r,n}(s)} + \frac{\mu_w}{k_{r,w}(s)}\right), \tag{4.57}$$

which informs us that the time step must be controlled in order to guarantee stability of the method. For our new iterative scheme, we expect no stability problems due to the fact that the scheme is fully implicit. The convergence of the scheme is still to be analyzed theoretically, while in this work we concentrate on studying this numerically.

We have in our work compared the IMPES approach to the new scheme numerically, by verifying that the new scheme is stable for time steps where the IMPES approach fails due to instability. This has however not been done systematically, thus no results are included.

4.3 Implementation

All our three system Equations (4.41), (4.49) and (4.57) are implemented and solved using MATLAB, a numerical computing environment suitable for our purpose. The discretized systems are implemented in a function which is run by a main script, where all the variables, physical parameters and initial- and boundary conditions can be changed. To cope with the fact that we, due to the includement of the dynamic capillarity, have an extra temporal derivative, we have developed a new iterative scheme to handle the two-phase flow model.

The new iterative scheme is derived in the spirit of the publications [1, 2], an alternative approach being the Newton method [43–45], which is quadratic but only locally convergent. For convergence analysis of flow and/or reactive transport in porous media, we also refer to [46–51].

For each progression in time, from time n to time $n+1$, we solve an additional inner loop to ensure convergence of the approximation of $\mathbf{p}^{n+1}$ and $\mathbf{s}^{n+1}$. This is done by including a second superscript as $\mathbf{p}^{n+1,j}$, $\mathbf{s}^{n+1,j}$, solving the two-phase model for $\mathbf{p}^{n+1,j+1}$, $\mathbf{s}^{n+1,j+1}$, as described in Sections 4.2.1 and 4.2.2. This iteration is repeated with updated values for p_c, λ_Δ and λ_Σ until convergence, that is when the increment between the previous and new j-step for both variables, measured in an L_2 norm as defined later, in Section 4.4.3, is below a certain tolerance limit, ϵ. Mathematically, if both

$$\|\mathbf{p}^{n+1,j+1} - \mathbf{p}^{n+1,j}\|_{L_2} < \epsilon \quad \text{and} \tag{4.58}$$

$$\|\mathbf{s}^{n+1,j+1} - \mathbf{s}^{n+1,j}\|_{L_2} < \epsilon, \tag{4.59}$$

the approximations are accepted and are used for the computation of $\mathbf{c}^{n+1}$. The concentration is not a part of the iterative loop and is implemented as described in the previous section.
As a security measure we include a return statement in the implementation, together with a maximum number of inner iterations, to prevent the code from running in the case when it is producing non-converging results.

All systems in our implementation are consisting of a strictly sparse system matrix, and are therefore solved effectively by using the direct solver in MATLAB. See Figure 4.15 for a schematic solution strategy.

4.4 Code Validation and Parameterizations

Before we start exploring MEOR activities and the effect of dynamic capillary pressure, we must validate our implementation. We do this by separately validating the two-phase flow model and the transport model, using accepted results from the literature for the flow model and an analytical solution to validate and analyze the convergence of the transport equation.

4.4.1 van Genuchten parameterization

Throughout this thesis the van Genuchten parameterization will be used for the constitutive relations between relative permeabilities and water saturation, and between static capillary pressure and water saturation. These are, see [29, 52, 53],

$$\begin{aligned} p_c(s^*(s)) &= p_e(s^{*-1/m} - 1)^{1/n}, \\ k_{r,w}(s^*(s)) &= \sqrt{s^*}[1 - (1 - s^{*1/m})^m]^2, \\ k_{r,n}(s^*(s)) &= \sqrt{1 - s^*}(1 - s^{*1/m})^{2m}, \end{aligned} \tag{4.60}$$

where n, m and the entry pressure, p_e, are model dependent van Genuchten parameters, and s^* is the effective saturation. The common way to approximate m is as $m = 1 - 1/n$. The functions for static capillary pressure and relative permeabilities fulfill the criteria that

- $p_c(s^*(s))$ is continuously differentiable $\forall s^* \in [0, 1]$,
- $p_c(s^*(s))$ is monotonous decreasing and $p_c(1) = 0$,
- $k_{r,n}$ is monotonous decreasing, $k_{r,n}(1) = 0$, $k_{r,n}(0) = 1$,
- $k_{r,w}$ is monotonous increasing, $k_{r,w}(0) = 0$, $k_{r,w}(1) = 1$.

Curves for the van Genuchten parameterizations are shown in Figures 4.7 and 4.8.

Related to the above it is worth mentioning that this parameterization, based solely on a constitutive relation between static capillary pressure and water saturation, and relative permeabilities and water saturation, is not fully descriptive. In reality the residual, or immobilized, water and oil saturation will depend on conditions that changes over time,

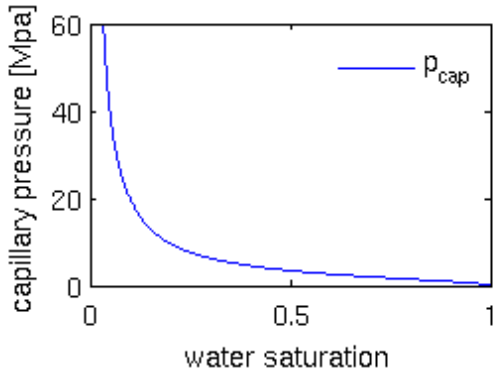

FIGURE 4.7: Example of van Genuchten static capillary pressure, for $s_{res} = 0$, $s_{max} = 1$, $p_e = 2$ MPa and $n = 2$.

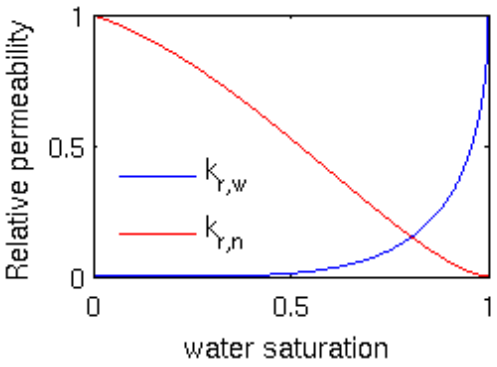

FIGURE 4.8: Example of van Genuchten relative permeabilities, for $s_{res} = 0$, $s_{max} = 1$, $p_e = 2$ MPa and $n = 2$.

such as flow velocity. Additionally, the static capillary pressure and relative permeabilities will exhibit the well-known hysteretic behavior, based on the sign of $\partial_t s$ [54], which requires a more sophisticated functional that this work does not include (see e.g. [55]).

The practical importance is yet undeniable as the model in most cases is able to replicate the reality good enough. However, the model will be expanded throughout this work to account for potential microbial effects, see Section 5.2.1.

4.4.2 Validation of the two-phase flow model

To validate the two-phase flow model we make use of two separate examples from the literature. The first shows an injection of gas into the left side of the domain, implicitly included through the Dirichlet boundary condition describing the water saturation, while the second example accounts explicitly for an injection of gas in the middle of our domain.

TABLE 4.1: Parameters for two-phase flow model validation 1

Property	Value	Property	Value
ϕ	0.1	s_{res}	0
k	1 mD	s_{max}	1
μ_n	$9 \cdot 10^{-6}$ Pa $\cdot$ s	τ	0
μ_w	$7.98 \cdot 10^{-3}$ Pa $\cdot$ s	n	2
ρ_w	10^3 kg/m^3	L	100 m
ρ_n	0.808 kg/(m^{3}MPa) $\cdot\, p_n$	p_{entry}	2 MPa

Example 1

The settings of the first problem follows the paper by Amaziane, Jurak and Keko [56]. Our two-phase flow model is solved on the same one dimensional domain, $[0, L]$, by using the van Genuchten parameterizations as introduced in Section 4.4.1. Table 4.1 shows fluid and matrix parameters, in addition to the length of the domain, L, and the van Genuchten parameters.

It is worth emphasizing that we have made a slight alteration from the simulation in [56], by assuming the gaseous phase to be incompressible with constant density $\rho_n = 2\ \mathrm{kg/m^3}$. We also remark that they solve for global pressure, whereas we solve for mean pressure in addition to phase pressures, and that the dynamic capillary coefficient τ=0.

The simulation was performed with the following boundary and initial conditions

$$p(0,t) = 1.8, \quad s(0,t) = 0.4, \quad p(L,t) = 0.1, \quad \frac{\partial s}{\partial x}(L,t) = 0,$$
$$s(x,0) = 1, \quad p(x,0) = 0.1,$$

and with both source terms equal to zero.

This simulation yielded the results shown in Figures 4.9 and 4.10 at a final time of 40 days.

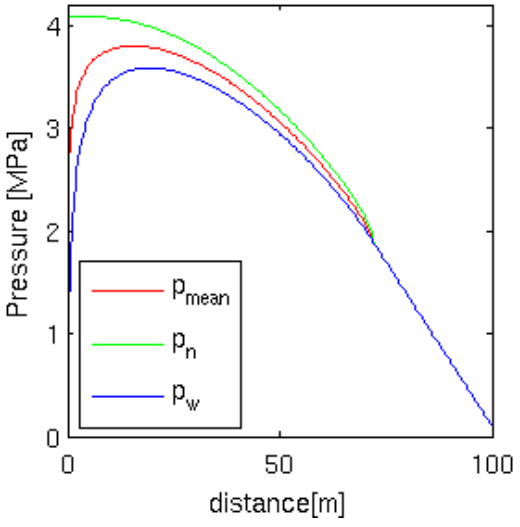

FIGURE 4.9: Example 1: Mean and phase pressures after t=40 days.

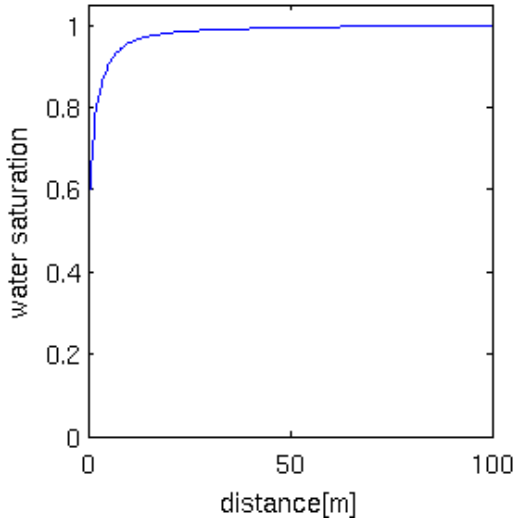

FIGURE 4.10: Example 1: Water saturation after t=40 days.

When comparing with [56] we see a strong correlation between their results and ours. Note that they are not perfectly identical, the non-wetting pressure is a bit imprecise due to the fact that we did not take into account the effects of compressibility.

Example 2

Secondly we compare our code by using the example defined in [52]. The fluid and solid properties are mainly the same, apart from the viscosity of the gaseous phase, which is here $\mu_n = 0.86 \cdot 10^{-3}$ Pa $\cdot$ s. We add a constant source term of gas in the interval $[47\text{ m}, 53\text{ m}]$ of $F_n = 0.01$ kg/day, and make a slight alteration from the simulation in [52], by assuming that the gas density does not change over a time step Δt.

The simulation was performed with the following boundary and initial conditions

$$p(0,t) = 0.1, \quad s(0,t) = 1, \quad p(L,t) = 0.1, \quad s(L,t) = 1,$$
$$s(x,0) = 1, \quad p(x,0) = 0.1,$$

yielding the results shown in Figures 4.11 and 4.12 at a final time of 12 days.

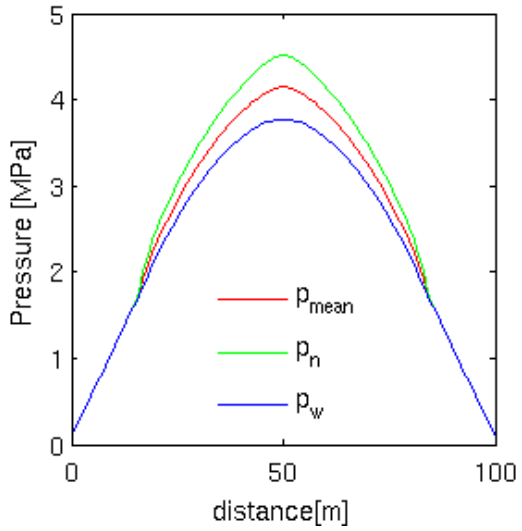

FIGURE 4.11: Example 2: Mean and phase pressures after t=12 days.

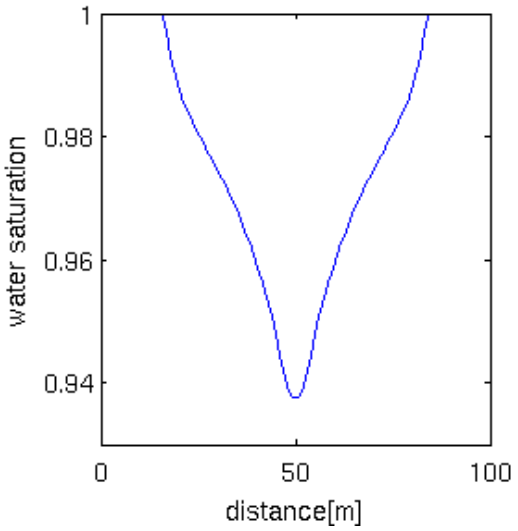

FIGURE 4.12: Example 2: Water saturation after t=12 days.

Again, the results obtained are very much consistent with what is found in [52].

These two results give us an understanding that the two-phase flow model implemented is consistent with the physics and numerical results from others, and thus qualifies for further exploration.

4.4.3 Validation of the transport model

To validate the implementation of the transport model we use an analytical solution, which gives us an opportunity to analyze the convergence of the implementation. In the simple case we let the water flux u_w, the water saturation s and the porosity ϕ be equal to 1, and the source term Q to be equal to zero. The dispersion-diffusion coefficient is set to be $D = 0.01$.
The equation at hand is therefore simplified to

$$\frac{\partial c}{\partial t} = -u\frac{\partial c}{\partial x} + D\frac{\partial^2 c}{\partial x^2}. \tag{4.61}$$

We construct an analytical solution as given in [57], where the following is given in $T \times \Omega = [0, 0.5] \times [0, 1]$:

The exact solution,

$$c_{ana}(t, x) = \frac{0.025}{\sqrt{0.000625 + 0.02t}} \exp\left(-\frac{(x + 0.5 - t)^2}{0.00125 + 0.04t}\right), \tag{4.62}$$

the boundary conditions,

$$c(t, 0) = \frac{0.025}{\sqrt{0.000625 + 0.02t}} \exp\left(-\frac{(0.5 - t)^2}{0.00125 + 0.04t}\right), \tag{4.63}$$

$$c(t, 1) = \frac{0.025}{\sqrt{0.000625 + 0.02t}} \exp\left(-\frac{(1.5 - t)^2}{0.00125 + 0.04t}\right), \tag{4.64}$$

and the initial condition,

$$c(0, x) = \exp\left(-\frac{(x + 0.5)^2}{0.00125}\right). \tag{4.65}$$

The Euclidean norm

We now seek to validate our numerical implementation, as well as analyzing the convergence of it, by comparing the numerical solution with the analytical solution for various

grid sizes and time steps. The comparison is done with respect to the Euclidean norm, or the L_2 norm, as well as the infinity norm. We define on $L_2(0,1)$ the scalar product as

$$(f,g)_{L_2} = \int_0^1 f(x)g(x)\,\mathrm{d}x \quad \forall \quad f,g \in L_2(0,1), \tag{4.66}$$

with the associated vector norm

$$\|f\|_{L_2} = \sqrt{(f,f)_{L_2}} = \sqrt{\int_0^1 f^2\,\mathrm{d}x}. \tag{4.67}$$

In our comparison we use this to compute the L_2 norm of the error $E = |c_{ana} - c_{num}|$ as

$$\|c_{ana} - c_{num}\|_{L_2} = \sqrt{(c_{ana} - c_{num}, c_{ana} - c_{num})_{L_2}} = \sqrt{\int_0^1 (c_{ana} - c_{num})^2\,\mathrm{d}x}, \tag{4.68}$$

approximating the integral by usage of the midpoint rule from Section 4.1.2

$$\|c_{ana} - c_{num}\|_{L_2} = \sqrt{\sum_{i=1}^{n} \int_{x_{i-1/2}}^{x_{i+1/2}} (c_{ana} - c_{num})^2\,\mathrm{d}x} \approx \sqrt{\Delta x \sum_{i=1}^{n} (c_{ana,i} - c_{num,i})^2}, \tag{4.69}$$

for an equidistant grid. The maximum norm is computed as

$$\|c_{ana} - c_{num}\|_{\infty} = \max_{i=1}^{n} |c_{ana} - c_{num}|_i \quad \forall \quad i. \tag{4.70}$$

The simulations are initially done with coarse resolution, which is refined several times by a factor 2. Δx and Δt are kept equal, resulting in what is presented in Figure 4.13 and table 4.2. The reduction is computed as the previous error relative to the new error. By this we can verify that our model is converging, and by the reduction computed we can ascertain that the model is of $O(\Delta t, \Delta x)$, see Figure 4.14.

TABLE 4.2: Error analysis for the numerical solution of the transport equation

Δx	Δt	L_2 error	reduction	∞ norm	reduction
0.1	0.1	0.25115010452	-	0.04967906036	-
0.05	0.05	0.16492175678	1.522843980	0.03240072760	1.5332698996
0.025	0.025	0.09557610089	1.725554351	0.01931483324	1.67750491
0.0125	0.0125	0.05172816959	1.847660600	0.01069415672	1.8061109211
0.00625	0.00625	0.02696745073	1.918170542	0.00563489752	1.8978440473

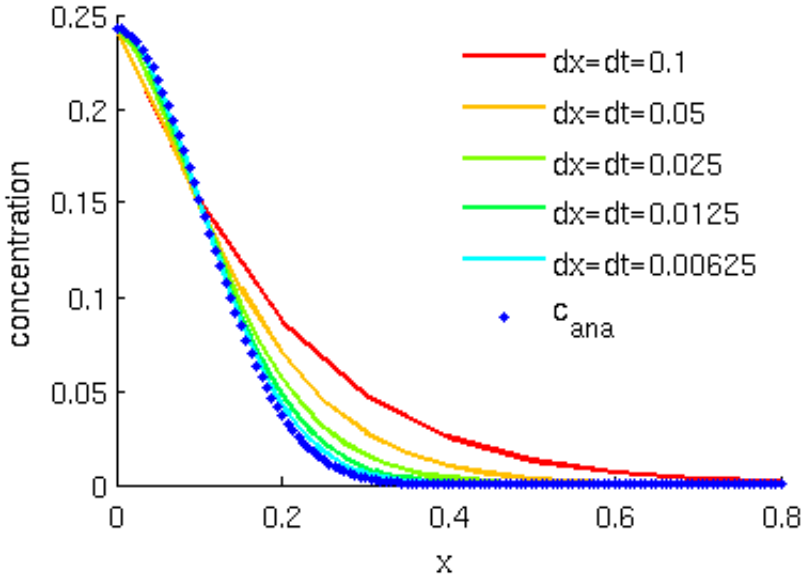

FIGURE 4.13: The analytical solution compared with numerical solutions for different resolutions.

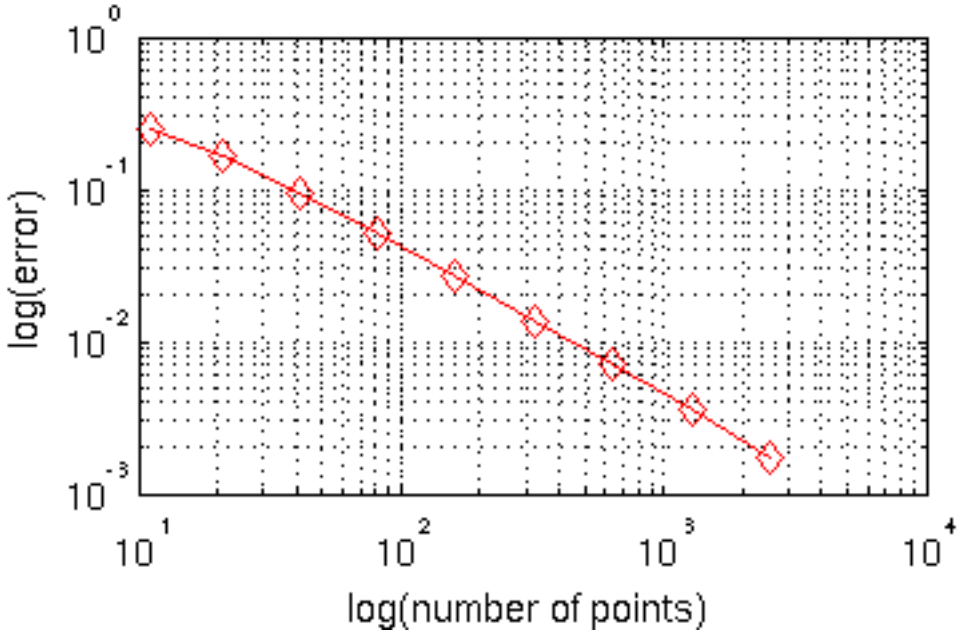

FIGURE 4.14: Log-log plot of the error versus number of points.

After the separate validation is performed, we couple the whole system together, and reproduce the results to validate that the coupling is done correctly. Our whole scheme is then solved as outlined in Figure 4.15.

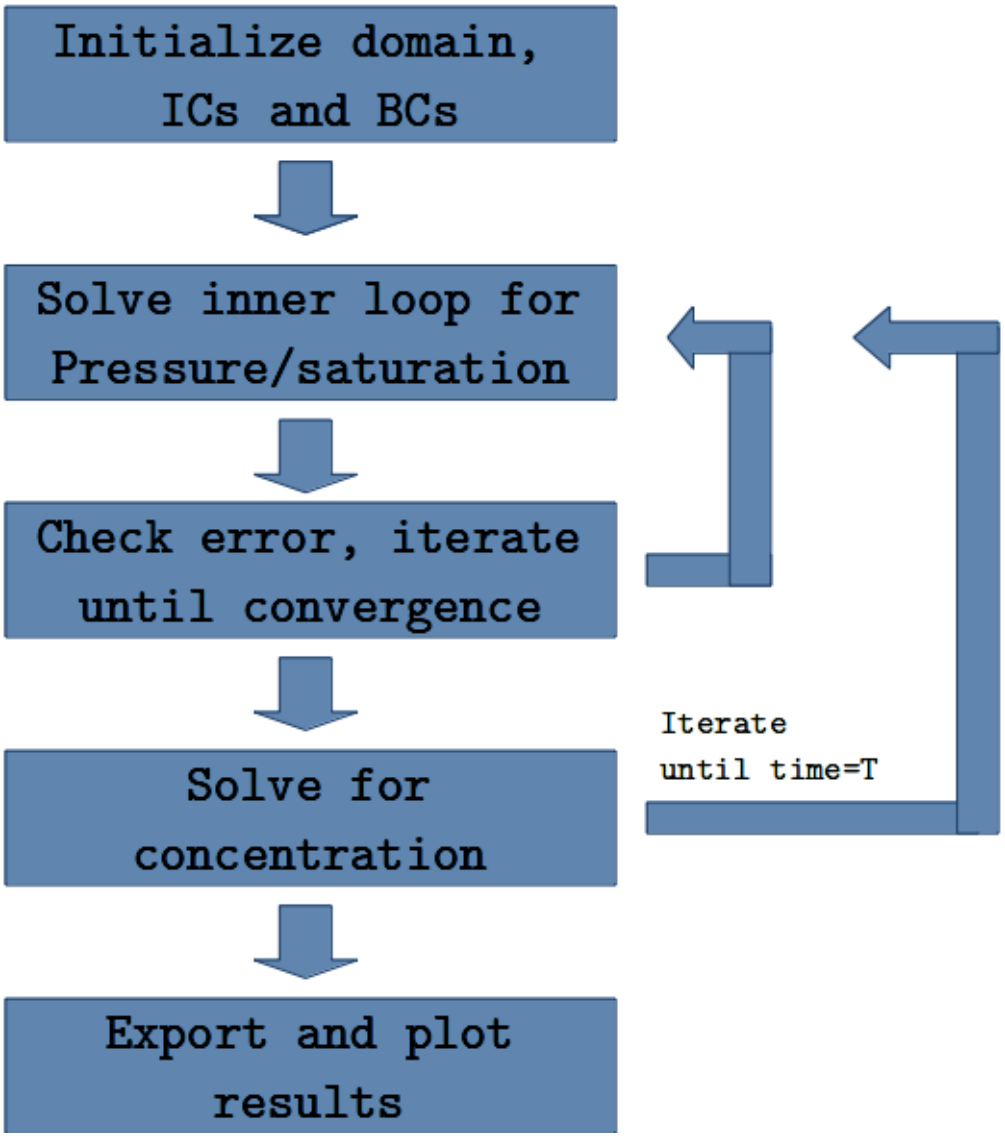

FIGURE 4.15: Solving the fully coupled model until $t = T$.

Chapter 5

The Effects of MEOR and Dynamic Capillary Pressure

In this chapter we will make use of our coupled model to explore the effects of MEOR. We will compare different approaches and quantify the produced oil in terms of barrels. As well we will model the effect of dynamic capillary pressure, and also explore the effects of some chosen parameters through sensitivity analysis. Finally, convergence history of the new inner loop is numerically examined.

5.1 Reference Reservoir

We start by defining a reference reservoir, see Figure 5.1, to compare different approaches. The reservoir has an initial saturation of water of $s(0, x) = 0.3$, meaning that there is 70 % oil left in the reservoir after initial recovery. The reservoir and fluid properties are listed in Table 5.1.

To compare different approaches we need to identify the goal, which undoubtedly is to mobilize and recover as much of the oil as possible. Thus, we introduce the typical petroleum unit barrel, bbl, in this context. 1 bbl $\approx$ 159 liters, and given our constant oil density this gives us a relationship between mass and volume as

$$1 \text{ bbl} \approx 159 \text{ liters} \cdot \rho_o = 0.159 \text{ m}^3 \cdot 770 \text{ kg/m}^3 = 122.43 \text{ kg}. \tag{5.1}$$

Property	Value	Property	Value
ϕ	0.25	D	3 m^2/day
k	200 mD	σ_0	40 mN/m
μ_o	$3 \cdot 10^{-3}$ Pa · s	σ_{min}	0.06 mN/m
μ_w	$1 \cdot 10^{-3}$ Pa · s	α	0.5
ρ_w	1020 kg/m^3	s_{max}	0.59
ρ_o	770 kg/m^3	s_{res}	0.1
p_{entry}	1 MPa	$p(0,x)$	5 MPa
A	1000 m^2	L	300 m
$s(0,x)$	0.3	n	2

TABLE 5.1: Properties reference reservoir

OIP, the oil in place, is found numerically at time step n as

$$\text{OIP}(n) = \frac{AL}{N}(\sum_{i=2}^{N}(1 - s_i^n) + 0.5(2 - s_1^n - s_{N+1}^n)), \tag{5.2}$$

where A is the cross-sectional area and L the length of the reservoir, n is the time and N is the number of intervals. Further,

$$\text{OOIP} = \text{OIP}(0) = \frac{AL}{N}(\sum_{i=2}^{N}(1 - s_i^0) + 0.5(2 - s_1^0 - s_{N+1}^0)), \tag{5.3}$$

$$\text{OOIP} \approx 1.32 \text{ million bbl}, \tag{5.4}$$

is the original oil in place. Using this we can calculate the production per time step and the total production as

$$\text{Production/time step} = \text{OIP}(n-1) - \text{OIP}(n), \tag{5.5}$$

$$\text{Total production} = \text{OOIP} - \text{OIP}(n). \tag{5.6}$$

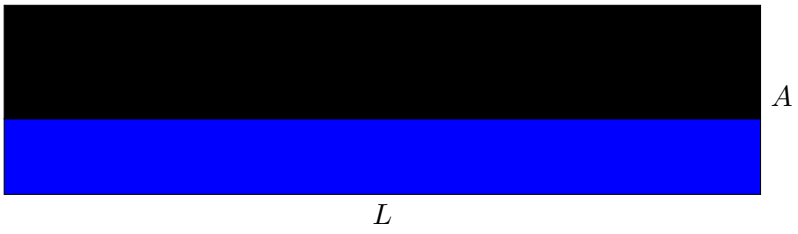

FIGURE 5.1: The reference reservoir with length L = 300 m, cross-sectional area A = 1000 m^2, and initial water saturation of s=0.3.

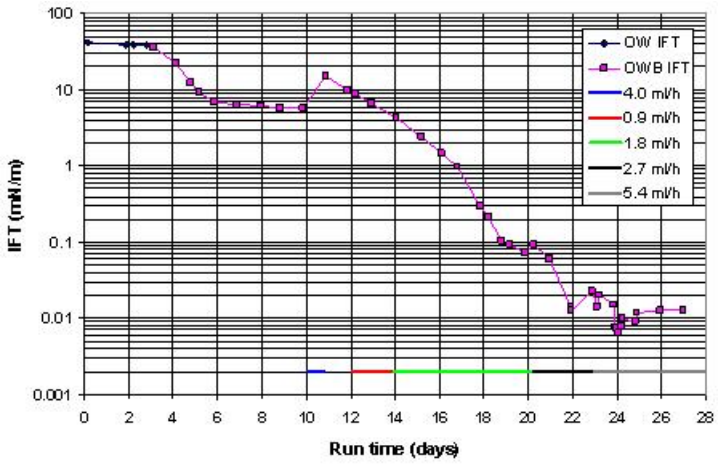

FIGURE 5.2: Drop in IFT from $38 - 0.06$ mN/m, due to bacterial effects as a function of run time in days, from [4].

5.2 IFT Reduction - Possible Effects

This section is devoted to investigation of the most promising mechanism of MEOR, the possible reduction of interfacial tension due to activity of surfactants on the interface between oil and water. To do so, we need to link the reduction in IFT with a reduction in static capillary pressure. This link is obvious through the Young-Laplace equation Equation (3.6), and thus we seek to include such effects in the parameterization of p_c, $k_{r,w}$ and $k_{r,n}$.

5.2.1 Capillary pressure, residual oil and relative permeabilities as functions of concentration

In [4], two separate experimental results show a reduction of IFT. The first shows a drop of IFT from $35 - 0.17$ mN/m, while the second shows a drop from $38 - 0.06$ mN/m, due to bacterial activity, see Figure 5.2. Based on these results we suggest a simple, exponential relationship between concentration, c, and interfacial tension, σ, as

$$\sigma(c) = (\sigma_0 - \sigma_{min})\, \mathrm{e}^{-\alpha c} + \sigma_{min}. \tag{5.7}$$

Above, σ_0 is the IFT when no microbes are present, σ_{min} is the lowest possible value of the IFT and α is a coefficient determined by the effects of microbial activity. Notice

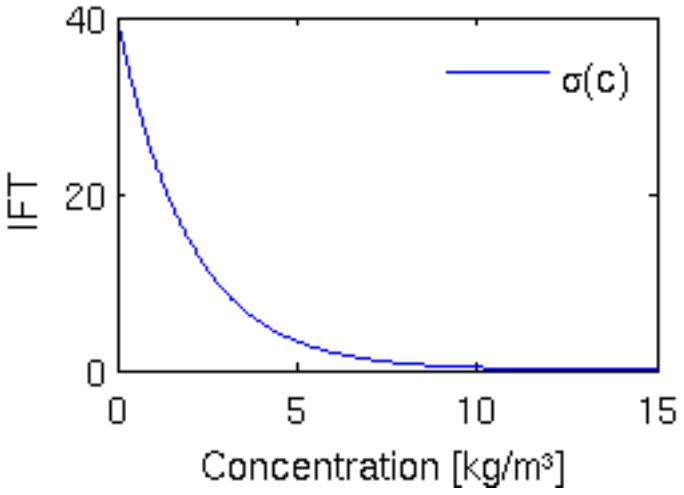

FIGURE 5.3: Example of our relationship $\sigma(c)$, for α=0.5, σ_{min} = 0.06 mN/m and σ_0 = 40 mN/m.

that we do not take into account the time aspect, as we assume immediate effect. This may be seen as a weakness of the parameterizations compared to Figure 5.2.

Capillary pressure

To couple the effect of the IFT reduction with the static capillary pressure, we include the effects in the entry pressure, p_e, which is the sought-after, possible effect [5, 22]. We express the entry pressure as

$$p_e(c) = \frac{p_{e,0}}{\sigma_0}(\sigma(c)) = \beta((\sigma_0 - \sigma_{min})\,\mathrm{e}^{-\alpha c} + \sigma_{min}), \tag{5.8}$$

where $p_{e,0}$ corresponds to the entry pressure in the case of no reduction in the interfacial tension. This, together with the previously introduced van Genuchten parameterization for the relationship between p_c and s^* from Section 4.4.1, results in a function relating concentration, effective saturation and capillary pressure. Hence,

$$p_c(s^*, c) = \frac{p_{e,0}}{\sigma_0}((\sigma_0 - \sigma_{min})\,\mathrm{e}^{-\alpha c} + \sigma_{min})(s^{*-1/m} - 1)^{1/n}, \tag{5.9}$$

where $m = 1 - 1/n$ and n is the model dependent van Genuchten parameter as before.

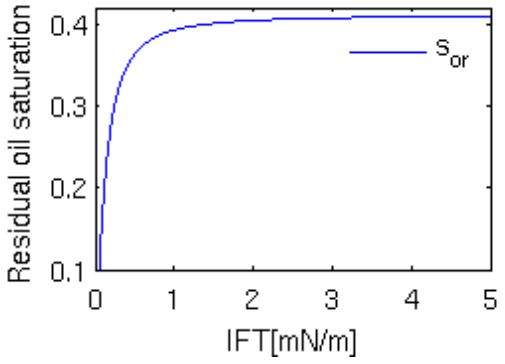

FIGURE 5.4: Example of the effects of IFT reduction on residual oil content, for $s_{o,res,initial} = 0.41$.

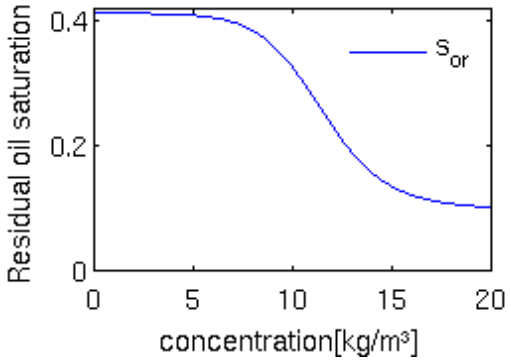

FIGURE 5.5: Example of a relationship between concentration and residual oil, for $s_{o,res,initial} = 0.41$.

The residual oil saturation

As an effect of the reduction of IFT the amount of residual, or immobilized, oil may decrease. Experiments from [6] predicts a correlation between IFT and residual oil saturation as

$$s_{o,res} = \frac{\sigma}{A\sigma + B}, \tag{5.10}$$

where A and B are constants depending on reservoir conditions. In our case, we choose to use the same constants as the authors (A=2.432, B=0.1154), so that our expression for the maximum water saturation, s_{max}, which is our parameter in Equation (3.3) becomes

$$s_{max}(c) = 1 - s_{o,res}(c) = 1 - \frac{\sigma(c)}{2.432\sigma(c) + 0.1154}, \tag{5.11}$$

corresponding to an initial residual oil saturation of 0.41.

Relative permeabilities

Recall the standard van Genuchten relative permeabilities curves of Section 4.4.1

$$k_{r,w}(s^*(s)) = \sqrt{s^*}[1 - (1 - s^{*1/m})^m]^2, \tag{5.12}$$

$$k_{r,n}(s^*(s)) = \sqrt{1 - s^*}(1 - s^{*1/m})^{2m}. \tag{5.13}$$

Relative permeabilities rule the flow of the different phases through porous media, and experiments have shown that as the IFT between water and oil is reduced, the slope of

these curves tend to move towards straighter lines [6–8]. It is also shown that, as for the residual oil saturation, the effects are small for IFT-values above 1 mN/m.

We seek to include such effects in our parameterizations, and do so by determining a dependence of $k_{r,n}$ and $k_{r,w}$ on the concentration c. This is done by including the effects in the exponent m, which governs the slope of the curve. For the oleic phase, we include the effects by reducing m for low values of IFT (i.e. below 1 mN/m), and for the wetting phase we do the opposite, by increasing m.

We define the lowest possible value for the oleic parameter, m_o=0.1, and the highest possible value for the wetting parameter, m_n=1.3, both for $\sigma = 0.01$ mN/m, which is not reachable in practical applications. As we only want to model permeability-changes for IFT-values below 1 mN/m, we construct one point for the water parameter at (σ, m_w)=(0.1,0.9), and for the oleic parameter at (σ, m_o)=(0.1,0.3), and use this together with the minimum value described above, and the value m_0 at $\sigma = 1$ mN/m. Logarithmic regression gives us useful relationships for the parameters based on IFT as

$$\begin{aligned} m_w(\sigma(c)) &= 0.5 - 0.17\ln(\sigma(c)), \qquad \forall\sigma < 1 \text{ mN/m}, \\ m_o(\sigma(c)) &= 0.5 + 0.09\ln(\sigma(c)), \qquad \forall\sigma < 1 \text{ mN/m}, \end{aligned} \tag{5.14}$$

where m_0 has been fixed at a value of 0.5, which is the parameter used throughout this work. This results in the relative permeabilities being

$$\begin{aligned} k_{r,w}(m_w(\sigma(c)), s^*(s,c)) &= \sqrt{s^*}[1-(1-s^{*1/m_w})^{m_w}]^2, \\ k_{r,n}(m_o(\sigma(c)), s^*(s,c)) &= \sqrt{1-s^*}(1-s^{*1/m_o})^{2m_o}. \end{aligned} \tag{5.15}$$

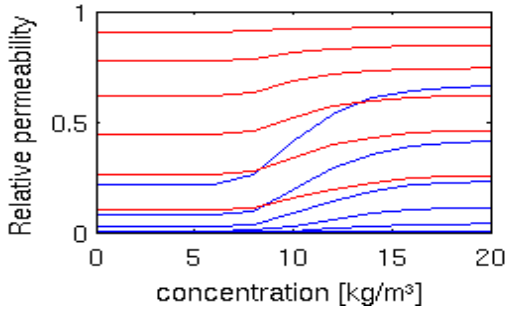

FIGURE 5.6: Relative permeabilities as a function of c from 0-20 kg/m^3. Blue lines are $k_{r,w}$, red are $k_{r,n}$.

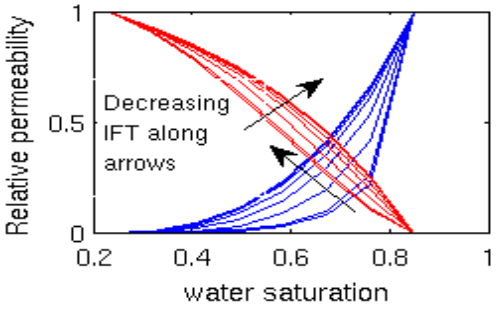

FIGURE 5.7: Relative permeabilities for IFT 0.06-1 mN/m, with residuals s_{res}=0.23, s_{max}=0.85.

5.2.2 Summary of our parameterizations depending on concentration

In this thesis we choose to use the van Genuchten parameter n=2 $\Leftrightarrow$ m=0.5. To summarize our new parameterization we have

$$
\begin{aligned}
&\sigma(c) = (\sigma_0 - \sigma_{min})\,\mathrm{e}^{-\alpha c} + \sigma_{min},\\
&p_c(s^*, c) = \frac{p_{e,0}}{\sigma_0}((\sigma_0 - \sigma_{min})\,\mathrm{e}^{-\alpha c} + \sigma_{min})(s^{*-2} - 1)^{1/2},\\
&s_{max}(c) = 1 - s_{o,res}(c) = 1 - \frac{\sigma}{2.432\sigma + 0.1154},\\
&m_w(c) = 0.5 - 0.17\ln(\sigma(c)), && \forall \sigma < 1 \text{ mN/m},\\
&m_o(c) = 0.5 + 0.09\ln(\sigma(c)), && \forall \sigma < 1 \text{ mN/m},\\
&m_w = m_o = 0.5, && \forall \sigma \geq 1 \text{ mN/m},\\
&k_{r,w}(m_w(c), s^*) = \sqrt{s^*}[1 - (1 - s^{*1/m_w})^{m_w}]^2,\\
&k_{r,n}(m_o(c), s^*) = \sqrt{1 - s^*}(1 - s^{*1/m_o})^{2m_o},
\end{aligned}
\tag{5.16}
$$

with

$$
s^*(s, c) = \frac{s - s_{res}}{s_{max}(c) - s_{res}}, \tag{5.17}
$$

so that we need to determine values for $p_{e,0}$, σ_0, σ_{min} and α.

5.3 The Isolated Effect of Dynamic Capillarity for Different Permeabilities

In this section we will explore the effect of dynamic capillarity for a single point in space (x = 5 m), close to our left boundary. This is chosen because we expect the saturation to change from the initial value quite early and rapidly. We will compare the same point in space for a reservoir with high permeability, k = 500 mD, a reservoir with medium permeability, k = 50 mD and also for a reservoir with low permeability of k = 5 mD, in order to compare the three. In either case the fluid properties are as described in Table 5.1, and the boundary- and initial conditions are

$$
p(0,t) = 35, \quad s(0,t) = s_{max} = 0.59, \quad p(L,t) = 5, \quad \frac{\partial s}{\partial x}(L,t) = 0,
$$
$$
p(x,0) = 5, \quad s(x,0) = 0.01,
$$

with a residual saturation of $s_{res} = 0$ and $s_{max} = 0.59$. The results are shown in Figures 5.8 and 5.9 for the different permeabilities, together with three different functions for τ, one constant equal to zero, one large constant, and one linear relationship

- $\tau(s) = 0$,
- $\tau(s) = 10^7$ Pa $\cdot$ s,
- $\tau(s) = 2 \cdot 10^7(1 - s)$ Pa $\cdot$ s,

for all three examples. Notice that different times are plotted for the different cases, to capture the time-period where the effects are most distinct. The different choices of τ are inspired by [58].

In all cases $\alpha = 0.5$, $\sigma_{min} = 0.06$ mN/m and $\sigma_0 = 40$ mN/m.

The literature on the subject of dynamic capillarity suggests that the effects may be more significant in porous media with low permeability [31, 33, 59], especially in the process of wetting [31].

This is not clear from our findings in Figures 5.8 and 5.9, but an important point is to notice that the dynamic effect play a role for a longer time for the less permeable reservoirs, while at the highly permeable reservoir, the effect is only present in the few hours of wetting of the point. Due to the fact that the wetting process takes place in less time, the effects are more visible in the figures, because of the magnitude of $\partial_t s$, which governs the size of the dynamic effects in our model.

We have been working on strictly homogeneous reservoirs, while [33, 58] suggests that the effects of dynamic capillarity may be even more significant in heterogeneous porous media.

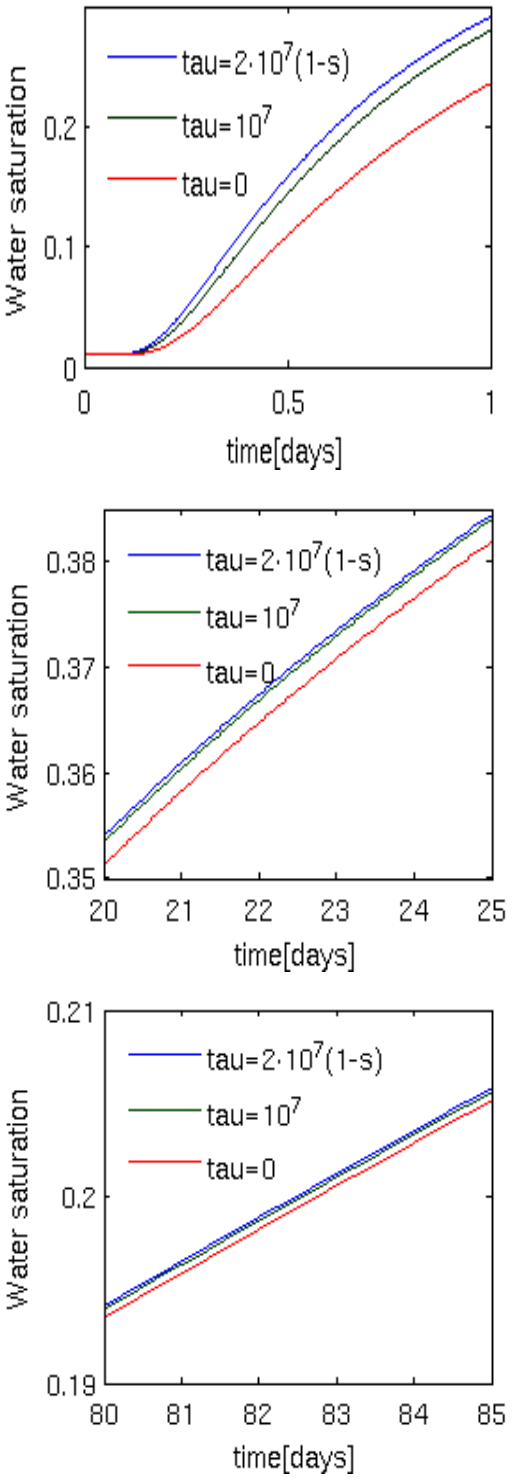

FIGURE 5.8: Saturation profiles at different times at $x = 5$ m, with different functions for τ, for decreasing permeability from $k = 500$ mD $k = 50$ mD and $k = 5$ mD.

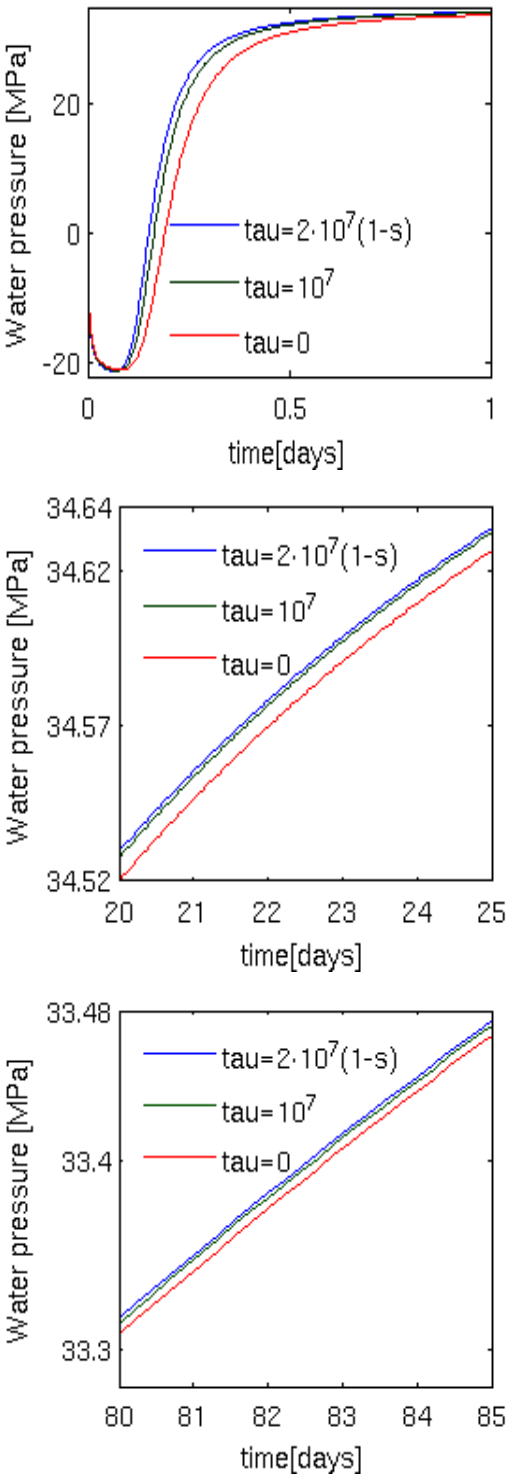

FIGURE 5.9: Pressure profiles at different times at $x = 5$ m, with different functions for τ, for decreasing permeability from $k = 500$ mD $k = 50$ mD and $k = 5$ mD.

5.4 The Dual Effect of Dynamic Capillarity and Bacterial Concentration for Different Permeabilities

In order to couple the concept of MEOR and the concept of dynamic capillarity we use the same settings as in the previous section. In addition, we apply boundary- and initial conditions for the concentration as

$$c(0,t) = 6, \qquad \frac{\partial c}{\partial x}(L,t) = 0, \qquad c(x,0) = 0, \tag{5.18}$$

in order to model an injection of bacteria through the left boundary. Once again we run the simulations for low, medium and high permeability, and compare them in Figures 5.10 and 5.11. One can observe that when we couple the effects, the difference between the functions for τ becomes more distinct due to the increase of s_{max}, explained by the added concentration, and therefore larger possible changes in the saturation. Also note that the wetting in the first case happens at a later time for the same reason, the waterflood fills the first part of the reservoir, which now can hold more water than in the previous case.

The changes are once again almost negligible for the low permeability, and the explanation for this is once again that the wetting is more gradual, which explains why the dynamic effects are smaller. Aside from that, one can clearly observe that the wetting happens at an earlier time than in the case where there are no microbes present. The microbes thus cause a relatively big effect, leading to more porespace for the water to invade than in the first case. Such consequences will be further investigated in Sections 5.5.1 to 5.5.3.

In [59], the authors suggests that the dynamic coefficient that governs the dynamic effects could be higher in low permeability reservoirs than in those with higher permeability, and in a new study by Zhang et al. [60], the reported coefficients are in the range of $10^{10} - 10^{13}$ Pa $\cdot$ s for ultra-low permeability below 1 mD.

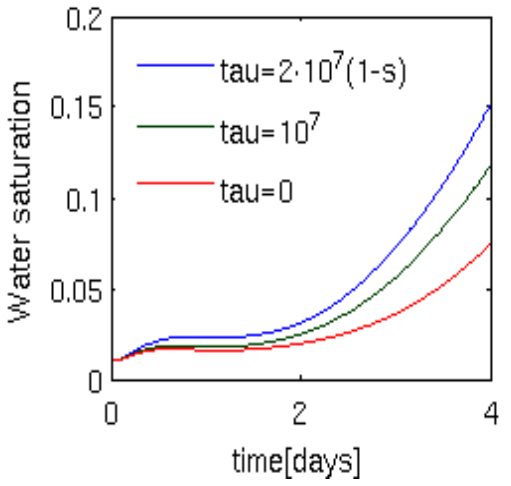

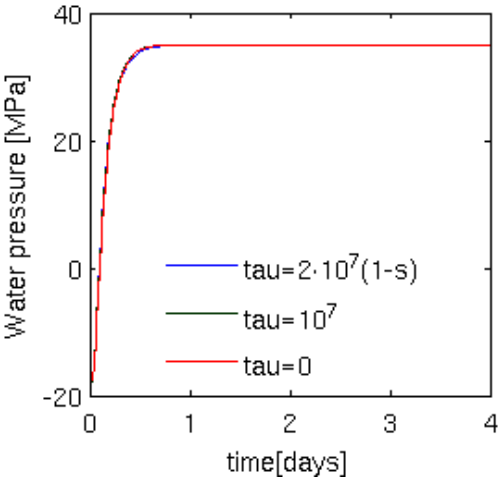

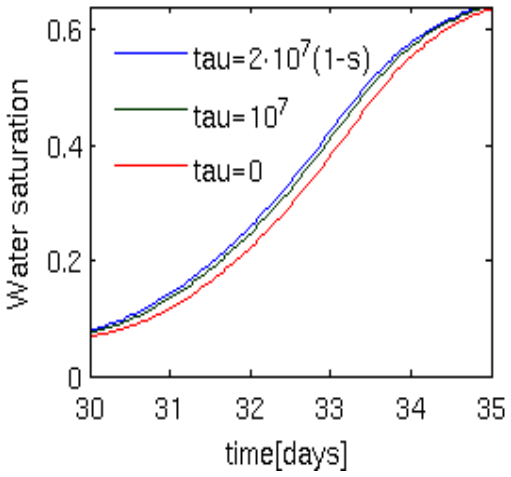

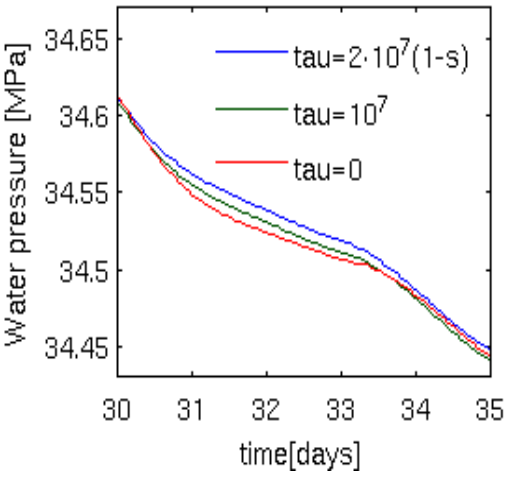

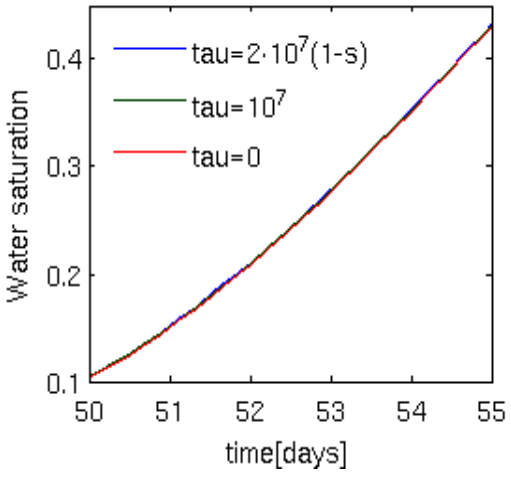

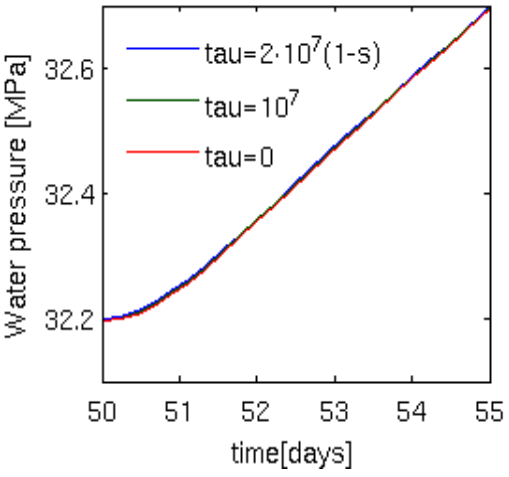

FIGURE 5.10: Saturation profiles at different times at $x = 5$ m, with different functions for τ, for decreasing permeability from $k = 500$ mD $k = 50$ mD and $k = 5$ mD, included MEOR.

FIGURE 5.11: Pressure profiles at different times at $x = 5$ m, with different functions for τ, for decreasing permeability from $k = 500$ mD $k = 50$ mD and $k = 5$ mD, included MEOR.

5.5 MEOR and Dynamic Capillarity for Different Examples

In this section we will model different reservoirs with different approaches for second or third phase recovery strategies. Results are compared for different injection volumes of microbes, with or without dynamic capillary pressure includement.

In all cases we waterflood the reservoir from the left boundary, with boundary conditions in the reservoir as

$$p(0,t) = 35, \quad s(0,t) = s_{max}, \quad p(L,t) = 5, \quad \frac{\partial s}{\partial x}(L,t) = 0, \tag{5.19}$$

where the Dirichlet boundary for saturation on the left boundary is updated to the actual value of s_{max} at all times. We inject different amount of bacteria in the flood, described in the Dirichlet boundary conditions for the left boundary

- $c(0,t) = 0$,
- $c(0,t) = 6$,
- $c(0,t) = 12$,

with a Neumann BC for the concentration at the right boundary in all cases,

$$\frac{\partial c}{\partial x}(L,t) = 0. \tag{5.20}$$

In the following we will present three examples, where the first example considers our reference reservoir as introduced in Section 5.1, the second is a significantly shorter reservoir setup and the third can be seen as an extreme case, where we apply unrealistic parameters to force significant dynamic effects.

5.5.1 Example reference reservoir

The simulations are first performed without the inclusion of dynamic capillarity, letting τ=0. The initial conditions are

$$p(x,0) = 5, \qquad s(x,0) = 0.3.$$

Results for production rate and total production, saturation, average pressure and concentration are graphically presented at a time of 250 days, 500 days and at the end time of 750 days.

The simulations are then reproduced with the inclusion of dynamic capillarity, letting $\tau = 10^7$ Pa $\cdot$ s. Once again the results for production rate, total production, saturation, average pressure and concentration are presented at the same times.

Note that we have kept the same size of both the grid size and time step in the two simulations to ensure similarity in the computations.

The plots of interest are presented in Figures 5.12 to 5.19, where the plots included dynamic capillary pressure are on the right hand side in all figures.

When comparing the results with and without dynamic capillarity, we discover that they are close to identical for all variables, meaning that the dynamic capillary pressure exhibits no visible difference on the macroscale in this example. As a possible explanation to this we observe that the wetting is rather slow, as it takes 750 days to come close to equilibrium in the case of most concentration, and 500 days for the other two cases.

For different injected quantity of microbes we observe interesting behavior. We note that in the case of $c(0,t) = 6$ the results are only slightly better than for the pure water-wetting, in terms of overall production the difference is 2,6 %. On the other hand, observe that, when $c(0,t) = 12$, the wetting happens with what can be described as a dual front. The initial front is slightly less progressed compared to the other two in terms of time, and significantly smaller in size, explaining the fact that the production rate is lower during the first 250 days. The second front is due to the alteration of the residual oil content, because of a significant reduction in the interfacial tension. It flushes the reservoir at a later time, resulting in a substantial production of oil for a longer period of time.

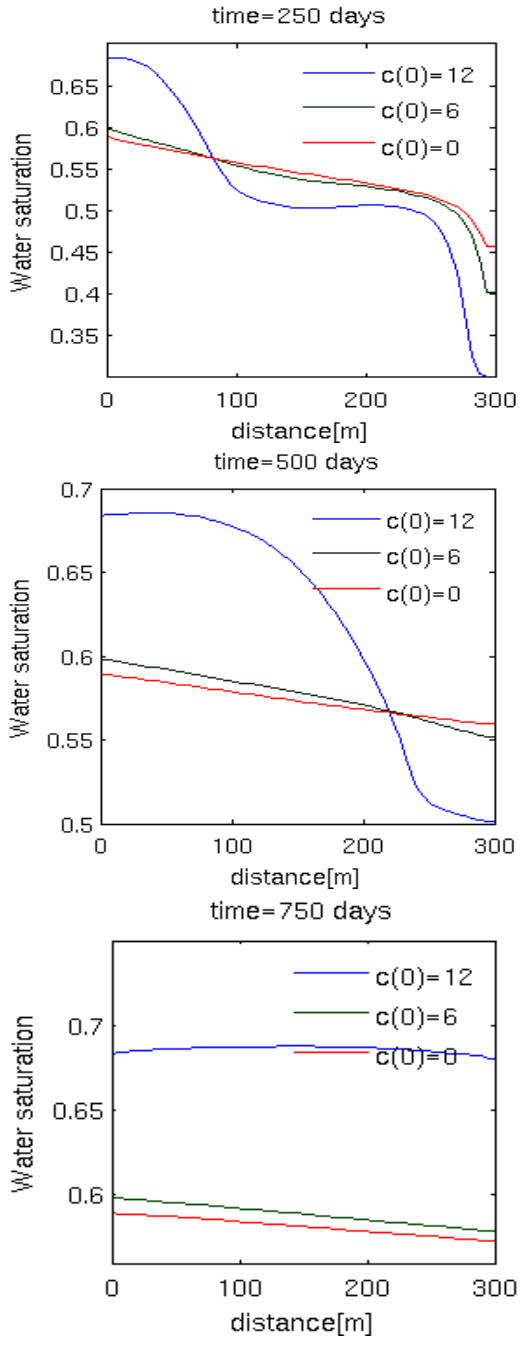

FIGURE 5.12: Saturation profiles at different times, for different injected concentration of bacteria, no dynamic capillarity.

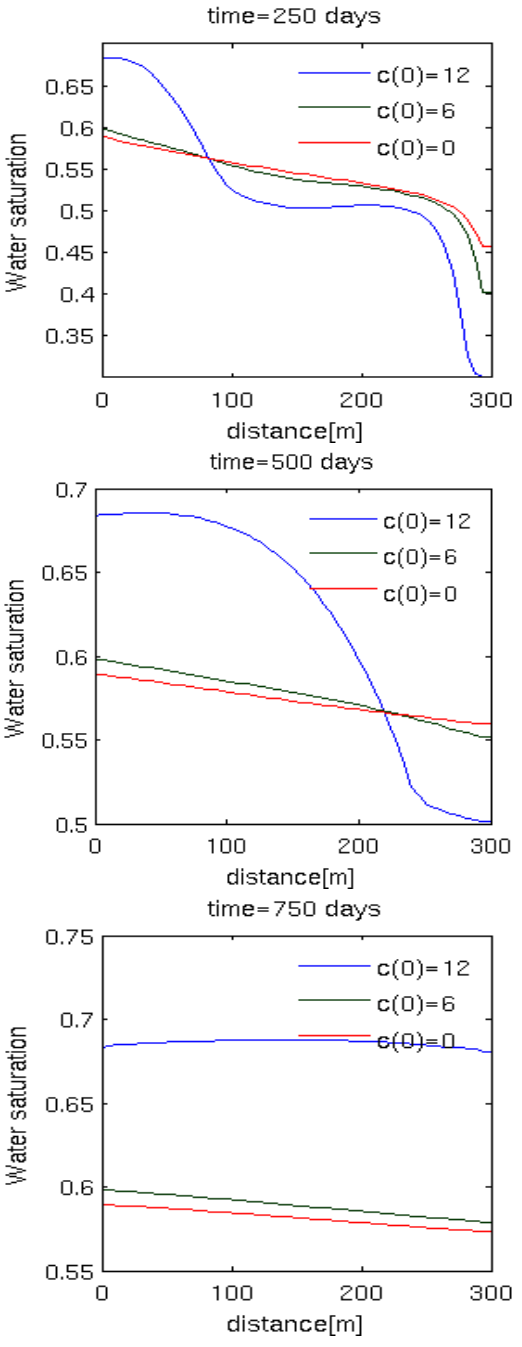

FIGURE 5.13: Saturation profiles at different times, for different injected concentration of bacteria, with $\tau = 10^7$ Pa $\cdot$ s.

In terms of total production we observe that when the injected concentration is $c(0,t) = 12$ the result after 750 days are approximately 35 % better than for the other two. The distinct peaks of the production rate stems from the water breakthrough, where we again observe two peaks due to the dual front in the case of high concentration.

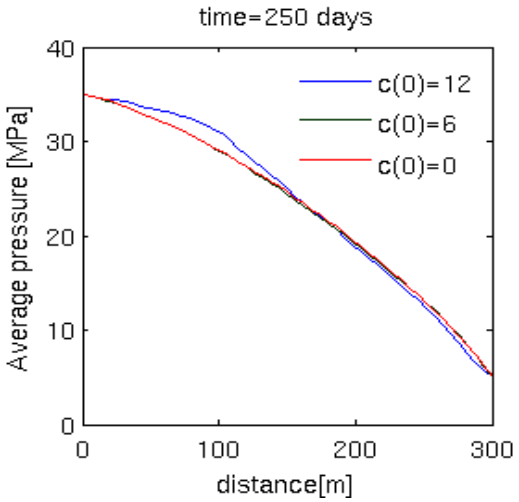

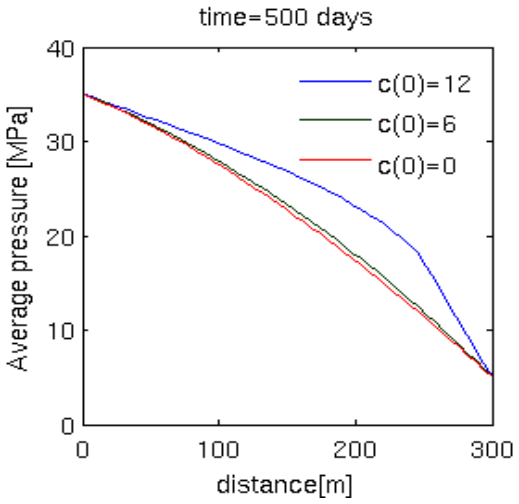

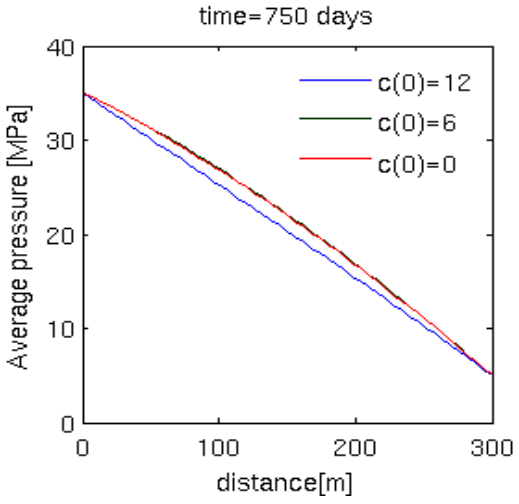

FIGURE 5.14: Pressure profiles, for different concentration of bacteria, no dynamic capillarity.

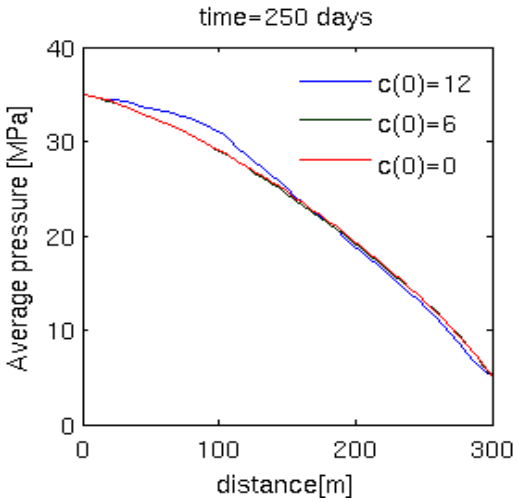

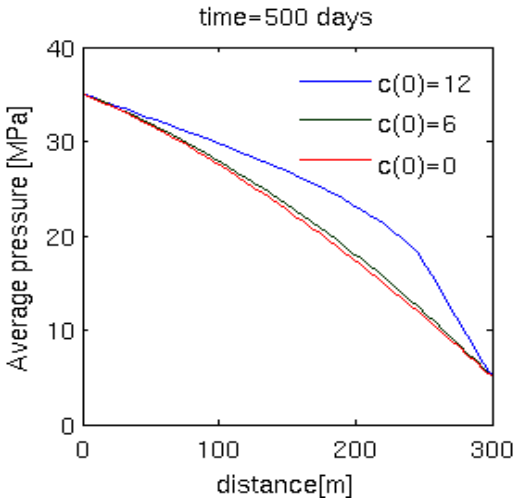

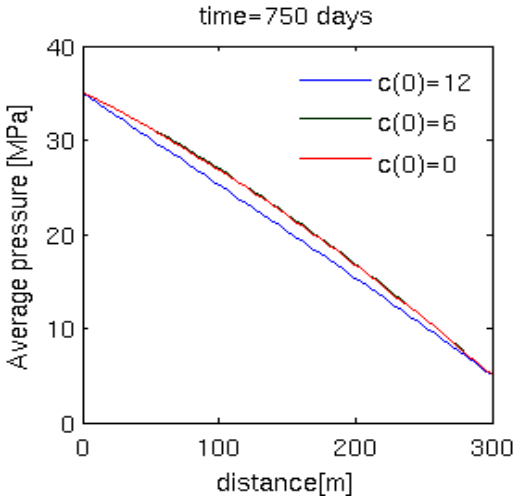

FIGURE 5.15: Pressure profiles, for different concentration of bacteria, $\tau = 10^7$ Pa $\cdot$ s.

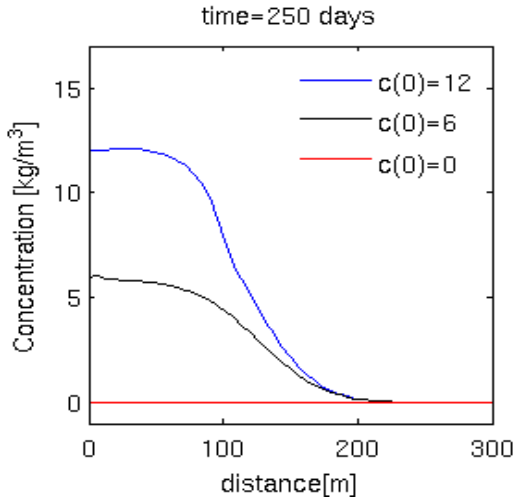

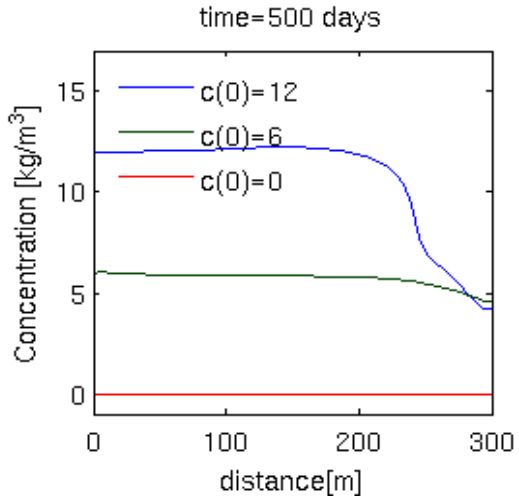

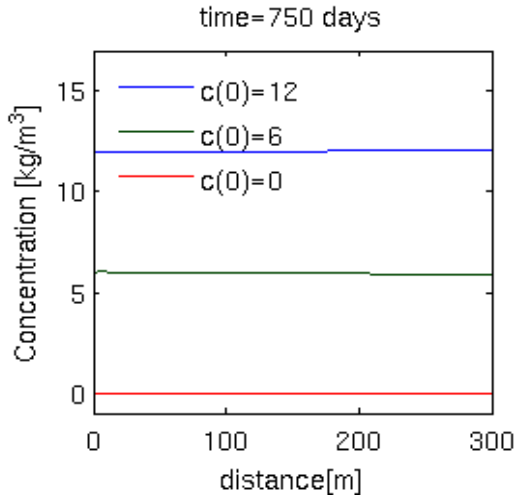

FIGURE 5.16: Concentration profiles at different times, for different injected concentration of bacteria, no dynamic capillarity.

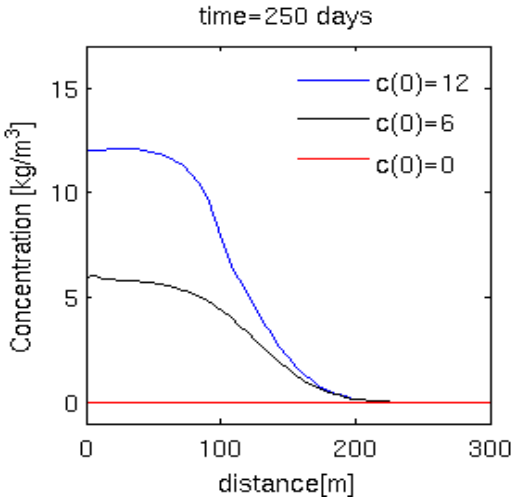

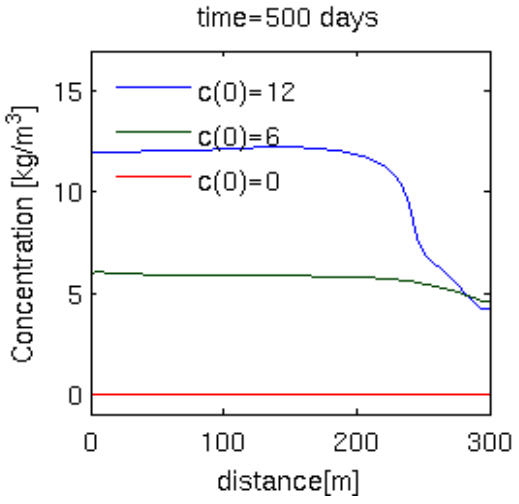

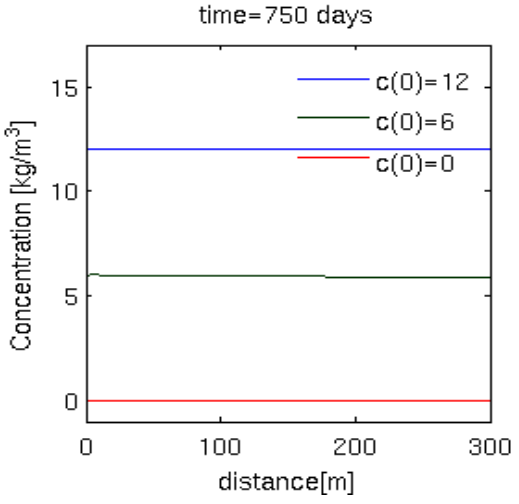

FIGURE 5.17: Concentration profiles at different times, for different injected concentration of bacteria, $\tau = 10^7$ Pa · s.

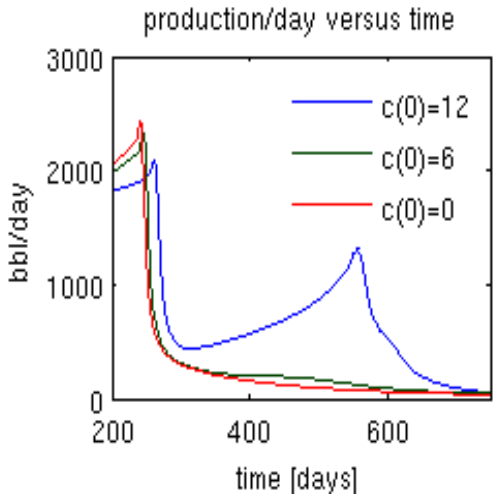

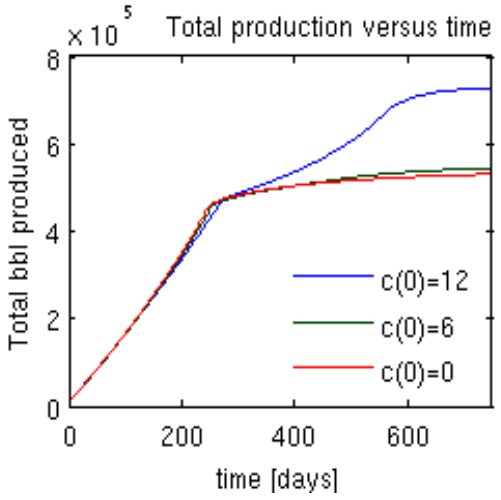

FIGURE 5.18: Production rate and total production as a function of time, for different injected concentration of bacteria, $\tau = 0$.

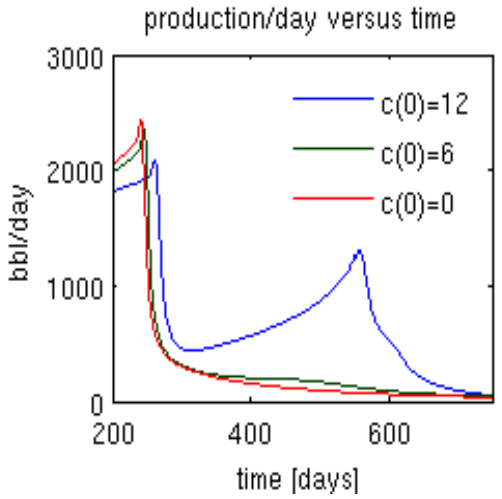

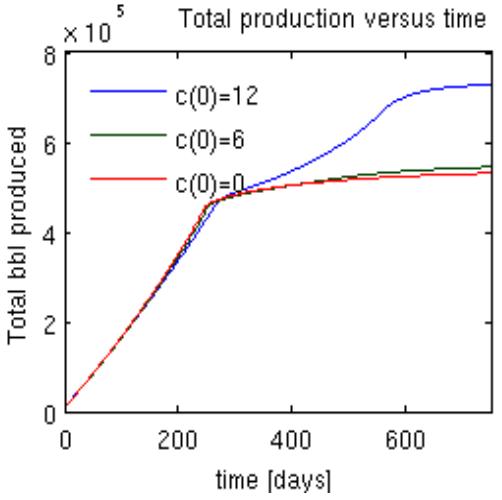

FIGURE 5.19: Production rate and total production as a function of time, for different injected concentration of bacteria, $\tau = 10^7$ Pa $\cdot$ s.

5.5.2 Example reservoir II

In order to produce results that might show an effect of the dynamic capillary pressure, we create a domain, and introduce physical properties, that allow for a higher rate of change in the saturation. This rate of change rules the size of the contribution due to dynamic capillarity. The domain and properties for the reservoir are presented in Table 5.2.

We apply the same boundary conditions as in the previous example, but introduce a lower initial saturation

$$p(0,t) = 35, \quad s(0,t) = s_{max}, \quad p(L,t) = 5, \quad \frac{\partial s}{\partial x}(L,t) = 0,$$
$$p(x,0) = 5, \quad s(x,0) = 0.1.$$

As the reservoir is one third the length of the previous one, the pressure gradient inside is significantly larger, and the residual saturation is equal to zero.

The injection of microbes are done in the same fashion, and the results are presented as before, at times 10 days, 20 days, and an end time of 30 days, in Figures 5.20 to 5.27. Dynamic capillary pressure is included in the same way, with $\tau = 0$ corresponding to the plots on the left hand side, and $\tau = 10^7$ Pa $\cdot$ s the right hand side.

We observe that in the case of $c(0,t)$=12, the total production is again higher than for the other situations, with a 26 % higher production after 30 days, while the dynamic capillary pressure neither here seems to cause much effect.

Property	Value	Property	Value
ϕ	0.4	D	6 m^2/day
k	200 mD	σ_0	4 mN/m
μ_o	$3 \cdot 10^{-3}$ Pa $\cdot$ s	σ_{min}	0.06 mN/m
μ_w	$1 \cdot 10^{-3}$ Pa $\cdot$ s	α	0.5
ρ_w	1020 kg/m^3	s_{max}	0.59
ρ_o	770 kg/m^3	s_{res}	0
p_{entry}	1 MPa	$p(0,x)$	5 MPa
A	1000 m^2	L	100 m
$s(0,x)$	0.1	n	2

TABLE 5.2: Properties reservoir II

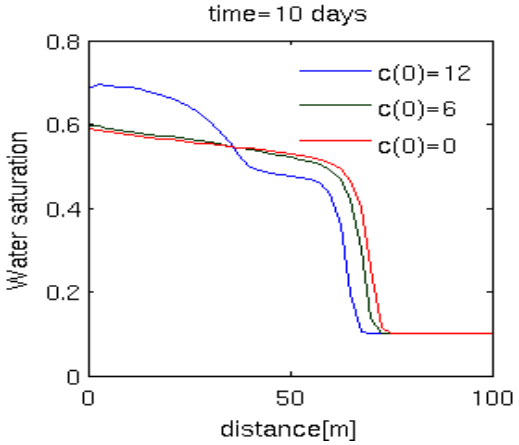

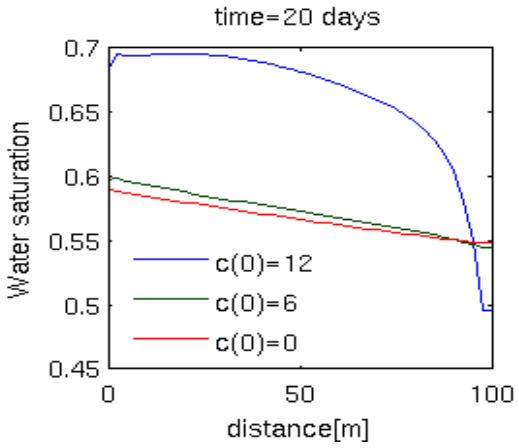

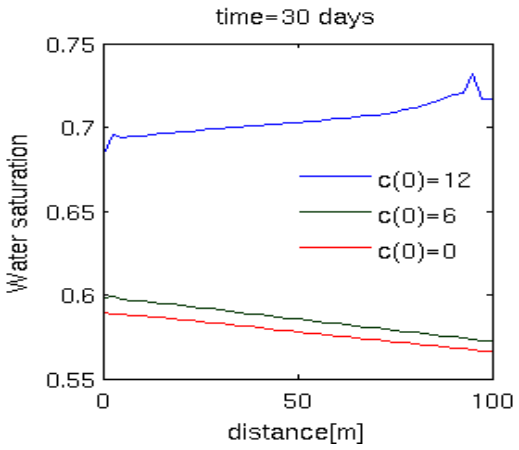

FIGURE 5.20: Saturation profiles at different times, for different injected concentration of bacteria, no dynamic capillarity.

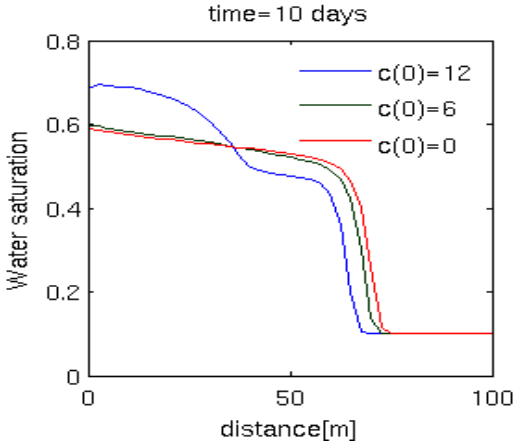

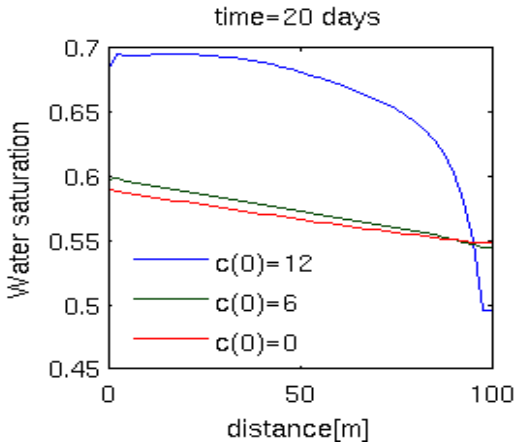

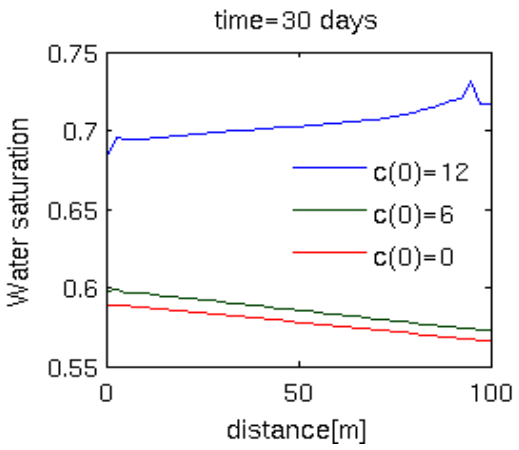

FIGURE 5.21: Saturation profiles at different times, for different injected concentration of bacteria, $\tau = 10^7$ Pa · s.

Again the peaks show the water breakthrough, and the dual front is noticeable in the case of high microbial concentration.

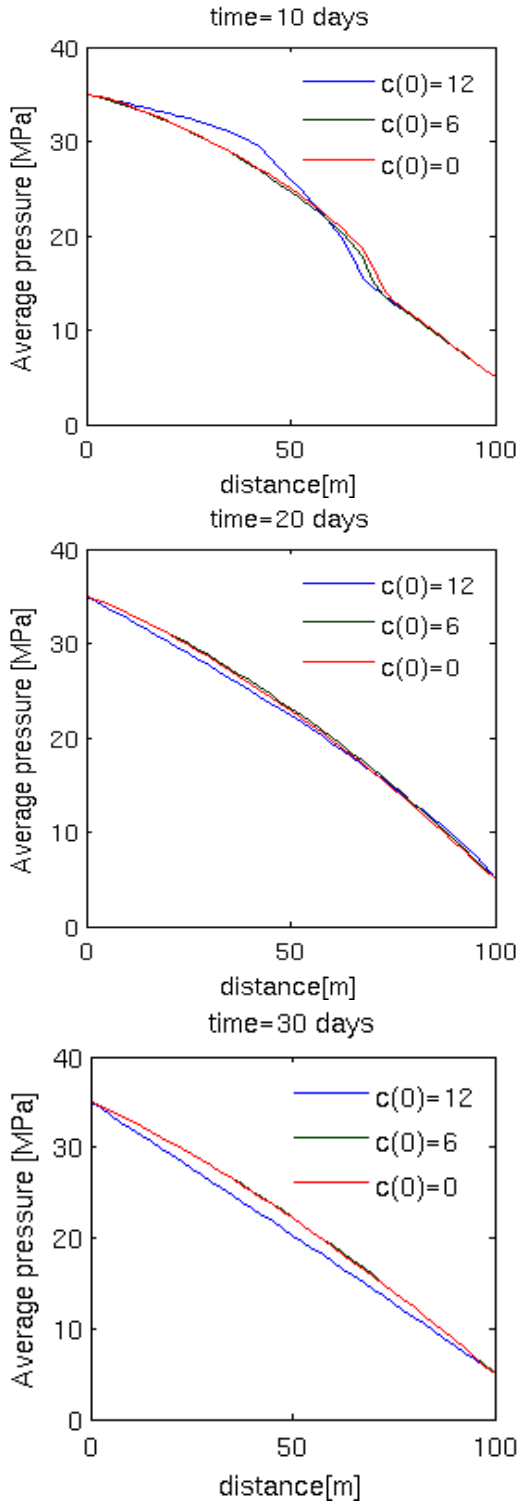

FIGURE 5.22: Pressure profiles, for different concentration of bacteria, no dynamic capillarity.

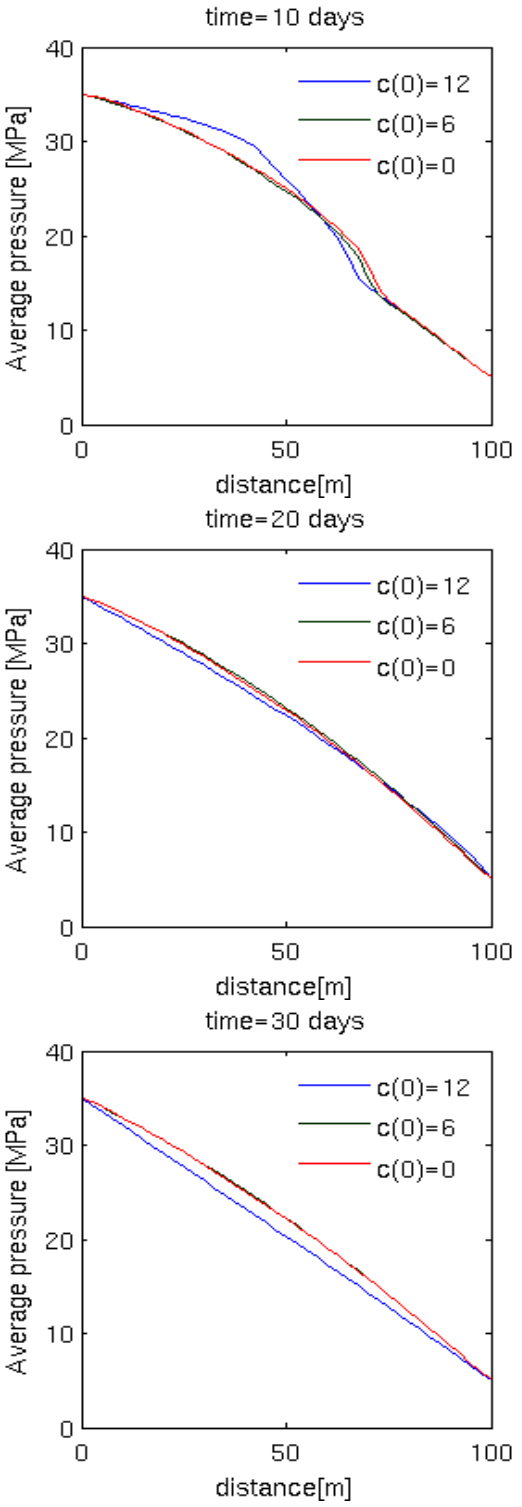

FIGURE 5.23: Pressure profiles, for different concentration of bacteria, $\tau = 10^7$ Pa $\cdot$ s.

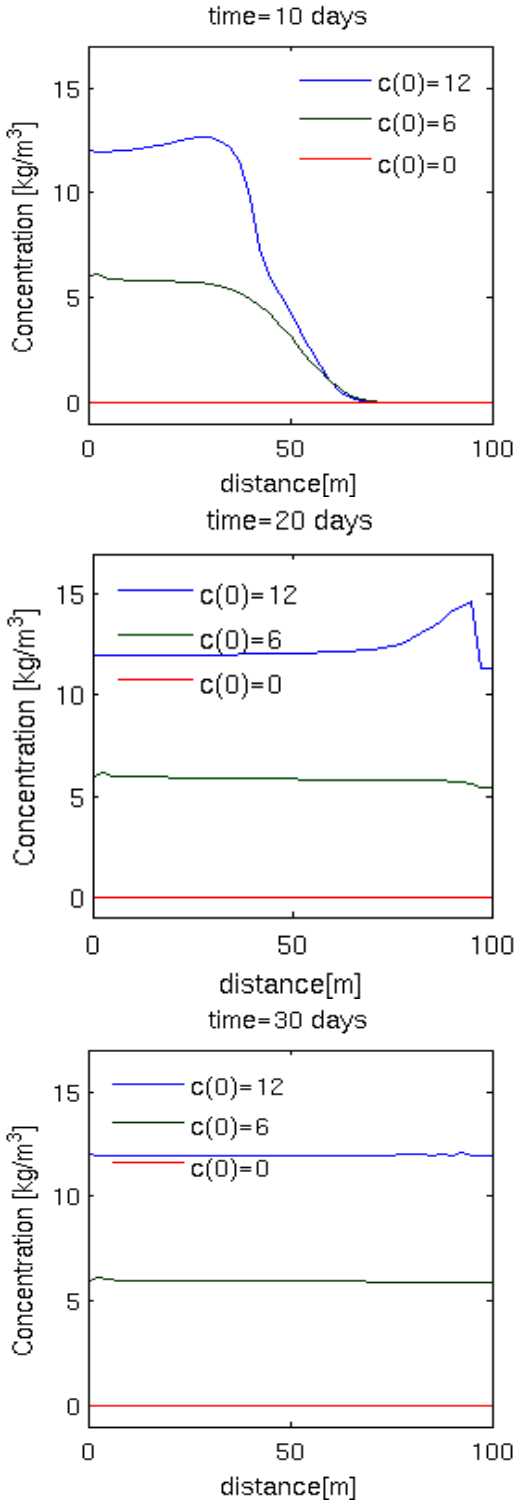

FIGURE 5.24: Concentration profiles at different times, for different injected concentration of bacteria, no dynamic capillarity.

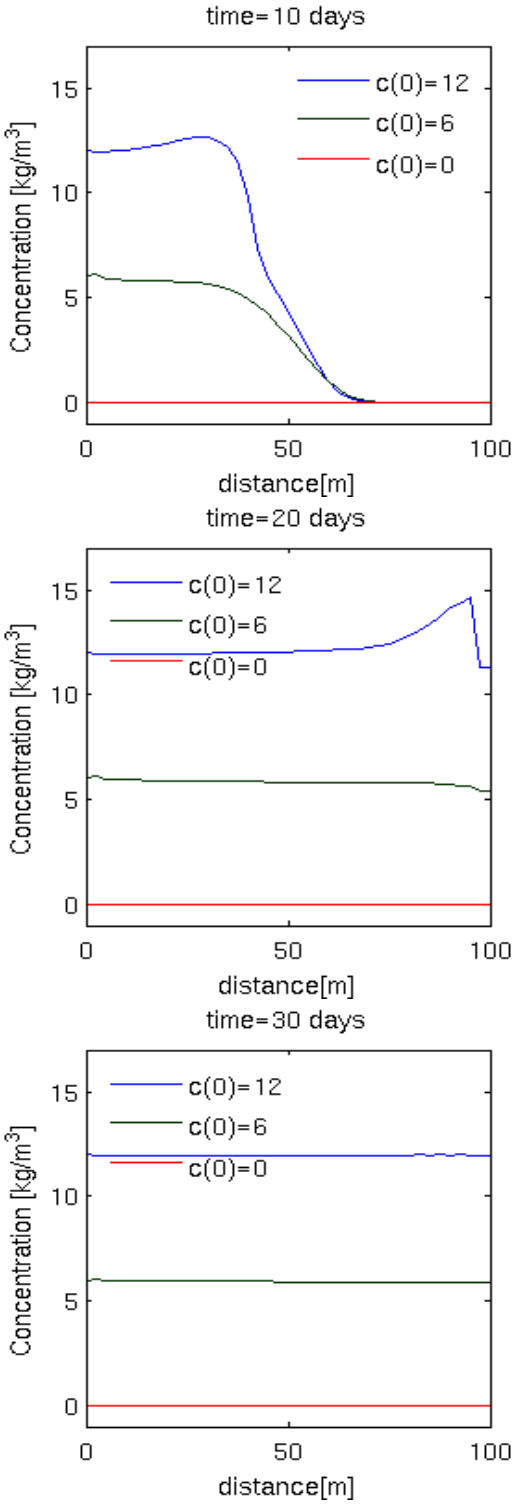

FIGURE 5.25: Concentration profiles at different times, for different injected concentration of bacteria, $\tau = 10^7$ Pa · s.

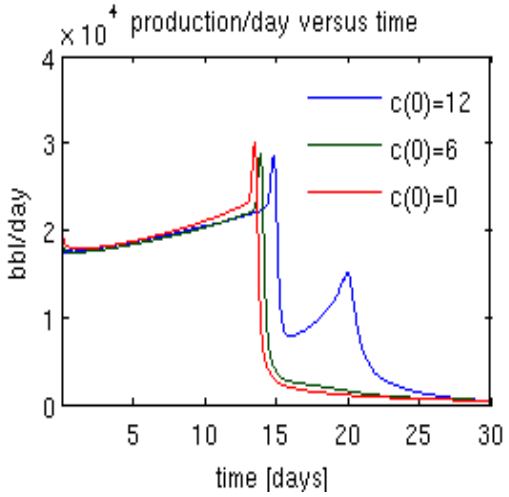

FIGURE 5.26: Production rate and total production as a function of time, for different injected concentration of bacteria, $\tau = 0$.

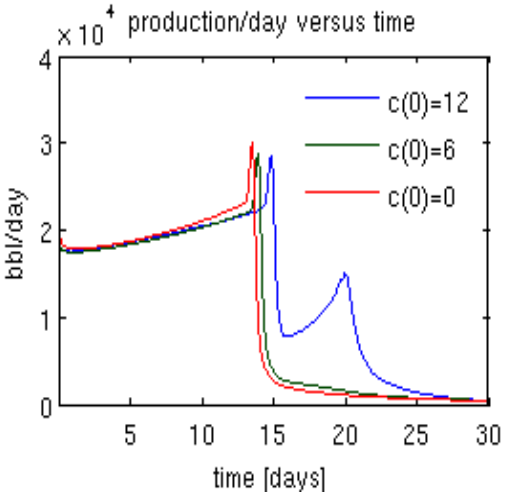

FIGURE 5.27: Production rate and total production as a function of time, for different injected concentration of bacteria, $\tau = 10^7$ Pa · s.

5.5.3 Example reservoir III

Again, we modify properties to model effects of dynamic capillary pressure. This is done by shortening the reservoir to a length of $L = 70$ m, introducing a dispersion-diffusion coefficient of $D = 9$ m^2/day for smoothing, together with a non-realistic value for the dynamic capillary coefficient, $\tau = 10^{10}$ Pa $\cdot$ s. The other properties are as described in Table 5.2.

We apply the same boundary- and initial conditions as in the previous example,

$$p(0,t) = 35, \quad s(0,t) = s_{max}, \quad p(L,t) = 5, \quad \frac{\partial s}{\partial x}(L,t) = 0,$$
$$p(x,0) = 5, \quad s(x,0) = 0.1.$$

Again we emphasize that this means that the pressure gradient is larger, due to the reduced length, L. The results are here presented at times of 4, 8 and 12 days, using the same system, with dynamic capillary pressure included on the plots on the right hand side, in Figures 5.28 to 5.35.

Here we are able to see a significant difference between the results with and without the inclusion of dynamic capillarity. What we observe is that after 4 days, the effects on saturation are clearly visible for all concentrations, where the front is more progressed in the case of dynamic capillarity. Also, notice that the second front in the case of high concentration is significantly more spread out in the case of dynamic capillary pressure inclusion. All these effects are explained by the fact that the dynamic capillarity drives the flow, together with the pressure gradient, from left to right. As the reservoir approaches equilibrium, the effects are not as visible, as seen in the case of medium and no concentration after 8 and 12 days.

The same applies for the concentration of microbes in this case, where the second driving force, the dynamic capillarity, makes the bacteria spread out faster with the flow, especially visible after 4 and 8 days, for both large and medium concentration.

The average pressure is increased in most of the reservoir after 4 days when dynamic capillary pressure plays a role, while the increase is not as significant without the dynamic capillarity. After 8 days we see a distinct difference between the pressures in the case of

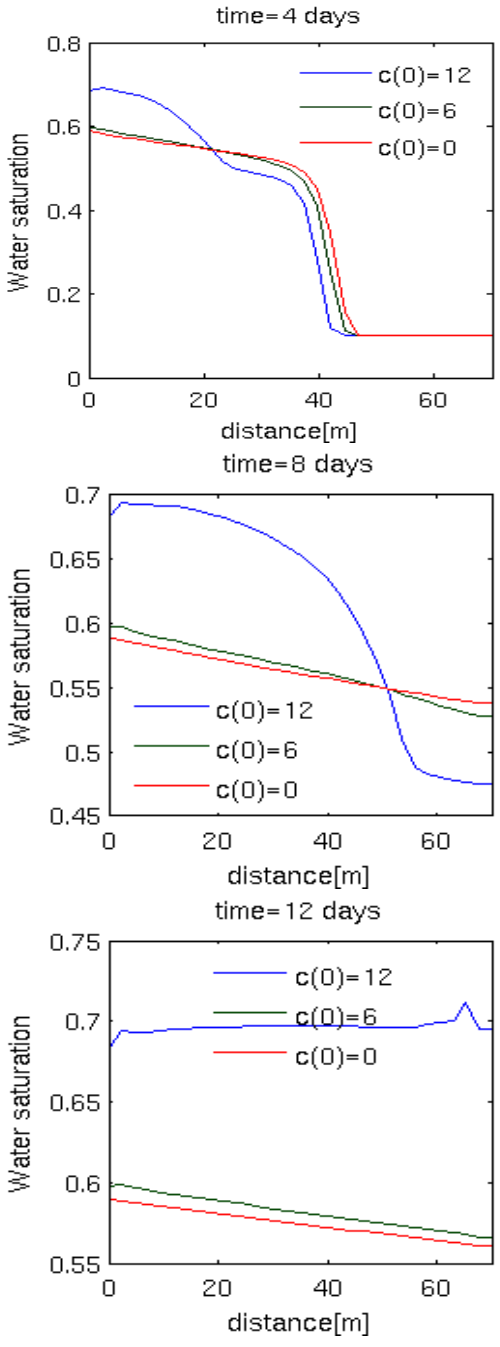

FIGURE 5.28: Saturation profiles at different times, for different injected concentration of bacteria, no dynamic capillarity.

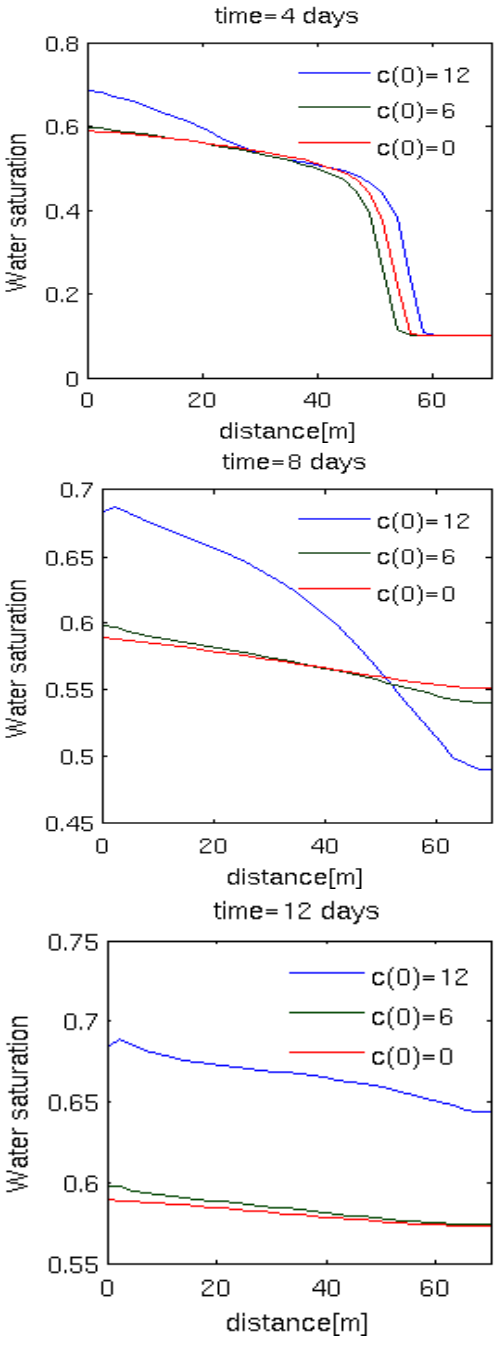

FIGURE 5.29: Saturation profiles at different times, for different injected concentration of bacteria, $\tau = 10^{10}$ Pa · s.

high concentration and no dynamic capillarity due to the massive waterfront which has built up.

Again we note that to produce a substantial amount of oil for a longer period of time, we have to add a significant amount of microbes in the flood, where the total production

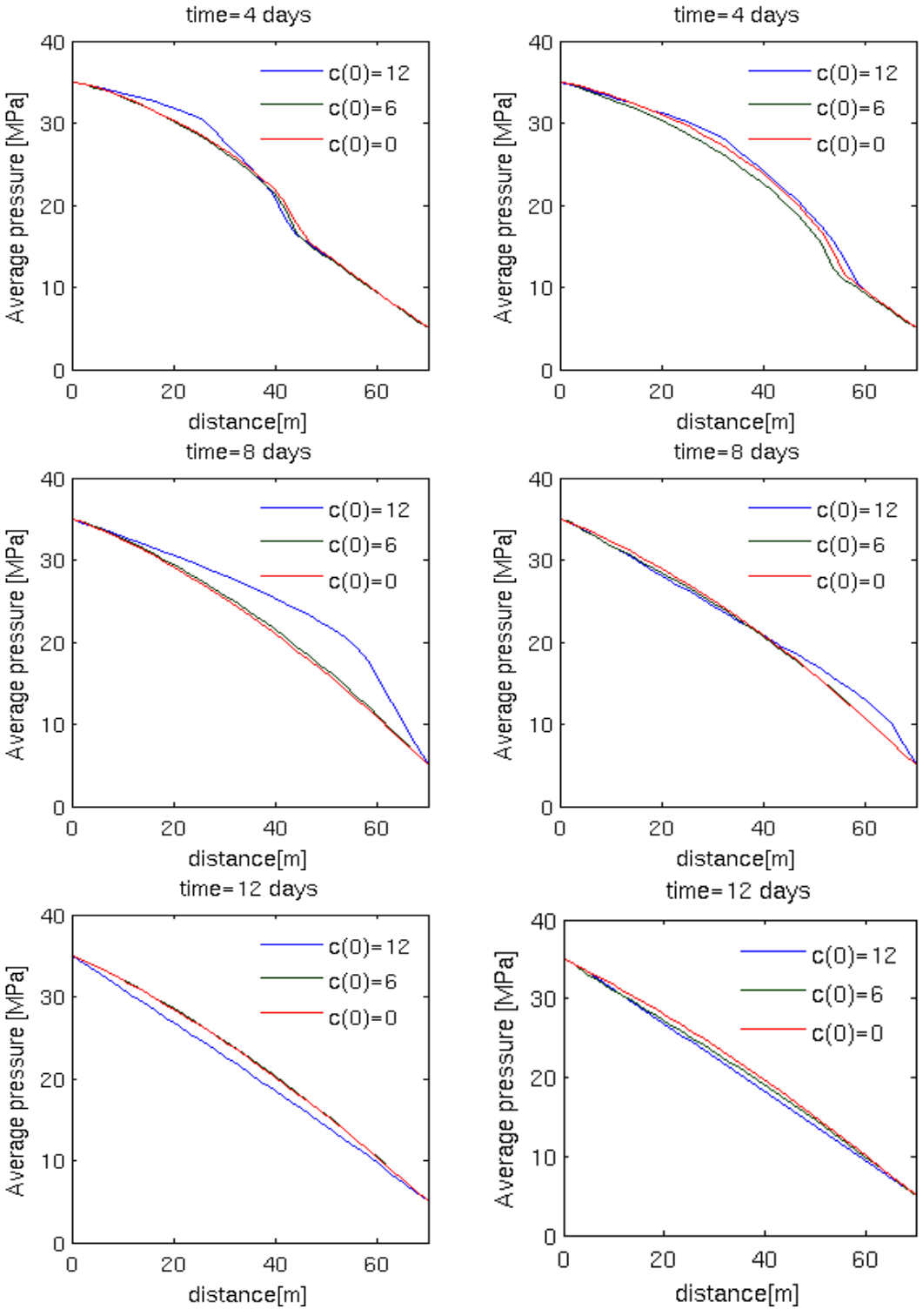

FIGURE 5.30: Pressure profiles at different times, for different injected concentration of bacteria, $\tau = 0$.

FIGURE 5.31: Pressure profiles at different times, for different injected concentration of bacteria, $\tau = 10^{10}$ Pa $\cdot$ s.

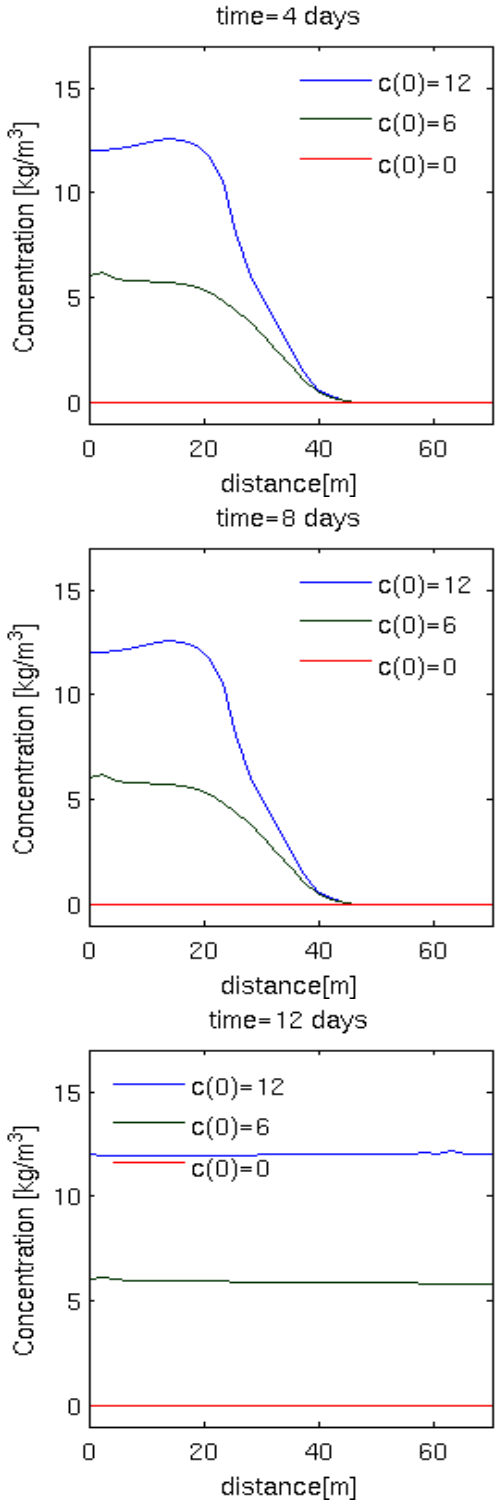

FIGURE 5.32: Concentration profiles at different times, for different injected concentration of bacteria, no dynamic capillarity.

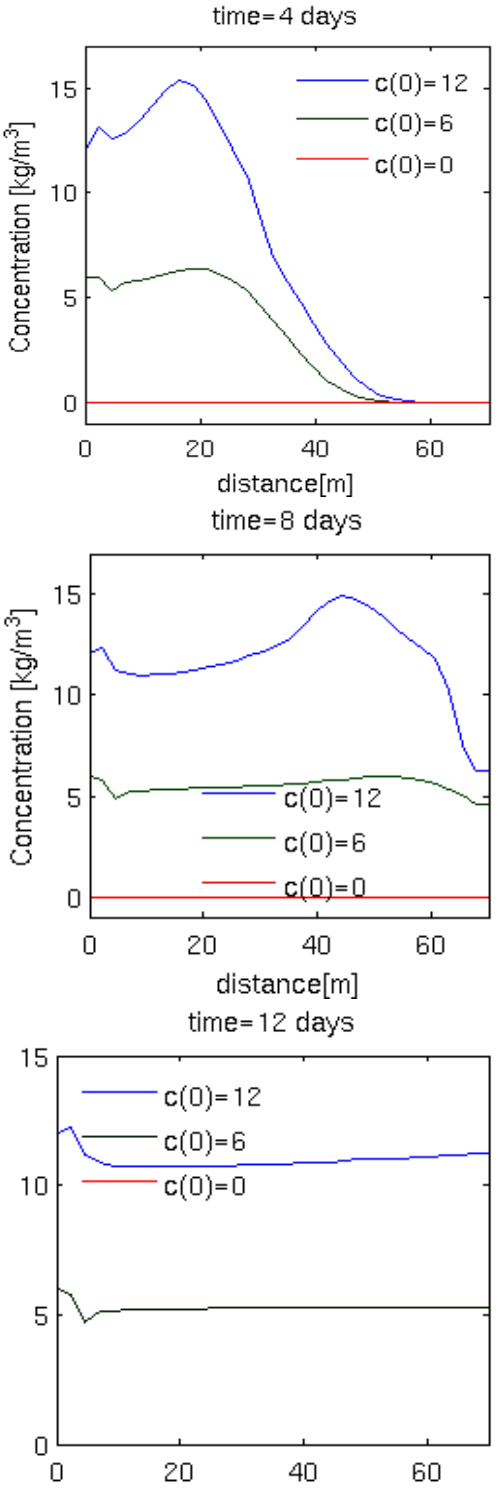

FIGURE 5.33: Concentration profiles at different times, for different injected concentration of bacteria,$\tau = 10^{10}$ Pa $\cdot$ s.

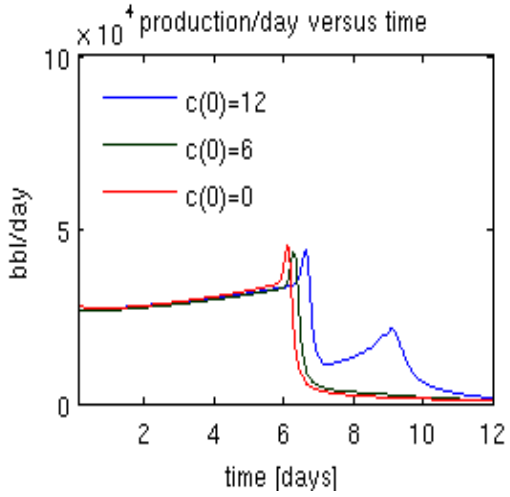

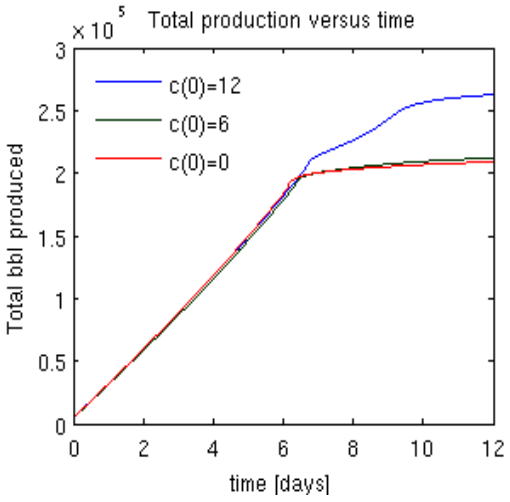

FIGURE 5.34: Production rate and total production, for different injected concentration of bacteria, no dynamic capillarity.

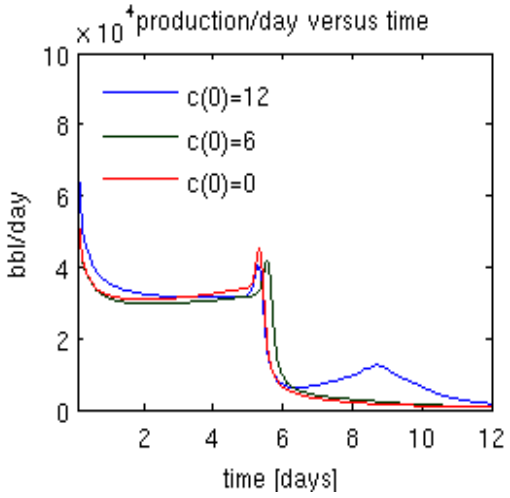

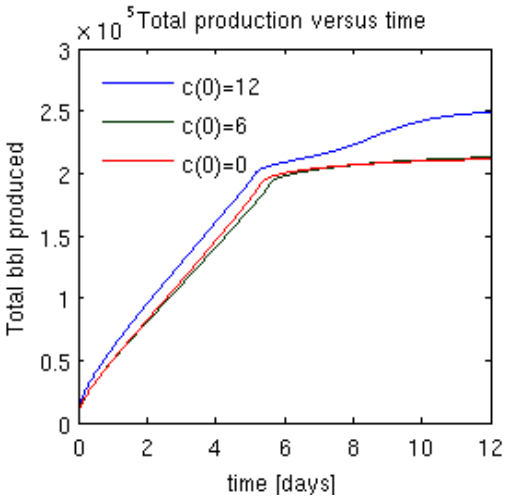

FIGURE 5.35: Production rate and total production, for different injected concentration of bacteria, $\tau = 10^{10}$ Pa · s.

after 12 days is nearly the same in the case of no and medium concentration. Further, the total production is approximately 17,5 %/24,5 % higher with/without dynamic capillarity for the case of $c(0,t)$=12. Note that the oil production is significantly higher at an earlier stage in the case with dynamic capillary pressure, especially in the case of high production, where the first front progresses noticeably faster.

The second front in the case of high concentration is not as defined in the case included dynamic capillarity, which explains that neither the production rate peak is as distinct.

5.5.4 Magnitude of $\frac{\partial s}{\partial t}$ - the driving force for dynamic capillary pressure

In order to understand why the dynamic capillary pressure is hard to spot in the first two examples, whilst it is clearly present and influencing the results in the third example, we explore the term that governs the size of the dynamic pressure. Together with the obvious reason that the value for the coefficient is 3 orders of magnitude larger in the last example, the rate of change is also larger, due to the extreme setup in example III.

All comparisons are done with the highest injected concentration, $c(0,t) = 12$, and the derivative is plotted at times $\{T/6, T/3, T/2, 2T/3, 5T/6, T\}$ in all cases, where T is the endtime.

In the comparison, found in Figure 5.36, we find what we suspected; a very small value for the derivative of saturation throughout for the example on our reference reservoir, explaining the very small effects of dynamic capillary pressure. Again, for example II the rate of change, together with the dynamic coefficient, is too small to see effects on the macroscale. Further, in the extreme case, example III, due to both the maximum rate of change and the dynamic coefficient being of together $4-5$ orders of magnitude larger than in the previous two, the effect is clearly visible.

In all three figures, it is easy to spot the first and second wetting front, where the first front yields the largest values for the rate of change in all three cases. After the fronts have flushed the reservoir the rate of change is, as expected, significantly lower.

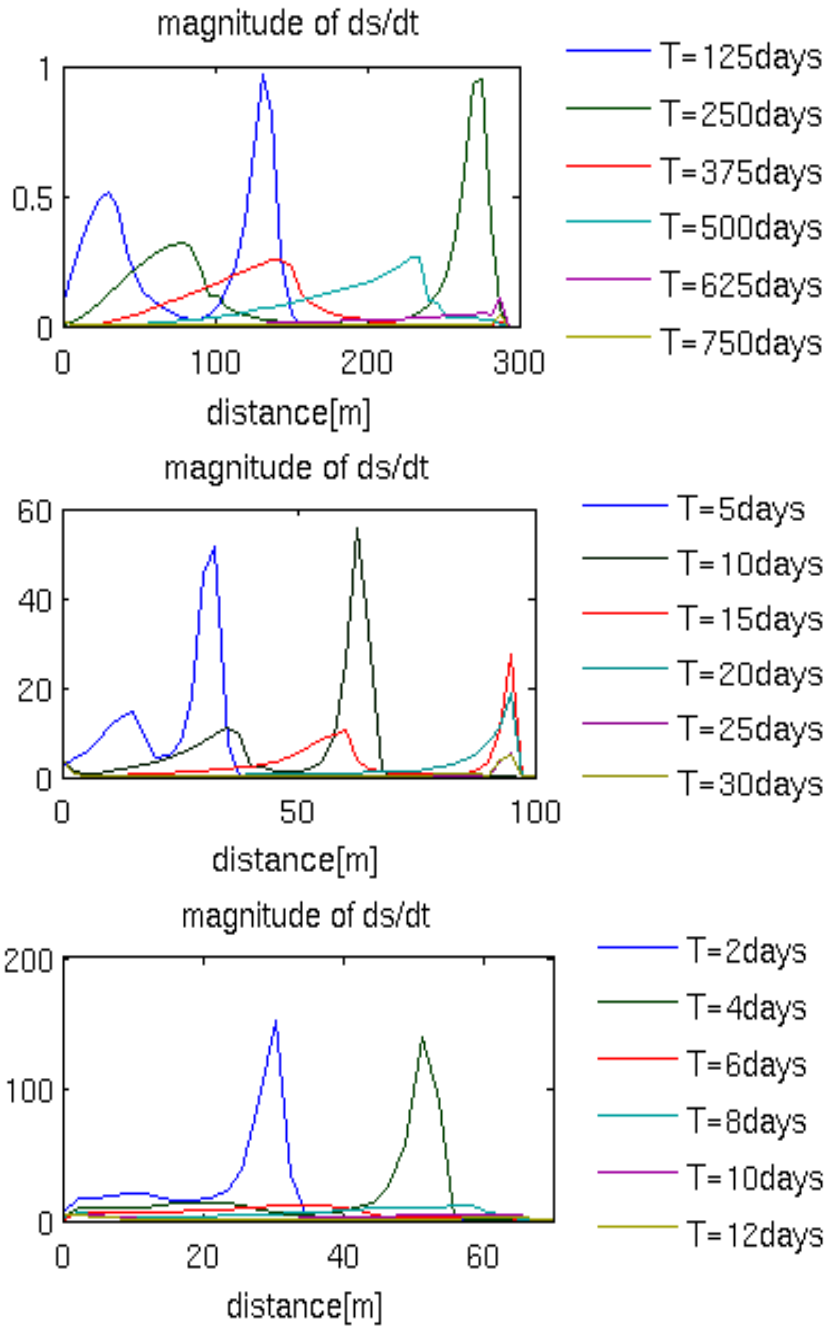

FIGURE 5.36: The magnitude of $\frac{\partial s}{\partial t}$ for example reference reservoir (top),with $\tau = 10^7$ Pa $\cdot$ s, example II (middle), with $\tau = 10^7$ Pa $\cdot$ s and example III (bottom) with $\tau = 10^{10}$ Pa $\cdot$ s and high concentration, $c(0,t)$ =12 for all three.

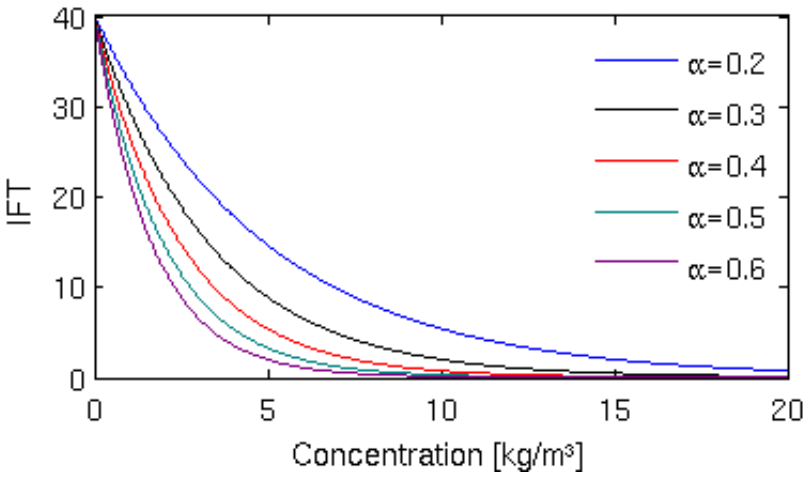

FIGURE 5.37: Interfacial tension as a function of c for different effect coefficients α.

5.5.5 Sensitivity of the effect coefficient α

Here we explore the sensitivity to the parameter describing the effect microbes have on interfacial tension. This is done by variation of the effect coefficient α in Equation (5.7), which governs the relations for relative permeabilities, as well as static capillary pressure, based on microbial concentration. We do so by again modelling waterflooding in our reference reservoir, with a substantial injection of microbes from the left boundary of $c(0,t) = 15$. All other parameters and conditions are as described in Section 5.5.1.

There is no dynamic capillary pressure included in the model, and α is varied from 0.2 to 0.6 in the calculations, with increments of 0.1. Results are shown after 250, 500 and 750 days as before, Figures 5.38 to 5.40. As the effects on average pressure are small, the pressure plots are omitted.

Obvious differences are portrayed on the equilibrium saturation, saturation and production for different values of the effect coefficient, with a 59 % higher production in the case of high effect, α=0.6, versus low effect, α=0.2. The different progression of the fronts shows that the relative permeabilities and static capillary pressure play a significant role in the flow.

This effect coefficient should be experimentally explored, and must describe the IFT-reducing effects that the microbes have on the oil/water surface, as the results in the end are obviously highly sensitive to the size of such effects.

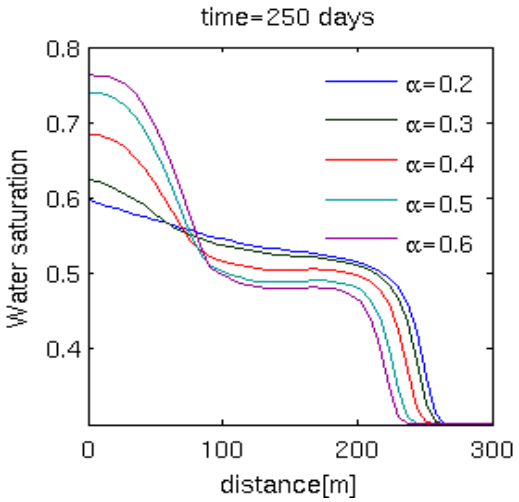

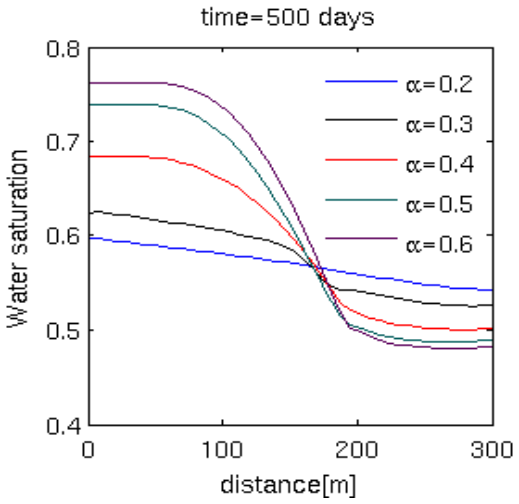

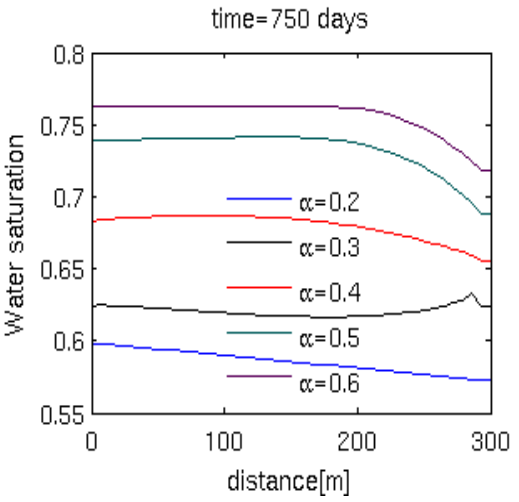

FIGURE 5.38: Saturation profiles at reference reservoir, for different effect coefficients α, $c(0,t) = 15$.

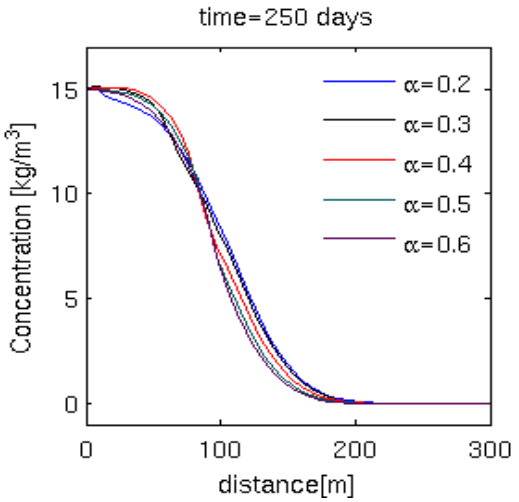

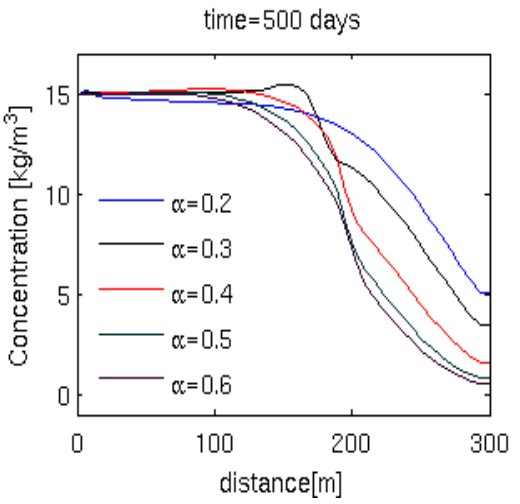

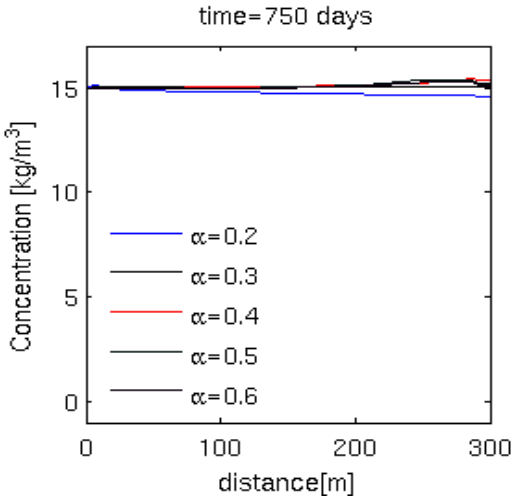

FIGURE 5.39: Concentration profiles at reference reservoir, for different effect coefficients α, $c(0,t) = 15$.

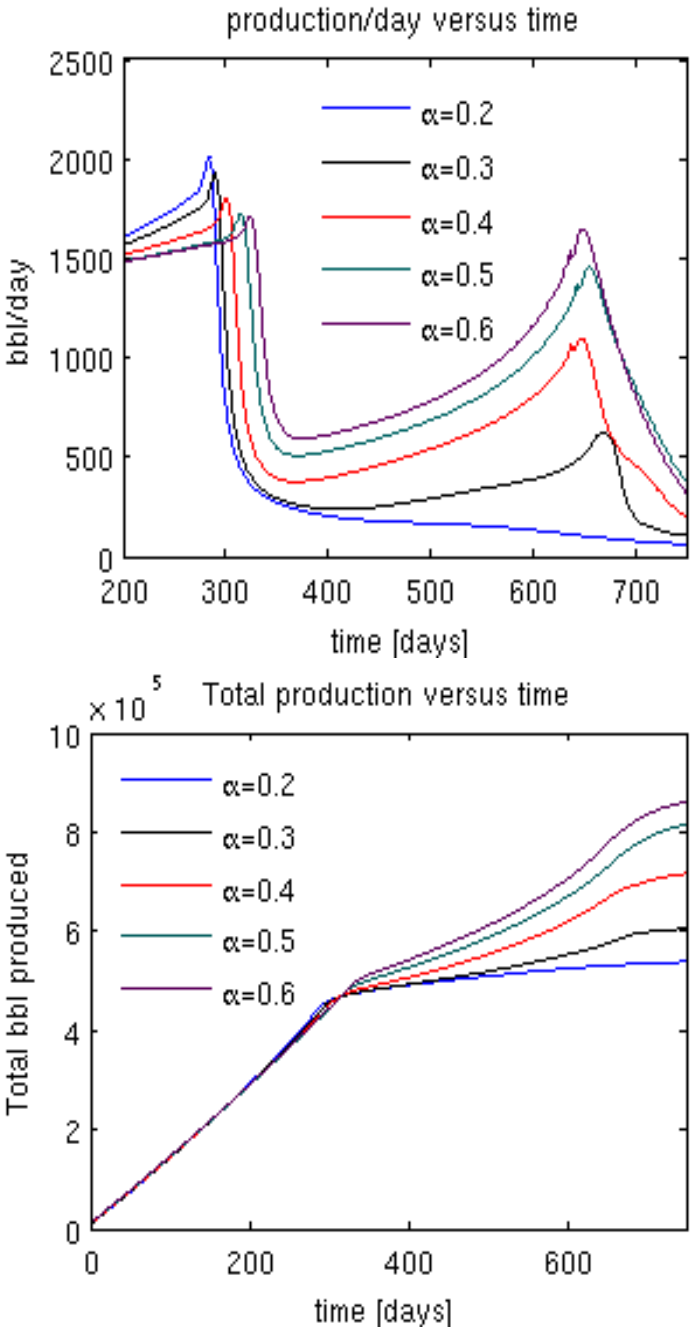

FIGURE 5.40: Production rate and total production at reference reservoir, for different effect coefficients α, $c(0,t) = 15$.

5.5.6 Sensitivity to change in the initial entry pressure, $p_{e,0}$

Determining the pore entry pressure, the minimum capillary pressure required for a pore to be invaded in the reservoir, is crucial and difficult when modelling oil reservoirs. In this section we seek to explore what effect the magnitude of the entry pressure have on reservoir conditions and production. We continue our exploration based on the reference reservoir, Section 5.1 and table 5.1, applying pore entry pressures of $p_{e,0} = \{0.5 \text{ MPa}, 1.5 \text{ MPa}, 2.5 \text{ MPa}, 3.5 \text{ MPa}, 4.5 \text{ MPa}\}$. The comparisons are done based on the same initial- and boundary conditions as in Section 5.5.1, where

$$p(0,t) = 35, \quad s(0,t) = s_{max}, \quad p(L,t) = 5, \quad \frac{\partial s}{\partial x}(L,t) = 0,$$
$$p(x,0) = 5, \quad s(x,0) = 0.3.$$

The injected concentration of microbes is $c(0,t) = 12$, and we do not include dynamic capillary pressure, hence $\tau = 0$.

Figures 5.41 to 5.43 show the plotted results for saturation, concentration and production after 250 days, 500 days and at an end time of 750 days. We discover that the main consequence of higher initial entry pressure is that the water front is moving slightly slower in the case of high entry pressure, compared to the lower entry pressure. This is also visible in the production data, where the production rate is higher earlier in the process in the case of low entry pressure.

At the end time, the system is close to full equilibrium in all three cases, and the total production is equivalent in the end. All together there is small response to significantly higher initial entry pressure, and it does not affect the flow and production remarkably in the performed simulations.

We have also performed simulations with dynamic capillarity, $\tau = 10^7$ Pa $\cdot$ s, but as the results are identical, the plots have been omitted.

The fact that we did not observe much difference with regards to dynamic capillarity, for our reference reservoir, motivated us to perform simulations on the extreme case, Table 5.2 and section 5.5.3. The same procedure was followed, applying initial pore entry pressures of $p_{e,0} = \{0.5 \text{ MPa}, 1.5 \text{ MPa}, 2.5 \text{ MPa}, 3.5 \text{ MPa}, 4.5 \text{ MPa}\}$.

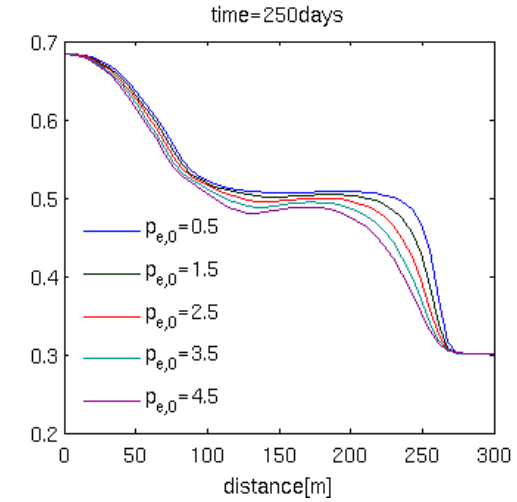

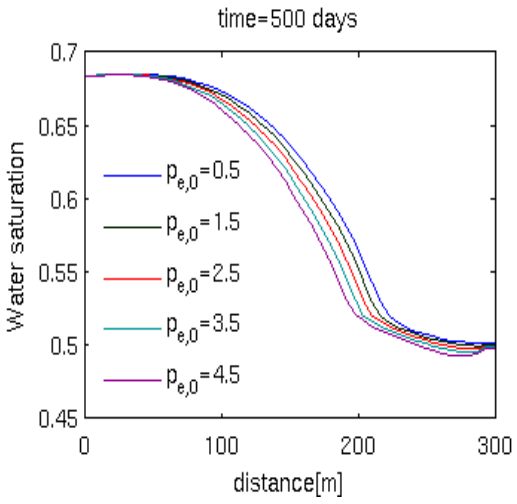

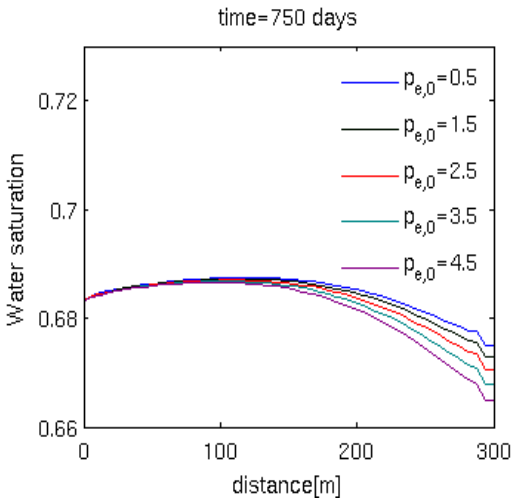

FIGURE 5.41: Saturation profiles at reference reservoir, for different entry pressures $p_{e,0}$, $c(0,t) = 12$.

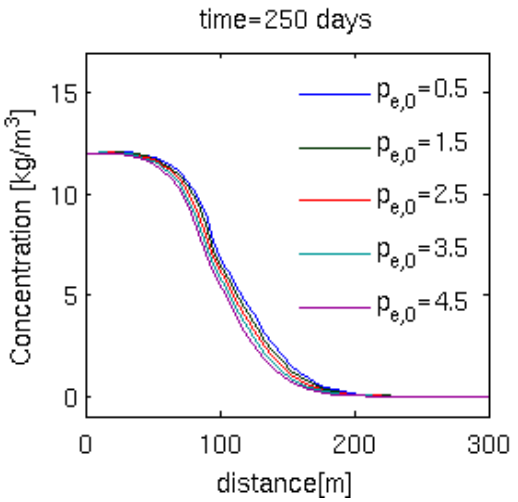

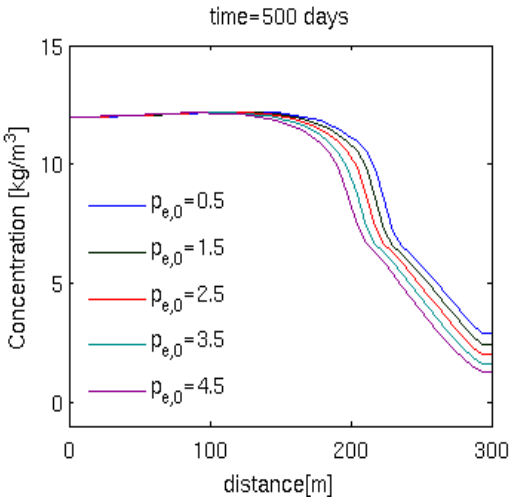

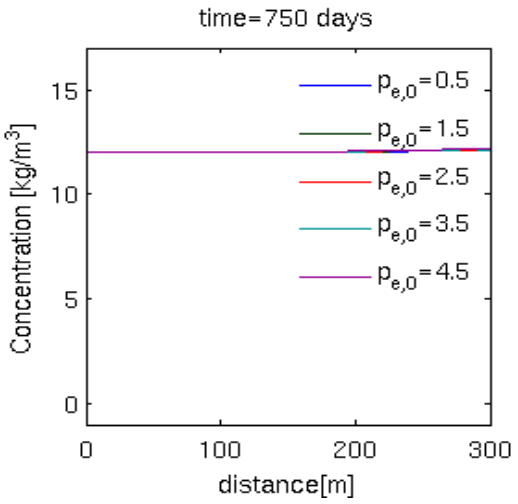

FIGURE 5.42: Concentration profiles at reference reservoir, for different entry pressures $p_{e,0}$, $c(0,t) = 12$.

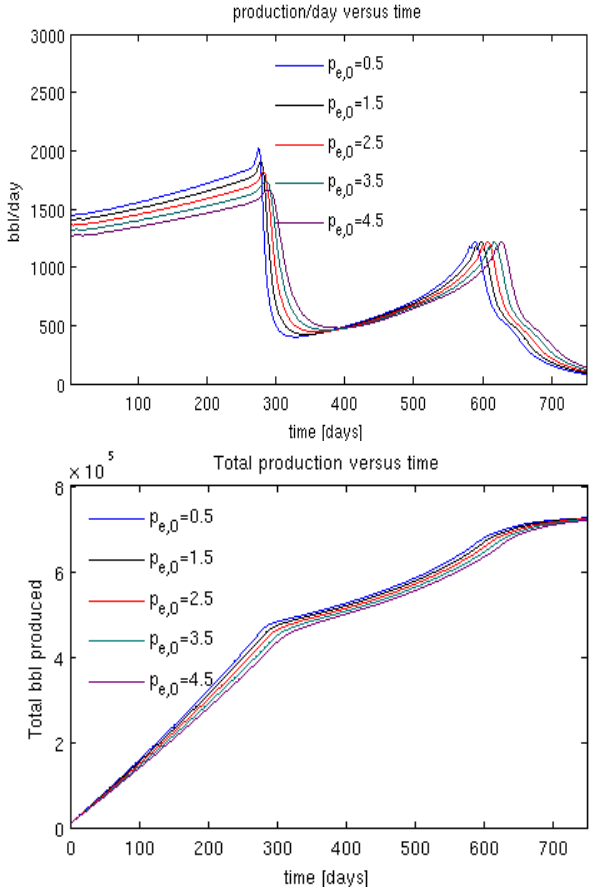

FIGURE 5.43: Production rate and total production at reference reservoir, for different entry pressures $p_{e,0}$, $c(0,t) = 12$.

The BCs and ICs

$$p(0,t) = 35, \quad s(0,t) = s_{max}, \quad p(L,t) = 5, \quad \frac{\partial s}{\partial x}(L,t) = 0,$$
$$p(x,0) = 5, \quad s(x,0) = 0.1,$$

were similar to Section 5.5.3, which reservoir length is $L = 70$ m. Simulations with ($\tau = 10^{10}$ Pa $\cdot$ s), and without, dynamic effects were conducted, and the results are as shown in Figures 5.44 to 5.49. Once again the results including dynamic effects are placed on the right hand side.

As for the results from Section 5.5.3, and contrary to the results for the reference reservoir, the dynamic effects are clearly visible in this case. Two things are worth noticing. Firstly, the dynamic effects are most noteworthy in the case of high initial entry pressure, where the front progresses faster. This may be explained by the fact that the pressure needs to build up before pores can be invaded, see the early peaks in saturation without

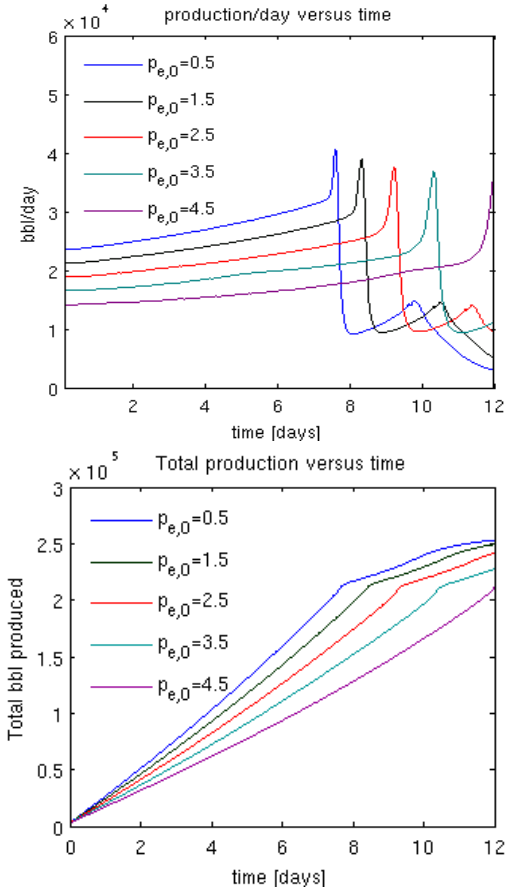

FIGURE 5.44: Production rate and total production for example III, for different entry pressures $p_{e,0}$, $c(0,t) = 12$, without dynamic capillarity.

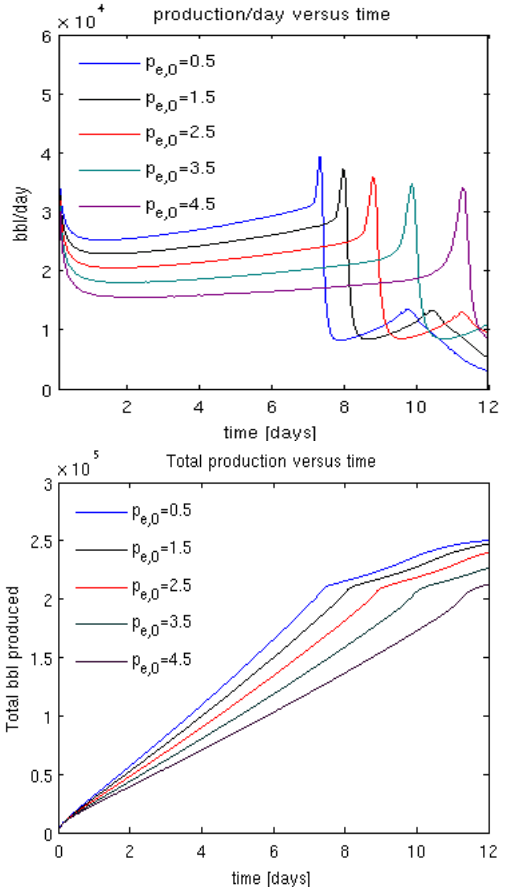

FIGURE 5.45: Production rate and total production for example III, for different entry pressures $p_{e,0}$, $c(0,t) = 12$, with dynamic capillarity.

dynamic capillarity. When dynamic effects are included water can penetrate into the pores even if the pressure is not exceeding the entry pressure. That is, less of the water gets trapped at the pore openings due to dynamic effects. Similar results are shown in [9], see section 6.1, and in our case it leads to considerable differences in the case of high initial entry pressure.

The size of the fronts in the case of no dynamic capillarity, and high initial entry pressure, also explains the distinct peaks in the concentration. As the water flux is higher in these situations, a substantial part of the microbes follows this front, especially visible in the concentration after 4 days.

In terms of ultimate production there is not much difference, but because of what is mentioned above, the production happens earlier when we include dynamic effects.

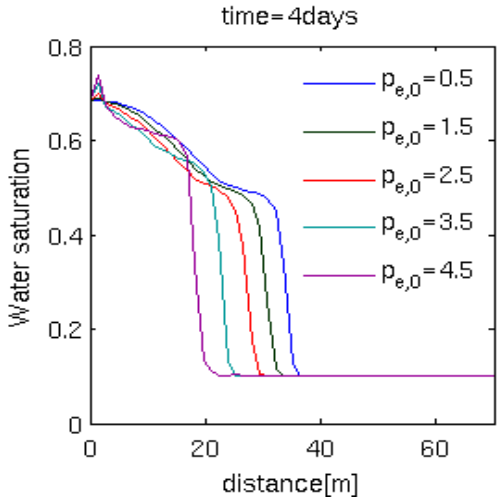

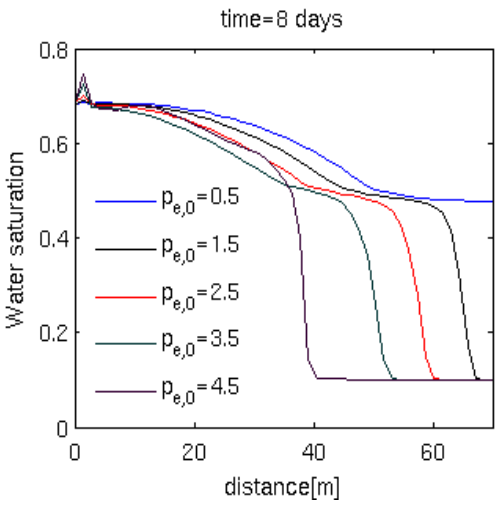

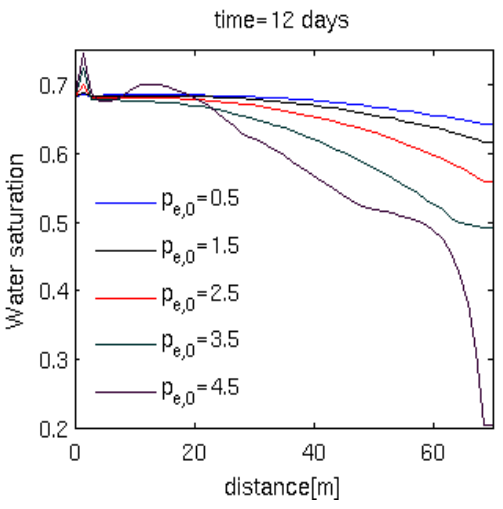

FIGURE 5.46: Saturation profiles for example III, for different entry pressures $p_{e,0}$, $c(0,t) = 12$, without dynamic capillarity

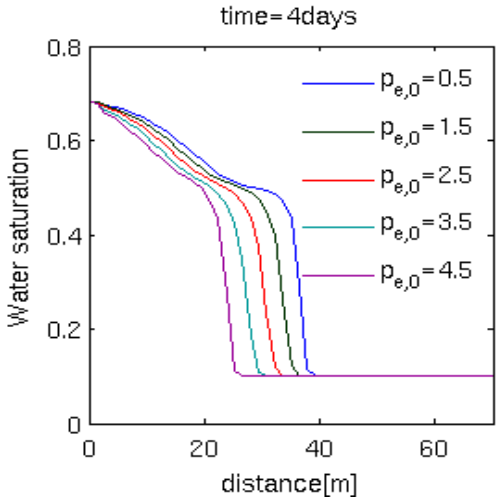

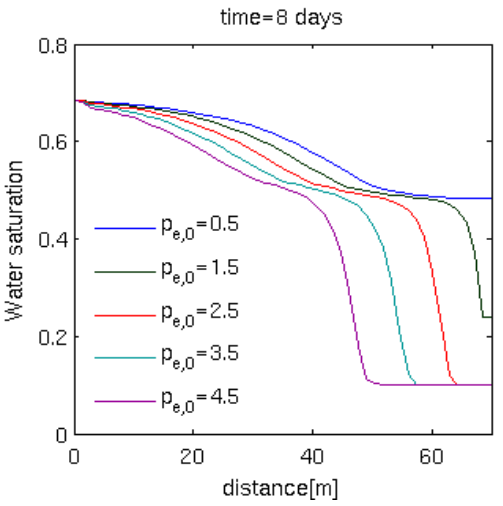

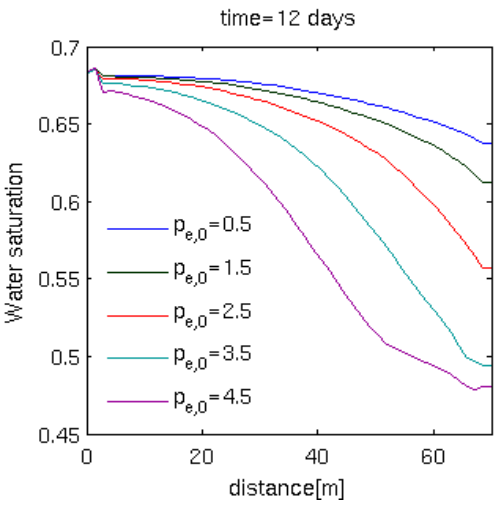

FIGURE 5.47: Saturation profiles for example III, for different entry pressures $p_{e,0}$, $c(0,t) = 12$, with dynamic capillarity.

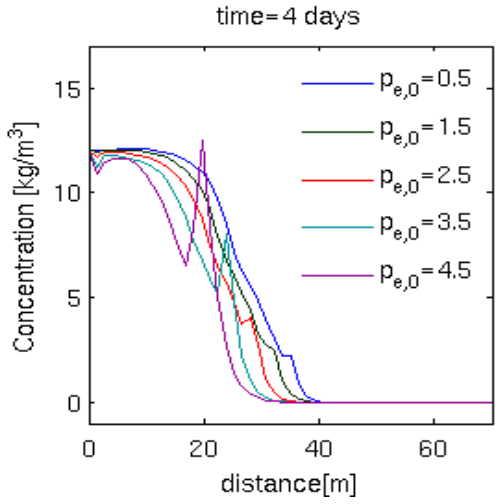

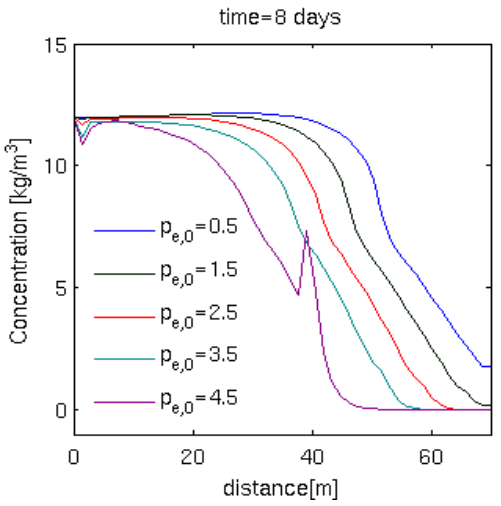

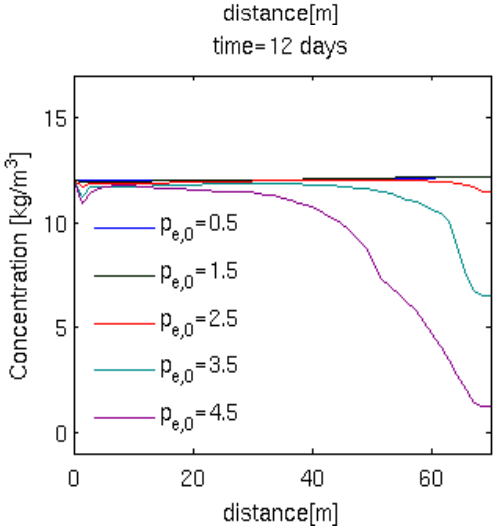

FIGURE 5.48: Concentration profiles for example III, for different entry pressures $p_{e,0}$, $c(0,t) = 12$, without dynamic capillarity.

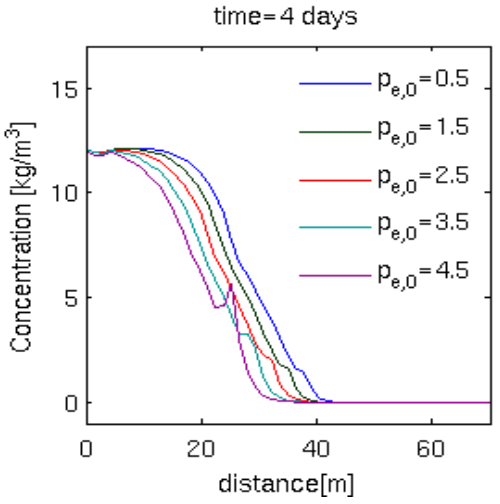

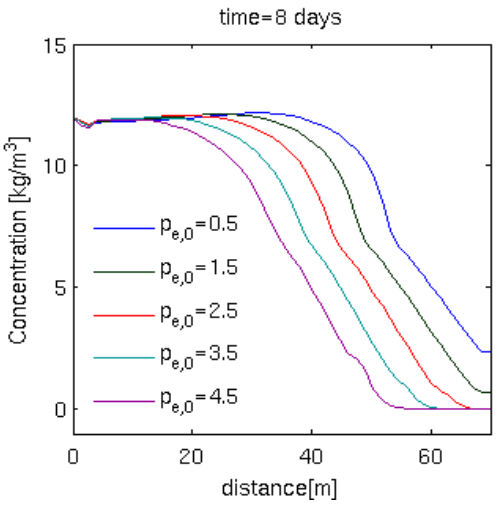

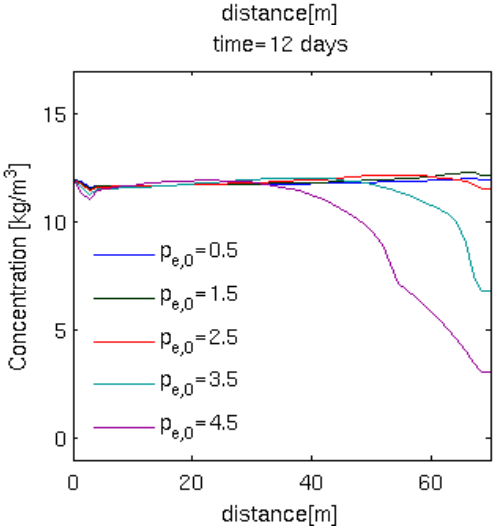

FIGURE 5.49: Concentration profiles for example III, for different entry pressures $p_{e,0}$, $c(0,t) = 12$, with dynamic capillarity.

5.6 Convergence History for the Inner Loop

The numerical discretization in this thesis includes an inner loop to handle the temporal derivative, induced by the dynamic capillary pressure-term. We have not seen this approach been used before, and therefore we include convergence history of the inner loop for the three main examples, Sections 5.5.1 to 5.5.3. The plots show the average error in the solutions for saturation and pressure, versus the number of inner iterations.

The convergence plots have been produced for the most challenging situation, with $c(0,t) = 12$, and included dynamic capillary pressure corresponding to Sections 5.5.1 to 5.5.3 (i.e., $\tau = 10^7$ Pa $\cdot$ s for the first two examples and $\tau = 10^{10}$ Pa $\cdot$ s for the extreme case). In our implementation we have applied a tolerance on the error of $\epsilon = 10^{-10}$, for all simulations. The simulations are first performed with decreasing spatial mesh size, but a constant resolution in time. Results are shown in Figures 5.50 and 5.51.

Observe that the number of iterations needed to forfill the criteria are significantly higher for the reference reservoir, caused by the fact that we are modelling over a long time span of 750 days, as well as a reservoir length of 300 m. Aside from that the convergence of the scheme is clear and unequivocally good in all three cases, where the maximum number of iterations needed are lower for the extreme case, even if the dynamic capillary pressure term has the highest impact in this case. Notice that as the spatial mesh is refined, while maintaining the same temporal gridding, the simulations still converges, but significantly slower. This applies for all three cases.

The same has been performed with decreasing time steps, and fixed spatial resolution, see results in Figures 5.52 and 5.53. Working on coarse temporal resolution, i.e., having longer time steps, comes with the cost of having to iterate the inner loop several times.

Finally, we searched numerically for a refinement-strategy that yielded consistent convergence. Figures 5.54 and 5.55 show consistency in the convergence rate when the spatial resolution is refined with a factor 2, while the temporal mesh is refined by a factor 6. This applies for the first two examples, but only partly for the extreme case, Section 5.5.3, where the convergence rate is reduced for the finest spatial mesh.

Throughout, it is the computation of the pressure which seems to be the most challenging. The convergence rate may be improved through a stabilization technique, as will be described in Section 6.1, but this has not been investigated in this thesis.

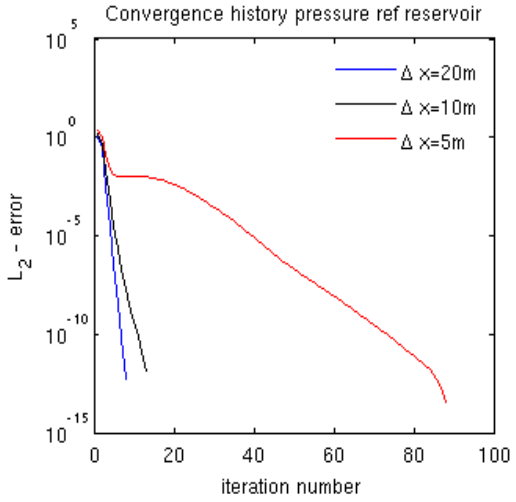

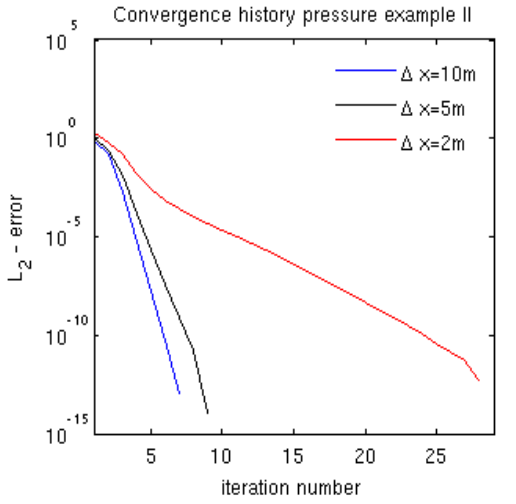

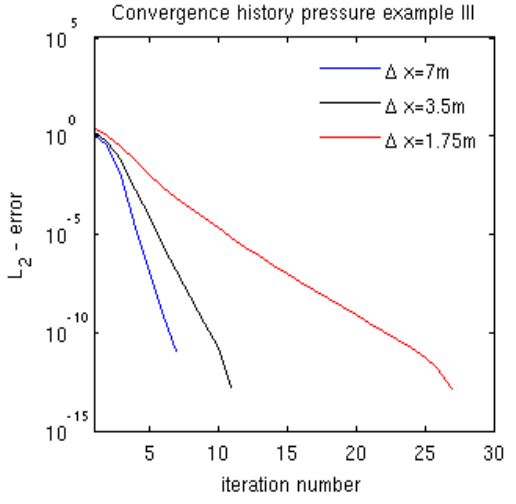

FIGURE 5.50: The average L_2 error versus number of inner iterations for average pressure, for different spatial mesh size.

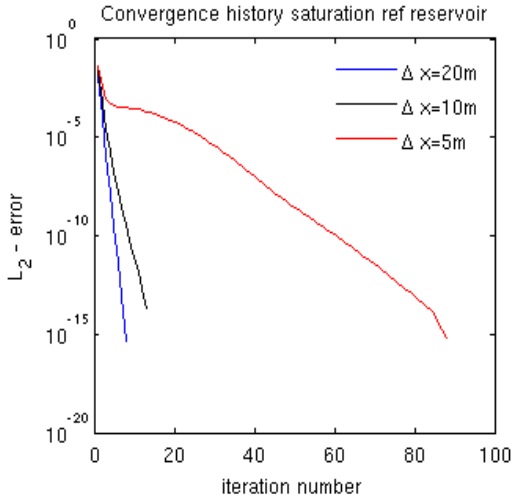

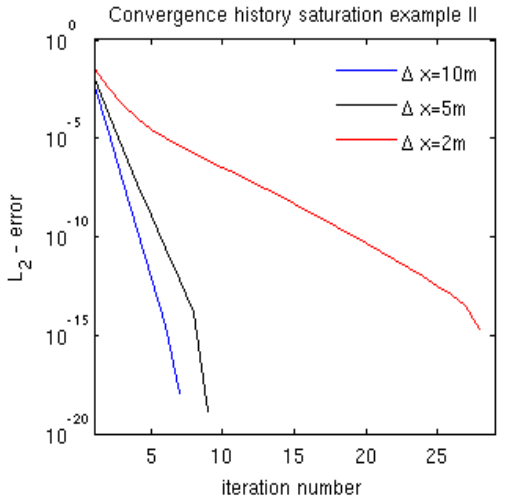

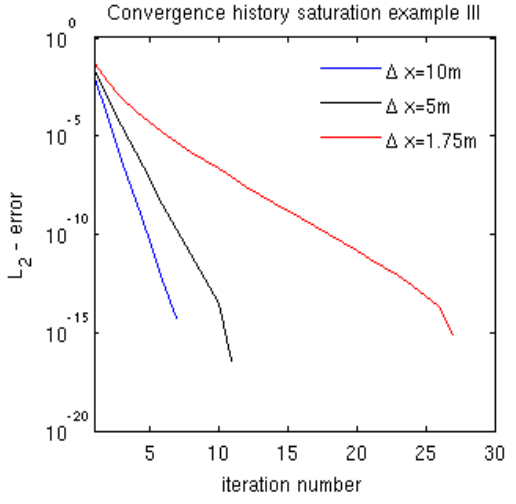

FIGURE 5.51: The average L_2 error versus number of inner iterations for saturation, for different spatial mesh size.

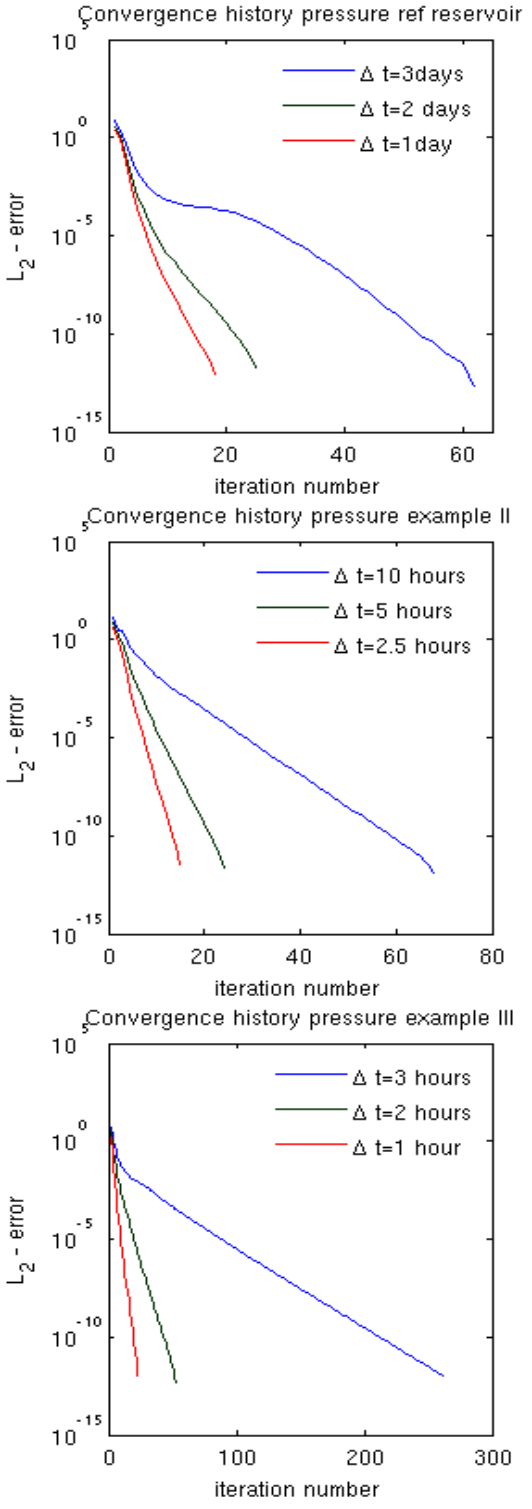

FIGURE 5.52: The average L_2 error versus number of inner iterations for average pressure, for different temporal mesh size.

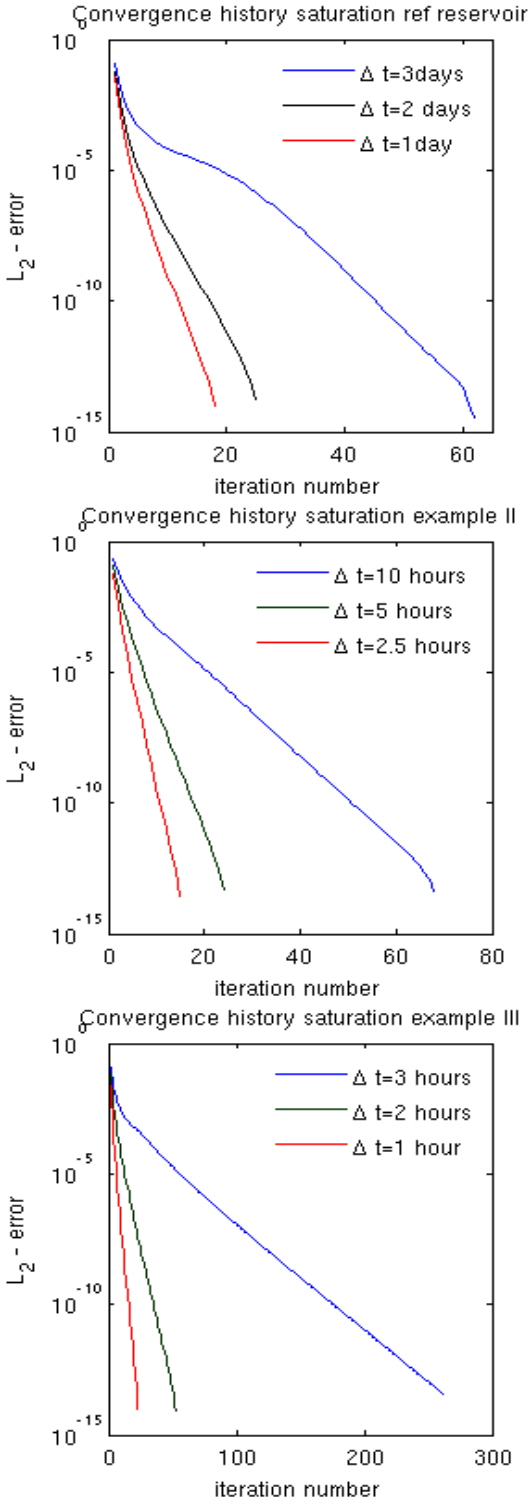

FIGURE 5.53: The average L_2 error versus number of inner iterations for saturation, for different temporal mesh size.

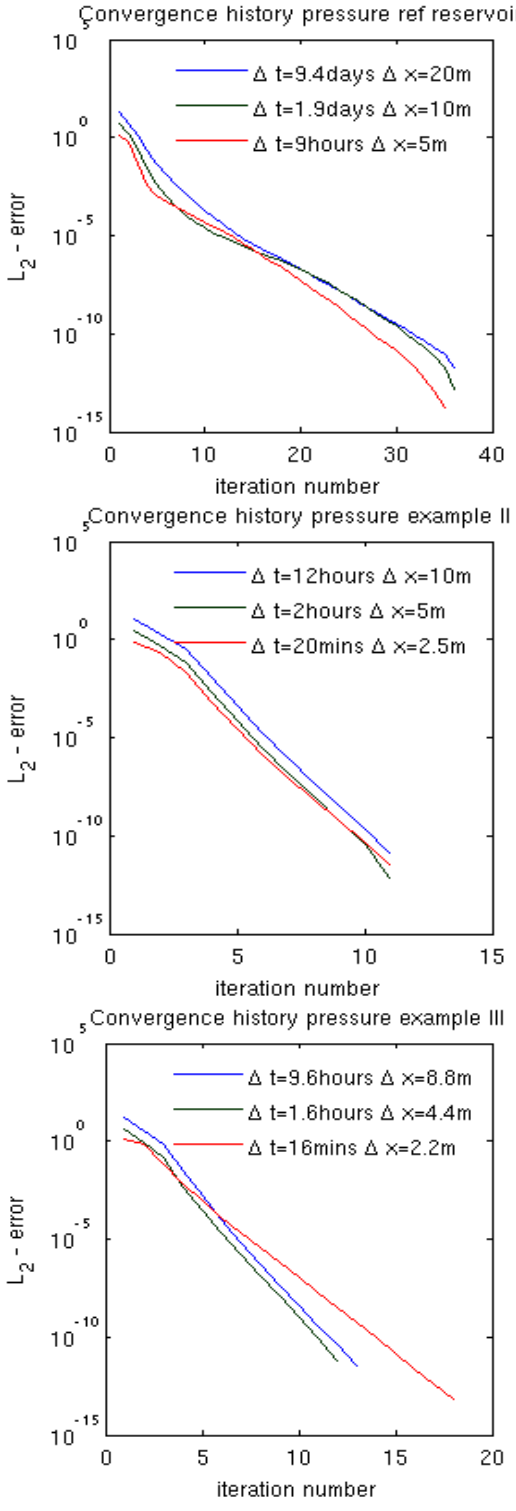

FIGURE 5.54: The average L_2 error versus number of inner iterations for average pressure, for different temporal and spatial mesh size.

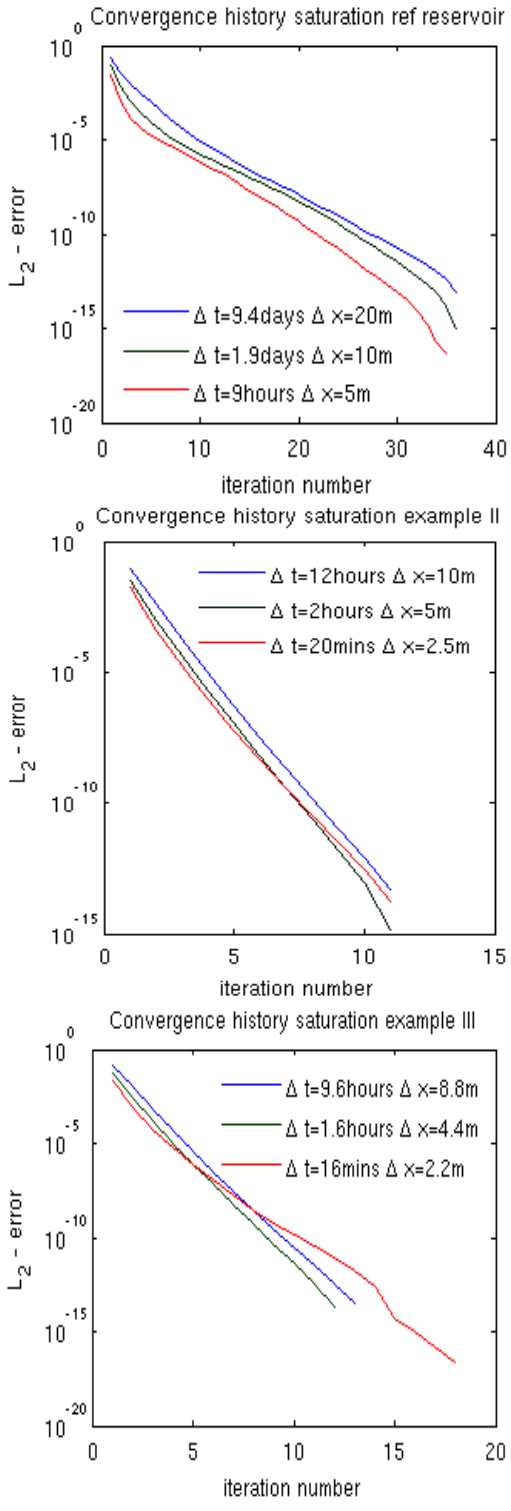

FIGURE 5.55: The average L_2 error versus number of inner iterations for saturation, for different temporal and spatial mesh size.

Chapter 6

Conclusion and Suggestions for Further Work

In this thesis we have modelled a two-phase flow regime in porous media, by designing and implementing a two-phase flow model consisting of oil and water, in addition to a transport equation to describe the motion of microbes in the water phase.

The model is discretized by a new, fully implicit formulation of the flow model, using an additional inner loop to ensure that the dynamic capillary pressure term is handled properly. Spatial discretization has been carried out with the TPFA method, which ensures conservation of the mass. The aim has been to explore the effects dynamic capillarity have on the two-phase flow, as well as the potential effects of MEOR on oil production. We have done so by proposing parameterizations which includes microbial effects, see Section 5.2.1. The parameterizations are inspired by existing theory and experiments conducted by others [4–8], showing that such effects may lead to a reduced interfacial tension. Further, we have performed simulations on three main examples in Section 5.5, where we have compared results with different injected quantity of microbes, and with or without dynamic effects.

Our findings suggest that dynamic capillary pressure plays a minor role in wide-stretched homogeneous porous media, simulated over a long time span, whilst it is shown to play a role in more extreme cases, with rapid changes in the saturation.

We have also performed sensitivity analysis on chosen key parameters, where we have found that the effect coefficient, α, has a huge impact on ultimate oil production. On the other hand, small differences are portrayed for changes in the initial pore entry pressure, $p_{e,0}$, for the reference reservoir. For the extreme case, where dynamic capillarity plays a significant role, the differences are again more apparent.

Further, we have numerically explored the convergence of the new scheme, with regards to the increments, of the updated solutions for saturation and average pressure, satisfying a tolerance limit. It is shown that the scheme converges, but that it is sensitive to the ratio of spatial versus temporal mesh size.

With regards to microbial enhanced oil recovery we have shown that, given our parameterizations, relatively high concentrations of microbes do effect interfacial tension and the pore entry pressure positively, in terms of oil production. Experimentally testing and improving our parameterizations would have been of immense interest, and we hope that they can be an inspiration and idea for others as a starting point. To progress towards more application of MEOR as an enhanced oil recovery technique in the future, interdisciplinary work including microbiologists, biochemists, mathematicians and petroleum engineers must be performed.

6.1 Further Work

It would be a great pleasure if this work, and our scheme, inspires further work. One necessity in the future is to theoretically delve into a convergence analysis of the scheme. Computationally, two other aspects comes to our mind:

Stabilization of the linear scheme

To further enhance the performance of the scheme, and allow for higher spatial resolution, one possibility is to include a stabilization term in the pressure equation. The stabilization term may be on the form

$$L(p^{n+1,i+1} - p^{n+1,i}), \tag{6.1}$$

where L is a real number, playing the role as a stabilization coefficient. In this case, the pressure equation becomes

$$\frac{\partial}{\partial x}(-k(\lambda_\Sigma \frac{\partial p^{n+1,i+1}}{\partial x} + \frac{1}{2}\lambda_\Delta \frac{\partial}{\partial x}(p_c^{n+1,i} - \tau \frac{\mathrm{d}s^{n+1,i}}{\mathrm{d}t}))) + \underline{L(p^{n+1,i+1} - p^{n+1,i})} = \sum_{\alpha=w,n} \frac{F_\alpha}{\rho_\alpha}, \tag{6.2}$$

resulting in an additional term on the diagonal of the system matrix in Equation (4.41). Additionally, $Lp^{n+1,i}$ completes the vector $\mathbf{b}$ in the same system. The pressure- and saturation equation can still be solved sequentially as before.

In our work we have not had time enough to do full simulations with this includement, neither have we done a theoretical analysis on the performance of a stabilization of this type. However, preliminary simulations on our code indicate that a stabilization coefficient $L < 0.1$ allows for higher spatial resolution, compared with the same resolution in time. Theoretical background for such an approach can be found in [1–3].

Application on heterogeneous media

In the future it will also be of interest to apply the model to situations similar to the approach in [9], where van Duijn, Cao and Pop have set up a one dimensional domain consisting of two adjacent homogeneous blocks separated by an interface. The blocks have constant, but unequal, absolute permeability, which may lead to entrapment of the non-wetting phase, when flowing from the coarse block towards the fine material. The interface is introduced as a thin porous layer, which length is passed to zero. The interesting thing to explore is the effect of dynamic capillarity, and if such non-equilibrium effects may lead to less of the non-wetting fluid being trapped at the interface. In [9] simulations mimicking an oil blob displaced by water suggest that dynamic effects allow for oil to penetrate the interface, thus occupying porespace in the fine grained block.

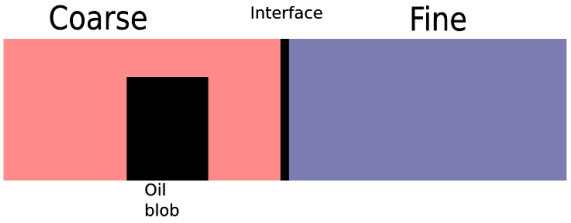

FIGURE 6.1: A heterogeneous case: two homogeneous blocks separated by an interface, with an initial oil blob in the coarse block at time t=0 [9].

Bibliography

[1] F.A.Radu, J.M.Nordbotten, I.S.Pop, and K.Kumar. A robust linearization scheme for finite volume based discretizations for simulation of two-phase flow in porous media. *J. of Com. and App. Math.*, 289:134–141, 2015. URL http://dx.doi.org/10.1016/j.cam.2015.02.051.

[2] I.S.Pop, F.A.Radu, and P.Knabner. Mixed finite elements for the richards' equation: linearization procedure. *J. of Com. and App. Math.*, 168:365–373, 2004. URL http://dx.doi.org/10.1016/j.cam.2003.04.008.

[3] M.Slodička. A robust and efficient linearization scheme for doubly nonlinear and degenerate parabolic problems arising in flow in porous media. *SIAM J. on Sci. Comp.*, 23:5:1593–1614, 2002. URL http:/dx.doi.org/10.1137/S1064827500381860.

[4] E.Kowalewski, I.Rueslåtten, T.Boassen, E.Sunde, J.Å.Stensen, B.L.P.Lillebø, G.Bødtker, and T.Torsvik. Analyzing microbial improved oil recovery processes from core floods. IPTC, 2005. URL http://dx.doi.org/10.2523/10924-MS.

[5] T.M.Al-Bazali, J.Zhang, M.E.Chenevert, and M.M.Sharma. Capillary entry pressure of oil-based muds in shales: The key to the success of oil-based muds. *Energy Sources, Part A: Recovery, Utilization, and Environmental Effects*, 30:4:297–308, 2007. URL http://dx.doi.org/10.1080/15567030600820609.

[6] P.Shen, B.Zhu, X.B.Li, and Y.S.Wu. The influence of interfacial tension on water/oil two-phase relative permeability. 95405, 2006. URL http://petroleum.mines.edu/research/emg/SPE_papers/2006,%20SPE-95405-MS-P.pdf.

[7] M.F.Destefanis and G.B.Savioli. Influence of relative permeabilities on chemical enhanced oil recovery. *J. of Physics*, 296, 2011. URL http://stacks.iop.org/1742-6596/296/i=1/a=012014.

[8] E.Ghoodjani and S.H.Bolouri. Experimental study and calculation of CO_2-oil relative permeability. *Petroleum & Coal*, 53:123–131, 2011. URL http://www.vurup.sk/sites/default/files/downloads/pc_2_2011_ghoodjani_105.pdf.

[9] C.J.van Duijn, X.Cao, and I.S.Pop. Two-phase flow in porous media: dynamic capillarity and heterogeneous media. *Casa report*, 2015. URL http://www.win.tue.nl/analysis/reports/rana15-17.pdf.

[10] J.Bear. *Dynamics of Fluids in Porous Media*. Dover, City of New York, State of New York, 1988.

[11] D.Zhang, R.Zhang, S.Chen, and W.E.Soll. Pore scale study of flow in porous media: Scale dependency, rev, and statistical rev. *Geophysical Research Letters*, 27(8): 1195–1198, April 2000. URL http://dx.doi.org/10.1029/1999GL011101.

[12] S.N.Ehrenberg and P.H.Nadeau. Sandstone vs. carbonate petroleum reservoirs: A global perspective on porosity-depth and porosity-permeability relationships. *The Amer. Ass. of Pet. Geo.*, 89(4):435–445, April 2005.

[13] K. Aziz and A. Settari. *Petroleum Reservoir Simulation*. Elsevier, London, Great Britain, 1979.

[14] J.M.Nordbotten and M.A.Celia. *Geological storage of CO_2: Modeling Approaches for Large-Scale Simulations*. Wiley, Hoboken, New Jersey, 2012.

[15] A.Muggeridge, A.Cockin, K.Webb, H.Frampton, I.Collins, T.Moulds, and P.Salino. Recovery rates, enhanced oil recovery and technological limits. *Phil.Trans.R.Soc.A*, 372(10):100–124, December 2013. URL http://dx.doi.org/10.1098/rsta.2012.0320.

[16] B.B.Sandiford. Laboratory and field studies of water floods using polymer solutions to increase oil recoveries. *J. of Pet. Tech.*, 16(1):917–922, January 1964. URL http://dx.doi.org/10.2118/844-PA.

[17] S.Kokal and A.Al-Kaabi. Enhanced oil recovery: challenges & opportunities. *World Petroleum Council: Official Publication*, (yearbook):64–69, 2010. URL http://www.world-petroleum.org/docs/docs/publications/2010yearbook/P64-69_Kokal-Al_Kaabi.pdf.

[18] N.Youssef, M.S.Elshahed, and M.J.McInerney. Microbial processes in oil fields: Culprits, problems, and opportunities. In A.I.Laskin, S.Sariaslani, and G.M.Gadd, editors, *Advances in applied microbiology, Vol. 66*, pages 141–251. Academic, London, 2009.

[19] I.M.Banat. Biosurfactants production and possible uses in microbial enhanced oil recovery and oil pollution remediation: A review. *Biore. Tech.*, 51:1–12, 1995. URL http://dx.doi.org/10.1016/0960-8524(94)00101-6.

[20] I.M.Banat, R.S.Makkar, and S.S.Cameotra. Potential commercial applications of microbial surfactants. *App. Microbial Biotech.*, 53:493–508, 2000. URL http://pmid.us/10855707.

[21] M.R.Gray, A.Yeung, J.M. Foght, and H.W.Yarranton. Potential microbial enhanced oil recovery processes: A critical analysis. 114676, 2008. URL https://www.onepetro.org/download/conference-paper/SPE-114676-MS?id=conference-paper%2FSPE-114676-MS.

[22] R.T.Armstrong and D.Wildenschild. Microbial enhanced oil recovery in fractional-wet systems: A pore-scale investigation. *Transport in Porous Media*, 92:819–835, 2012. URL http://dx.doi.org/10.1007/s11242-011-9934-3.

[23] D.Momeni and T.F.Yen. Microbial processes in oil fields: Culprits, problems, and opportunities. In T.F.Yen, editor, *MICROBIAL ENHANCED OIL RECOVERY:Principle and Practice*, pages 1–13. CRC press, Boca Raton, FL, US, 1990.

[24] H.Rashedi, F.Yazdian, and S.Naghizadeh. Microbial enhanced oil recovery. In L.Romero-Zerón, editor, *Introduction to Enhanced Oil Recovery (EOR) Processes and Bioremediation of Oil-Contaminated Sites*, pages 71–88. InTech, 2012.

[25] J.Adetunji. *MICROBIAL ENHANCED OIL RECOVERY*. PhD thesis, University of Aalborg, Denmark, august 2012.

[26] I.Lazar, I.G.Petrisor, and T.F.Yen. Microbial enhanced oil recovery. *Pet. Sci. and Tech.*, 25:1353–1366, 2007. URL http://dx.doi.org/10.1080/10916460701287714.

[27] Petro wiki - capillary pressure. http://petrowiki.org/Capillary_pressure. Accessed: 2015-05-20.

[28] Y. Mualem. A new model for predicting the hydraulic conductivity of unsaturated porous media. *Water Resources Research*, 12(3):513–522, 1976. URL http://dx.doi.org/10.1029/WR012i003p00513.

[29] M.Th.van Genuchten. A closed-form equation for predicting the hydraulic conductivity of unsaturated soils. *Soil Sc. Soc. of America*, 44(5):892–898, 1980. URL http://dx.doi.org/10.2136/sssaj1980.03615995004400050002x.

[30] P.Bastian. *Numerical Computation of Multiphase Flows in Porous Media*. PhD thesis, Christian Albrecht universitet Germany, june 1999.

[31] S.M.Hassanizadeh, M.A.Celia, and H.K.Dahle. Dynamic effect in the capillary pressure–saturation relationship and its impacts on unsaturated flow. *Vadose zone j.*, 1:38–59, 2002. URL http://dx.doi.org/10.2136/vzj2002.3800.

[32] R.Holm, M.I.J.van Dijke, S.Geiger, and M.Espedal. Consistent capillary pressure and relative permeability for mixed-wet systems in macroscopic three-phase flow simulation. EAGE, 2008. URL http://dx.doi.org/10.3997/2214-4609.20146419.

[33] D.B.Das, R.Gauldie, and M.Mirzaei. Dynamic effects for two-phase flow in porous media: Fluid property effects. *AIChE J.*, 53:2505–2520, 2007. URL http://dx.doi.org/10.1002/aic.11292.

[34] Y.Fan and I.S.Pop. A class of pseudo-parabolic equations: existence, uniqueness of weak solutions, and error estimates for the euler-implicit discretization. *Math. methods in the app. sci.*, 34:2329–2339, 2011. URL http://dx.doi.org/10.1002/mma.1537.

[35] I.Skjælaaen. *Mathematical Modeling of Microbial Induced Processes in Oil Reservoirs*. PhD thesis, University of Bergen, february 2010.

[36] M.Peleg. A model of microbial growth and decay in a closed habitat based on combined fermi's and the logistic equations. *J. of the Sc. of Food and Agric.*, 71: 225–230, 1996. URL http://onlinelibrary.wiley.com/doi/10.1002/%28SICI%291097-0010%28199606%2971:2%3C225::AID-JSFA572%3E3.0.CO;2-%23/epdf.

[37] F.A.Radu. *Mixed finite element discretization of Richards' equation: error analysis and application to realistic infiltration problems*. PhD thesis, University of Erlangen-Nuremberg, 2004.

[38] Z.Chen, G.Huan, and Y.Ma. *Computational Methods for Multiphase Flow in Porous Media*. Society for Industrial and Applied Mathematics, Philadelphia,USA, 2006.

[39] J.W.Thomas. *Numerical Partial Differential Equations: Finite Difference Methods*. Springer-Verlag, City of New York, State of New York, 1995.

[40] R.A.Adams and C.Essex. *Calculus: a Complete Course*. Pearson, Toronto,Canada, 2010.

[41] Ø.Pettersen. Lecture notes. *Basics of Reservoir Simulation With the Eclipse Reservoir Simulator*, 2006. URL http://folk.uib.no/fciop/index_htm_files/ResSimNotes.pdf.

[42] M.P.Anderson and W.W.Woessner. *Applied groundwater modeling: simulation of flow and advective transport*. Academic Press, San Diego, California, USA, 1992.

[43] F.A.Radu, I.S.Pop, and P.Knabner. On the convergence of the newton method for the mixed finite element discretization of a class of degenerate parabolic equation. In A.Bermudez de Castro, D.Gómez, P.Quintela, and P.Salgado, editors, *Numerical Mathematics and Advanced Applications*, pages 1194–1200. Springer Verlag, 2006.

[44] F.A.Radu and I.S.Pop. Newton method for reactive solute transport with equilibrium sorption in porous media. *J. of Com. and App. Math.*, 234:2118–2127, 2010. URL http://dx.doi.org/10.1016/j.cam.2009.08.070.

[45] F.A.Radu and I.S.Pop. Mixed finite element discretization and newton iteration for a reactive contaminant transport model with nonequilibrium sorption. *Com. Geosc.*, 15:431–450, 2011. URL http://dx.doi.org/10.1007/s10596-010-9213-3.

[46] F.A.Radu, I.S.Pop, and P.Knabner. Order of convergence estimates for an euler implicit, mixed finite element discretization of richards' equation. *SIAM*

J. on Num. Anal., 42:1452–1478, 2004. URL http://dx.doi.org/10.1137/S0036142902405229.

[47] F.A.Radu, I.S.Pop, and P.Knabner. Error estimates for a mixed finite element discretization of some degenerate parabolic equations. *Numerische Mathematik*, 109:285–311, 2008. URL http://dx.doi.org/10.1007/s00211-008-0139-9.

[48] F.A.Radu, I.S.Pop, and S.Attinger. Analysis of an euler implicit - mixed finite element scheme for reactive solute transport in porous media. *Num. Methods for Partial Diff. Eq.*, 26:320–344, 2010. URL http://dx.doi.org/10.1002/num.20436.

[49] F.A.Radu, A.Muntean, I.S.Pop, N.Suciu, and O.Kolditz. A mixed finite element discretization scheme for a concrete carbonation model with concentration-dependent porosity. *J. of Com. and App. Math.*, 246:74–85, 2013. URL http://dx.doi.org/10.1016/j.cam.2012.10.017.

[50] K.Kumar, I.S.Pop, and F.A.Radu. Convergence analysis of mixed numerical schemes for reactive flow in a porous medium. *SIAM J. on Num. Anal.*, 51:2283–2308, 2013. URL http://dx.doi.org/10.1137/120880938.

[51] K.Kumar, I.S.Pop, and F.A.Radu. Convergence analysis for a conformal discretization of a model for precipitation and dissolution in porous media. *Numerische Mathematik*, 127:715–749, 2014. URL http://dx.doi.org/10.1007/s00211-013-0601-1.

[52] B.Amaziane, M.Jurak, and A.Z.Keko. Modeling and numerical simulations of immiscible compressible two-phase flow in porous media by the concept of global pressure. *Transport in Porous Media*, 84:133–152, 2010. URL http://dx.doi.org/10.1007/s11242-009-9489-8.

[53] R.Helmig. *Multiphase Flow and Transport Processes in the Subsurface*. Springer-Verlag, Heidelberg, Berlin, 1997.

[54] R.Hilfer and H.Besserer. Macroscopic two-phase flow in porous media. *Physica B*, 279:125–129, 2000. URL http://dx.doi.org/10.1016/S0921-4526(99)00694-8.

[55] X.Cao and I.S.Pop. Two-phase porous media flows with dynamic capillary effects and hysteresis: Uniqueness of weak solutions. *Com. and Math. with App.*, 69: 688–695, 2015. URL http://dx.doi.org/10.1016/j.camwa.2015.02.009.

[56] B.Amaziane, M.Jurak, and A.Z.Keko. Modeling and numerical simulations of water-gas flow in porous media using the concept of global pressure. 2009. URL http://web.math.pmf.unizg.hr/~jurak/amaziane0.pdf.

[57] S.G.Ahmed. A numerical algorithm for solving advection-diffusion equation with constant and variable coefficients. *The Open Num. Methods J.*, 4:1–7, 2012. URL http://benthamopen.com/contents/pdf/TONUMJ/TONUMJ-4-1.pdf.

[58] R.Fučík and J.Mikyška. Numerical investigation of dynamic capillary pressure in two-phase flow in porous medium. *Mathematica Bohemica*, 136:395–403, 2011. URL http://geraldine.fjfi.cvut.cz/~benes/Dwnld/mb136_4_6_fucik.pdf.

[59] T.Shubao, L.Gang, H.Shunli, and Y.Lamin. Dynamic effect of capillary pressure in low permeability reservoirs. *PETROL. EXPLOR. DEVELOP.*, 39:405–411, 2012. URL http://dx.doi.org/10.1016/S1876-3804(12)60057-3.

[60] H.Zhang, S.He, C.Jiao, G.Luan, S.Mo, and X.Guo. Determination of dynamic relative permeability in ultra-low permeability sandstones via x-ray ct technique. *J. of Pet. Expl. and Prod. Tech.*, 4:443–455, 2014. URL http://dx.doi.org/10.1007/s13202-014-0101-6.